Numerical Simulation of Hydrodynamic Forces on Bridge Decks

Nader Naderi

TU Delft
Delft University of Technology

CoMEM

Challenge the future

ERASMUS +: ERASMUS MUNDUS MOBILITY PROGRAMME

Master of Science in

COASTAL AND MARINE ENGINEERING AND MANAGEMENT

CoMEM

NUMERICAL SIMULATION OF HYDRODYNAMIC FORCES ON BRIDGE DECKS

Technische Universiteit Delft (TU Delft)
16th July 2018

Nader Naderi

NTNU
Norwegian University of
Science and Technology

TUDelft
Delft
University of
Technology

UNIVERSITAT POLITÈCNICA
DE CATALUNYA
BARCELONATECH

UNIVERSITY OF
Southampton

CITY UNIVERSITY
LONDON

The Erasmus+: Erasmus Mundus MSc in Coastal and Marine Engineering and Management is an integrated programme including mobility organized by five European partner institutions, coordinated by Norwegian University of Science and Technology (NTNU).

The joint study programme of 120 ECTS credits (two years full-time) has been obtained at two or three of the five CoMEM partner institutions:

- Norges Teknisk- Naturvitenskapelige Universitet (NTNU) Trondheim, Norway
- Technische Universiteit (TU) Delft, The Netherlands
- Universitat Politècnica de Catalunya (UPC). BarcelonaTech. Barcelona, Spain
- University of Southampton, Southampton, Great Britain
- City University London, London, Great Britain

During the first three semesters of the programme, students study at two or three different universities depending on their track of study. In the fourth and final semester, an MSc project and thesis has to be completed. The two-year CoMEM programme leads to multiple officially recognized MSc degree certificates. These will be issued by the universities that have been attended by the student. The transcripts issued with the MSc Degree Certificate of each university include grades/marks and credits for each subject.

Information regarding the CoMEM programme can be obtained from the programme coordinator:

Øivind A. Arntsen, Dr.ing.
Associate Professor of Marine Civil Engineering
Department of Civil and Environmental Engineering
NTNU Norway
Mob: +47-92650455 Fax: + 47-73597021
Email: oivind.arntsen@ntnu.no

CoMEM URL: https://www.ntnu.edu/studies/mscomem

CoMEM Thesis

This thesis was completed by:
Nader Naderi

Under the supervision of:
Prof.dr.ir. W.S.J. Uijttewaal
Associate Prof.dr.ir. J.D. Bricker
Assistant Prof.dr.ir. Y. Yang

As a requirement to attend the degree of
Erasmus+: Erasmus Mundus Master in Coastal and Marine Engineering and Management (CoMEM)

Taught at the following educational institutions:

Norges Teknisk- Naturvitenskapelige Universitet (NTNU)
Trondheim, Norway

Technische Universiteit (TU) Delft
Delft, The Netherlands

University of Southampton,
Southampton, Great Britain

At which the student has studied from August 2016 to July 2018.

Numerical Simulation of Hydrodynamic Forces on Bridge Decks

By

Nader Naderi

An electronic version of this thesis is available at
http://repository.tudelft.nl/

Correspondence with the author may be directed to:
n.naderi@live.com

Summary

Highway bridges along the coast and small river bridges in mountainous regions can be submerged during storm surges or strong rainfall events, respectively. Loss of serviceability during these conditions can dramatically hamper the evacuation plan and the capacity for emergency transportation, thus it is essential to ensure the stability of bridges in extreme hydrological events. Correct estimates of the hydrodynamic forces on a bridge allows bridge designers to evaluate the robustness of the bridge in a more sophisticated approach rather than relying on a constant force magnitude obtained from a small range of physical tests.

This study presents numerical simulations performed to quantify the hydrodynamic forces on a bridge deck with a rectangular cross section. The results of the numerical model are validated against the results of physical experiments. More than 700 simulations were performed to thoroughly investigate the effect of certain parameters on the flow field and forces on the deck. The parameters considered include: the water level, the Froude number, the blockage ratio, the proximity of the deck to the channel floor, the inclination of the deck, and the aspect ratio of the deck.

The lift force is found to be downward unless the deck is significantly submerged i.e., inundation ratio (h^*) is greater than 3.5, and the upstream velocity is relatively small, $F_{rd}<0.6$. For $h^*<3.5$ the development of flow patterns on the upper side of the deck is constrained by the presence of the free surface which causes an asymmetric pressure distribution in the vertical direction and ultimately results in a downward force. Increase in flow velocity results in a higher downward force and hence increase the bridge stability (provided that the submergence of the bridge is not too high, $h^*<4$). When considering the trend of changes in lift and drag forces simultaneously, it can be said that the combination of small velocities and inundation ratios higher than 2 results in the most critical situation for the vertical stability of the bridge deck.

An increase in the blockage ratio results in an increase in the drag coefficient. On the other hand, a decrease in the blockage ratio shifts the drag coefficient towards the value of 1.56, which corresponds to the drag coefficient of a rectangular cylinder in an unbounded flow. Considering the common flow conditions of practical interest for bridge designers, the upper boundary of the drag coefficient for the box deck was found to be 2.8.

Incipient failure analysis is performed to establish a hydrodynamic situation that can cause the failure of the deck. Regardless of the proximity ratio and the Froude number, the bridge deck collapsed when the inundation ratio was higher than 1.3. This indicates that the deck is more susceptible to high water levels than to flood velocity or to the distance to the channel floor. Moreover, no bridge failure occurred for inundation ratios lower than 1.3, indicating that the deck must be deeply submerged to fail.

By extracting the starting point of failure for a wide range of inundation ratios, proximity ratios, and Froude numbers, contour lines of the threshold of failure are drawn. These contour lines representing the starting point of failure provide the basis for more accurate estimates of the failure of the bridge due to flood loadings and can be considered to be included in the bridge design codes and guidelines. In fact, this

proposed method is more reliable than the traditional method which assumes a constant value for drag and lift. The traditional methods are still present in some guidelines such as the AASHTO Load and Resistance Factor Design (LRFD) Bridge Design Specifications.

Attaching wing-shaped structures on the sides of the deck was proposed as a countermeasure to avoid failure of the bridge decks. Although the projected area of the deck perpendicular to the direction of flow was kept constant, it was expected that CD, CL, and CM would change; since they are dependent on the geometry of the deck, and the flow pattern is altered significantly due to the presence of wings.

Results of several simulations for six different shape of wings under different inundation ratio and Froude number indicated that a rational shape of the wings can significantly alter the flow pattern around the deck and postpone occurrence of failure during conditions of really high water levels (h*>2.5) and high flood velocity (Fr>0.65). The proposed countermeasure can be considered as a robust solution for the wide range of probable floods, because of the fact that firstly, occurrence of this extreme hydrological situation is rare, and secondly, the stability of the deck in that situation might not be the first priority, especially compared with the risk of flooding a large part of the upstream land.

Keywords: CoMEM, Fluent, hydrodynamic forces, bridge deck, drag, lift, moment, numerical simulation

Acknowledgement

Table of Contents

List of Figures

List of Tables

Symbol	Units	Description
A	m^2	Reference area
C_D	-	Drag coefficient
CF	-	Correction factor for debris
C_L	-	Lift coefficient
C_M	-	Moment coefficient
F_D	N	Drag force
F_L	N	Lift force
F_B	N	Buoyancy force
F_W	N	gravitational force
h_b	m	Distance from ground to the bottom of the bridge
h_u	m	Height of water from the ground
h_*	-	Inundation ratio
L	m	Bridge length
L_{cg}	m	Horizontal distance from the centre of gravity to the lower downstream heel of the deck
M_{cg}	N.m	Moment about the centre of gravity
M_h	N.m	Moment about the heel of the deck
μ	-	Friction factor
S	m	Deck thickness
UC_h	-	Horizontal stability ratio
UC_V	-	Vertical stability ratio
UC_M	-	Overturning stability ratio
V	m/s	Free stream velocity
V_i	m/s	Incident velocity
V_l	m/s	Local velocity
V_u	m/s	Upstream undisturbed velocity
V'	m^3	Volume of liquid displaced
V''	m/s	Debris velocity
W	m	Bridge width
ρ	kg/m3	Density of water

1 Introduction

This chapter provides the reader with the research motivation and questions. Research significance is highlighted in detail. Thesis structure and research approach are explained in the last part of this chapter.

1.1 Background

The U.S. Department of Transportation Climate Change Center has indicated that with a continuous increase in global temperature, changes in weather conditions are unavoidable [1]. Changes in precipitation and storm patterns combined with changes in land-use have resulted in more frequent and severe storms and floods [2]. Bridges, even those which are designed to withstand a 100-year return period flood, are experiencing extreme hydrological events more frequently. The occurrence of two 500-year floods in 1993 and 2008 (causing the failure of Union Pacific bridge) in the Midwestern United States provides a good example of the impact of changing storms and flooding patterns on bridges [1]. During flooding events bridges may become fully submerged, exerting great amounts of pressure on bridge infrastructure, which can result in shearing or overturning of the bridge deck and ultimately bridge failure.

Although it is assumed that bridge failure might happen during a 100-year flood, in the USA it is estimated that more than 65 per cent of bridge failures have happened during floods with return periods of less than 100 years [2]. This statistic suggests two things: 1- due to changes in climate, land-use, and stream flow regulations the probability of occurrence of severe flooding is higher. 2- The knowledge informing bridge design regulations is inadequate.

Although in reality there are various reasons for bridge collapse, the causes of bridge collapse can generally be divided into the following groups:
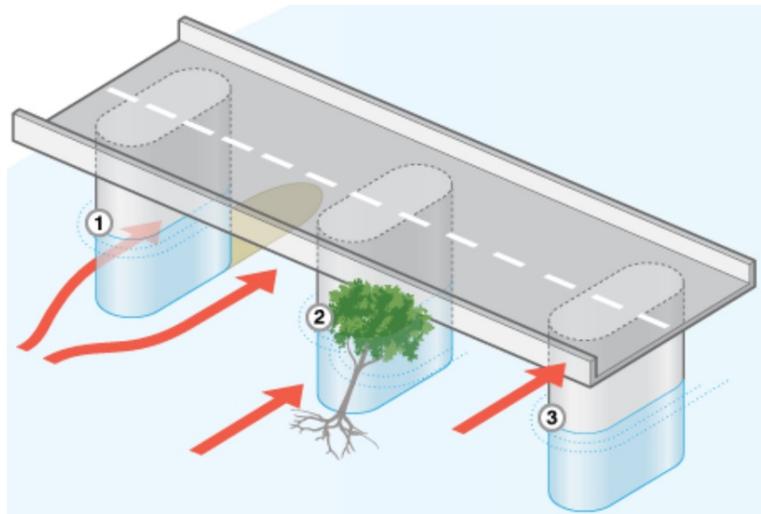
Figure 1- 1. Possible causes of bridge failure [3]

- Removal of the riverbed in upstream of piers due to high-speed turbulent flow
- Significant force due to torrent of water and debris
- Immerse pressure when the bridge is partly or fully submerged
- Wave force on bridge decks or piles

Further, the numerous types of damage to bridges can be divided into two general categories: damage to superstructure and damage to substructure [4]. The main causes of failures of substructures are a settlement of the embankment and scouring around bridge piles. Regarding the failures of superstructures, causes range from the partial displacement of decks to the complete failure of decks.

The magnitude and severity of these damages are related to both hydraulic parameters and the bridge geometry.

The focus of this study is on the failure of submerged small river bridges during strong rainfall events, especially when flotsam and debris obstruct flow under the girder. Failure of bridges due to scour near the foundation or due to wave force is out of the scope of this research.

1.2. Motivation and Research Significance

Bridges are essential components of a nation's transportation system. Damage or failure of such crucial infrastructure can disrupt the natural flow of life and cost huge amounts of money. Several bridges failures have been recorded in the last few decades. Some of the most prominent ones that heavily paralyzed the flooded areas are:

➢ Miscellaneous damage to 500 bridges in Georgia due to Alberto storm in 1994. Scouring and bridge overtopping were the main causes of failure [5].

➢ Flooding during Hurricane Ivan (2004) in the Escambia Bay caused a surge of 10.7 ft and severely damaged the I-10 Bridge [6].

➢ Three main bridges in Louisiana (I-10 Bridge) and Mississippi (US 90 bridges over St. Louis and Biloxi Bay) were brought down by Hurricane Katrina in 2005 [6].

➢ An enormous flood in Georgia (2009) with a return period of 500 years caused significant damages to bridges in Atlanta [7].

➢ More than 100 bridge failures were reported after 2011 Tohoku Tsunami [8]. In most of these cases, a weak connection of bridge superstructure to the pier was recognized as the main cause of failure which ultimately resulted in the displacement of bridge deck [9].
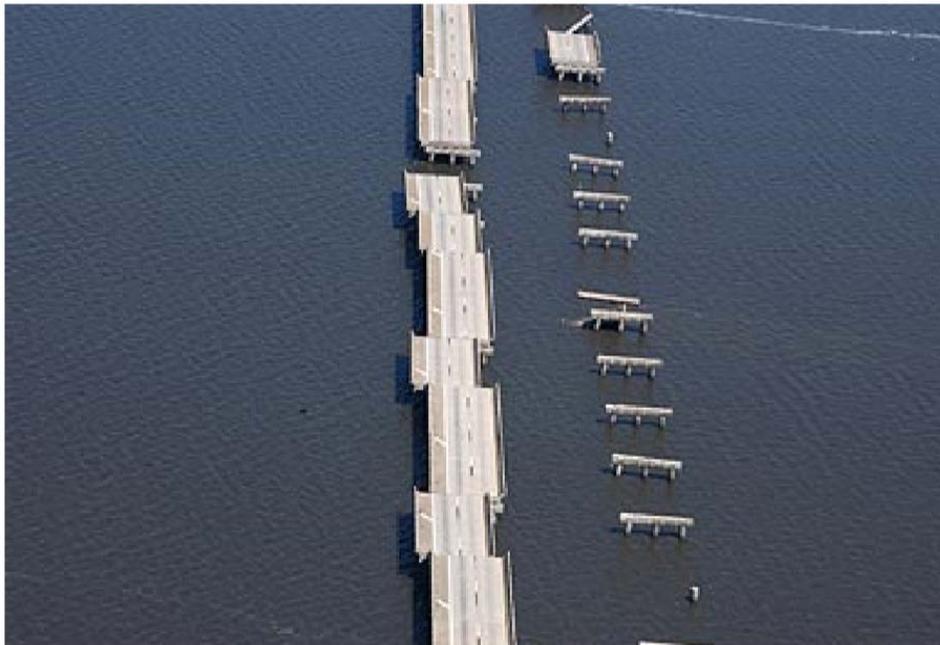
Figure 1- 2. Severe damage to Escambia Bay Bridge after Hurricane Ivan [6].

These examples are just a few of many global bridge failures, which clearly highlights the lack of thorough knowledge and the need for more research in this area. This lack of research is especially pronounced in the case of failure of small river bridges, which are often based on spread footings at locations where bedrock can be accessed. These bridges can become submerged during strong rainfall events, especially when flotsam and debris obstruct flow under the girder. Field observations show a similar pattern of failure for many such events, with the piers lying rotated 90°, top side facing downstream, and the girder further downstream, indicating the entire pier/girder unit was pushed over by a hydrodynamic force. Research into this type of failure is mostly limited to on-site surveys which try to explain the failure processes. Some scaled physical modelling that has been limited to a small range of floods condition was also conducted to asses this type of failure.

Figure 1- 3 Collapse of Abashiri River Bridge in Japan (photo by Jeremy Bricker). Indicating that entire pier/girder unit was pushed over by hydrodynamic force.

Figure 1- 4 Collapse of Abashiri River Bridge in Japan (photo by Jeremy Bricker). Indicating the probable role of debris in the collapse process.

Verifying the mechanism of this failure is the first step toward designing effective countermeasures. In order to obtain a better design method for bridges and to avoid the collapse of submerged bridges (by adopting appropriate counter measures), more accurate estimation of the loading on structures caused by flow is required.

Although bridge stability for several flood conditions has been studied by scaled experiments and documented in the literature, they are limited to a few design and flood conditions due to cost and time limitations. Moreover, channel geometry and bed roughness might influence stresses and hence forces on a bridge [10]. Parallel computers and significant advances in Computational Fluid Dynamics software

have enabled us to overcome such limitations. CFD simulations provide a sophisticated method to directly evaluate the stability of real case bridges for a wide range of flood conditions and design parameters.

By applying a CFD model, this thesis study aims to investigate the hydrodynamic loadings on bridges and to assess how accurately the proposed model can predicting flow forces and bridge failures. The findings can be applied to assessing proposed counter measures for bridge failure and to inform regulations founded on more comprehensive knowledge of the mechanisms leading to bridge collapse.

1.3. Research objective and questions
The main goal of this study can be defined as:

> **To verify the mechanism of failure of bridge decks in order to design countermeasures.**

The second objective is to assess the application of the Fluent model for analysing submerged bridge failure.

To achieve the main objectives of the research the following questions need to be answered:

- o What are the critical hydrodynamic situations that lead to the failure of river bridges?
- o Based on the results of simulations, what countermeasures can be proposed to avoid such failure mechanisms?

1.4 Research Approach and Thesis Structure
This research is divided into 5 chapters.

Chapter 1 describes the motivation, research significance, and general approach to the study.

Chapter 2 introduces the reader to a brief theory behind the loadings on the bridges, the structure of bridges, and basic concepts of hydrodynamic characteristic of flow around a bluff body. Further, the relevant literature related to both experimental and numerical simulations of hydrodynamic loadings on bridges are discussed.

Chapter 3 presents the CFD model and its validation for a small-scale, two-dimensional (2D) flow over the bridge deck. The lift and drag force and overturning moment on the bridge deck are compared with results from physical modelling.

Chapter 4 presents the main results obtained from the numerical simulations. Effects of inundation ratio (h^*), proximity to the bed (Pr), and Froude number (F_r) on bridge failure are investigated and results are presented. Moreover, incipient failure analysis is presented in this chapter. Based on the results, countermeasures for the stability of bridges are proposed.

Chapter 5 summarizes the conclusions, limitations, and recommendations for future work.

2 Literature Review

This chapter provides the reader with a fundamental background on fluid-structure interaction, as it provides the foundation required to investigate the failure of bridges. First, part of this chapter introduces different elements of bridges that are within the scope of this research. The second part is dedicated to the hydraulic features of flow around a submerged body. In the third part, the theory of hydrodynamic loadings on bridge are briefly presented. The remainder of this chapter is dedicated to outlining previous research on the hydrodynamic failure of bridges. Failures due to tsunamis, river floods, and storm surges are presented. For each of these failure mechanisms, the most recent and comprehensive field surveys, numerical and experimental studies are presented.

2.1 Bridge structure type

Various types of bridges can be found around the world, and each of them has its own characteristics. It is not possible to study all bridge types in existence, so the most common superstructure, support structure and foundation bridge types are briefly described in the following paragraphs.

The three most commonly used types of bridge superstructures are: slab, girder with slab on top, and box girder spans. The response of each of these superstructures can be different under flood conditions. The focus of this study is on the deck with girders.
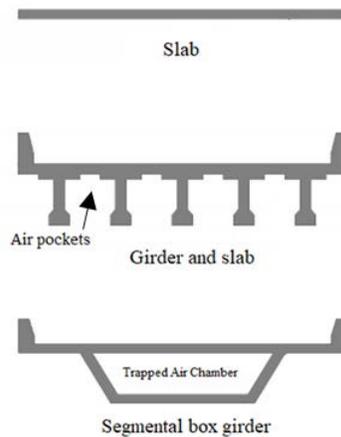
Figure 2- 1 Three most common Bridge superstructures shape.

Another important factor that will affect the failure mechanism of a bridge is the connection between decks and connections between deck and piers. The deck might be simply placed on the pile cap without any further supports (type A in *Figure 2- 3*). Several decks could also be connected to each other and form a continuous deck unit (type B in *Figure 2- 3*) *[6]*. Loads from spans to piers are transferred by bearings. Movements are accommodated by a combination of methods such as rolling, sliding and deformation *[11]*. One of the most common types of bearing for small bridges is reinforced elastomeric bearing which is made of rubber with several layers of steel plate inside that.
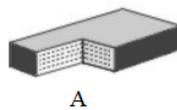
Figure 2- 2 Elastomeric Bearing.
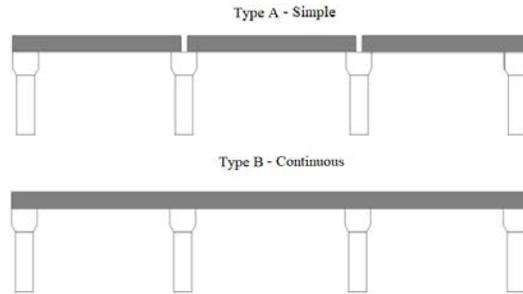
Figure 2- 3 Simple and Continuous types of deck-deck and deck-piers connections.

Foundations of a bridge are also important as they carry the entire weight of the bridge as well as traffic loads on the bridge. Foundation failures in bridges are one of the main causes of the collapse of bridges and other structures. Spread footing and pilling are two well-known types of foundations on bridges. Spread footing is the simplest type of foundation. It distributes loads over a larger area of supporting soil or rock so that the resulting pressure is less than the soil bearing capacity. If the soil is not strong enough to withstand loadings, piles might be driven deeper into the soil to transfer loads to a stronger soil or bed rock layer. The choice of foundation depends on several factors including the depth, the bearing capacity of the subsoil, and the allowable settlement, which is related to deck type.
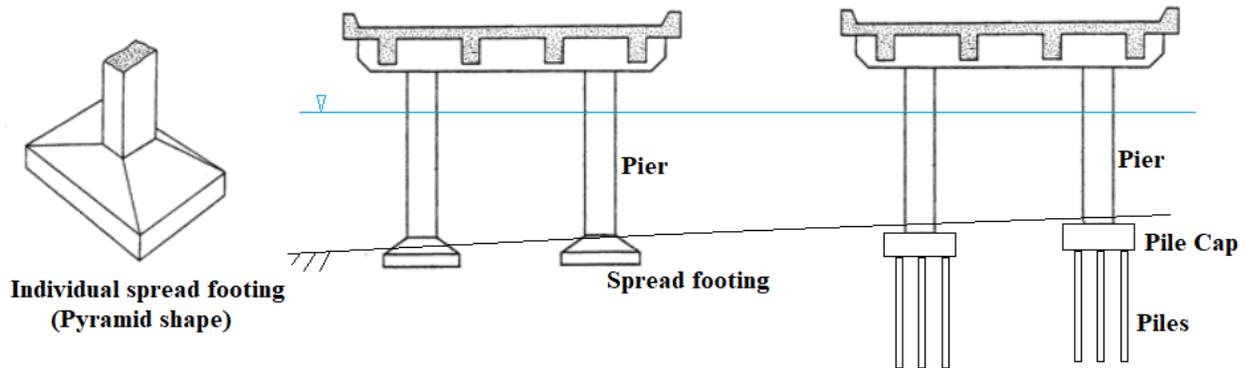
Figure 2- 4 Left: Sketch showing typical pyramid shape spread footing. Middle: Cross section of bridge with spread footing. Right: Cross section of bridge with piles.

2.2 Bluff body hydrodynamics

In a general term, when flow separation occurs around a body subjected to fluid flow, the drag would be dominated by pressure drag, and the body is often called a bluff body. The flow field around a bluff body is usually complex and variable in time and space. Bridge superstructures and piers that are partly or fully submerged underwater are considered as bluff bodies. For flow characterized by a high Reynolds number, flow around a bluff body can be described as below:

9
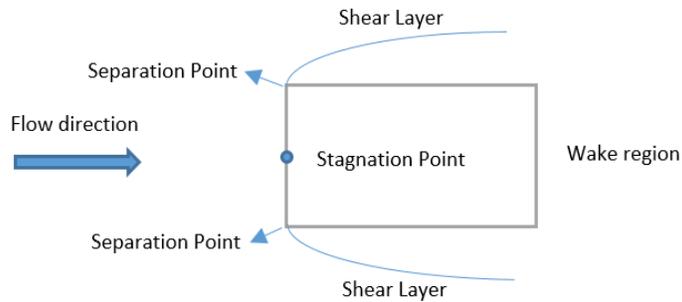
Figure 2- 5 Flow around a bluff body

Considering p_0 and v_0 as static free stream pressure and free stream velocity respectively. According to Bernoulli's equation, the pressure on the surface of the body (p) should be smaller than p_0, on the locations on the surface of the body that have a higher velocity than v_0. Similarly, for locations on the surface of the body with a smaller velocity than v_0, the pressure should be higher than p_0. Dimensionless pressure coefficient C_P can be defined as follows:

$$C_p = \frac{p - p_0}{\frac{1}{2}\rho V_0^2}$$

(2-1)

The point at which boundary layer detaches from the body is called the *separation point*. Two types of *separation points* can be defined as follows:

- ➢ In objects like a bridge deck with sharp corners or the body shown in Figure 2- 5, the separation point is easily considered as the sharp corner of the leading edges. This flow separation can dramatically increase pressure drag by inducing a pressure gradient between the leading and trailing edge of the body. For very small Reynolds numbers, flow will be attached to the surface of the body, and there might be no sign of separation.
- ➢ Consider an object with a continuous surface and without sharp corners as shown in below figure. Due to the shape of the object, at point A the pressure gradient is favourable, which means pressure difference reinforces the fluid flow in its own direction. This continues until point B. Consider there is an adverse pressure gradient at point D. If this adverse pressure gradient is strong enough, it will start to move upwards towards point A. The velocity close to the wall reduces until point C when no more retardation of flow is possible unless the flow reverses completely. At this point shear stress is zero, separation of the boundary layer occurs, and an area of recirculation flow downstream of point C forms. It should be noted that due to the higher kinetic energy of turbulent flow there would be a delay in the occurrence of separation, and it would occur further downstream for a turbulent flow [12].
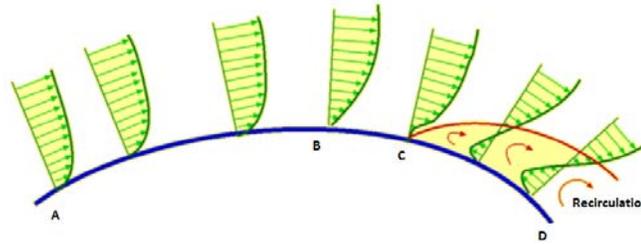
Figure 2- 6 Separation of flow over a continuous body

In the case of a continuous body without sharp corners, by increasing the turbulent intensity of flow and surface roughness, the changes from laminar to turbulent boundary layer can occur at smaller R_e. However, these two parameters do not change the separation point of a body with sharp corners.

The location where shear flow once again attaches to the surface of the body is called *reattachment point*. Several factors contribute to the reattachment of the flow including flow characteristics and shape of the bluff body. If conditions are favourable and reattachment occurs, the flow might undergo another separation of the boundary layer at the sharp edge on the back side of the body.

According to the Bernoulli equation, the pressure is maximum at the point where flow encounters an object and the fluid velocity is reduced to zero. This point is often called the *stagnation point*. For incompressible flow, the stagnation pressure is equal to the total pressure and hence the pressure coefficient C_p is one at this point.

At the trailing side of the body, the boundary layer detaches from the body and forms a low-pressure area which is called a *wake*. For high Reynolds numbers, the wake is significantly turbulent and eddies are dominant in that area. The wake area has a high effect on drag magnitude. Bigger wake areas correspond to higher drag.

2.3 Theory of loadings on inundated bridges

The structural response of bridges under flood conditions is highly dependent on fluid characteristics and also the configuration of the bridge. To be consistent with the literature, the parameters for bridge and flume dimensions are chosen as follows:
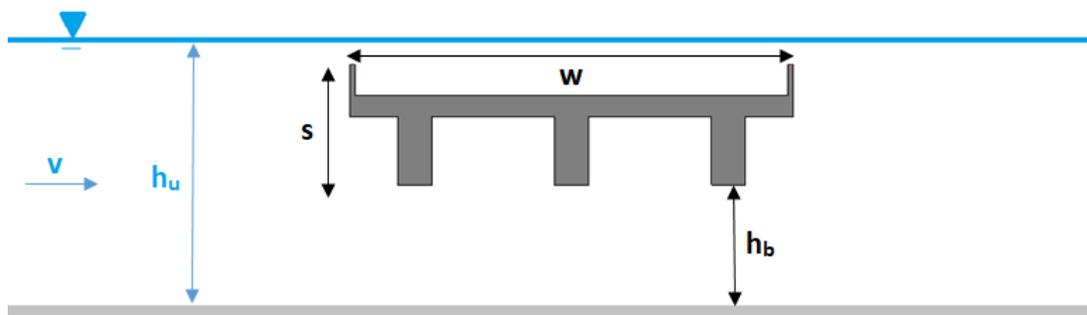
Figure 2- 7 Schematic diagram of a fully submerged three-girder bridge deck. S: deck thickness, W: Bridge width, h_b: distance from the ground to the bottom of the bridge, h_u: height of water from the ground. V: free stream velocity

Based on the upstream flow depth, the elevation of the bridge, and deck thickness, several inundation ratios (h_*) can exist:

$$h_* = \frac{h_u - h_b}{s} \tag{2-2}$$

$h_* = 0$, represents the situation where the water level is at the bottom side of the girders, and $h_* = 1$ describes the case where the water level is at top of the railings. Higher values of h_* mean that the bridge is more submerged.

The blockage ratio (B_r) and the proximity ratio (P_r) can be also defined as:

$$B_r = \frac{s}{h_u} \tag{2-3}$$

$$P_r = \frac{h_b}{s} \tag{2-4}$$

Three main responses of the submerged bridge deck which are of high importance for this research are shown in the below figure:
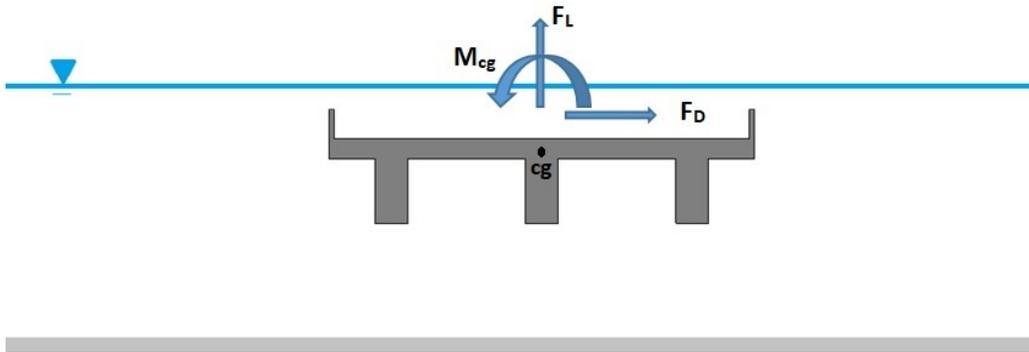
Figure 2- 8 Drag and Lift forces and centroidal moment acting on the bridge deck.

The presence of viscosity results in forces acting parallel to the flow direction which are termed *wall shear stresses*. Forces normal to the flow direction which exist due to pressure are also termed *normal stresses.* The component of the resultant of shear and pressure forces in the flow direction is the *drag force* and the component that acts normal to the direction of flow is the *lift* force [13]. As far as forces on bridges are concerned, the effect of surface tension is negligible. Despite these clear definitions of drag and lift, deriving a widely applicable, precise formula is difficult due to the dependence of force coefficients on the bridge shape.

The horizontal stability of the bridge deck might be threatened by the forces acting parallel to the flow direction, F_D, Drag forces:

$$F_D = \frac{1}{2}C_D\rho V^2(SL) \quad if\ h_* \geq 1 \tag{2-5}$$

$$F_D = \frac{1}{2} C_D \rho V^2 (h_u - h_b)\, L \quad if\ h_* < 1 \tag{2-6}$$

Where F_d is the drag force (N); C_D drag coefficient (non-dimensional); ρ density of water (kg/m3); V free stream velocity (m/s); A is the reference area for drag (m^2); h_u height of water from the ground(m); h_b distance from the ground to the bottom of the girder(m); L bridge length (m).

Similarly, the vertical stability of the bridge deck depends on the forces acting perpendicular to the flow direction, F$_L$, Lift forces:

$$F_L = \frac{1}{2} C_L \rho V^2 (WL) \tag{2-7}$$

Where F$_L$ is the lift force (N); C_l lift coefficient (non-dimensional);

For the case of fully or partially submerged bridges, the buoyancy force (F$_B$) also acts in the direction of lift:

$$F_B = \rho g V' \tag{2-8}$$

Where V' is the volume of liquid displaced (m^3).

In order to have a non-dimensional C$_L$ that is consistent with C$_D$ and C$_M$, F$_b$ should be excluded from F$_L$. Therefore, C$_L$ refers only to the effect of lift (and excludes the effect of buoyancy).

In case of an uneven distribution of forces, the moment about the centre of gravity, M$_{cg}$, might be sufficient to rotate the bridge decks:

$$M_{cg} = \frac{1}{2} C_M \rho V^2 (W^2 L) \tag{2-9}$$

Where C$_M$ is the momentum coefficient.

During flood events, heavy floating objects such as cars or cabins can induce impact forces on bridge decks and piers. This impact force has been studied by several authors, and different equations for calculating this force has been proposed such as [14]:

$$F = CF \left(\frac{MV''^2}{x} \right) \tag{2-10}$$

Where F is the impact force, M is the effective mass of debris, V'' is the debris velocity, x is the stopping distance, and CF is the correction factor which accounts for several factors.

However, this impact force is only relevant when a heavy object hits the bridge structure, which is not the common case. The type and magnitude of debris are highly dependent on the catchment vegetation, surrounding land uses, and the severity of the flood. Although in reality there are countless shapes and forms of debris with different permeabilities, roughnesses, and characteristics, the general process of debris mat formation in front of the bridge can be defined as follows: a tree with a height exceeding the deck height or the distance between two piers hits the bridge. Then, other smaller trees also get stuck, which traps other types of debris, such as bushes, that attach to the trees and form a bigger debris mat. This debris mat causes elevated water levels and increased pressure in front of the bridge, which can ultimately lead to the failure of the bridge.

The key point here is the shape of the debris. Is it possible to categorize the shape of the debris mat in front of bridges? The difficulty comes from the fact that during floods it is quite difficult to be close enough to the bridge to observe and record the shape of the debris mat. However, several field studies have been done in the USA to categorize the shape of the debris mat in front of bridges [6]. The summary of these studies are as follows:
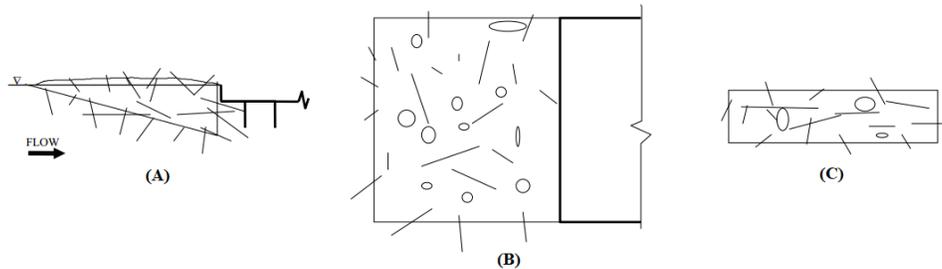
Figure 2- 9 Common form of debris at bridge deck observed in the USA. Left (Side view (A)), right (Plan view (B)) bottom (Front view(C)) [6].
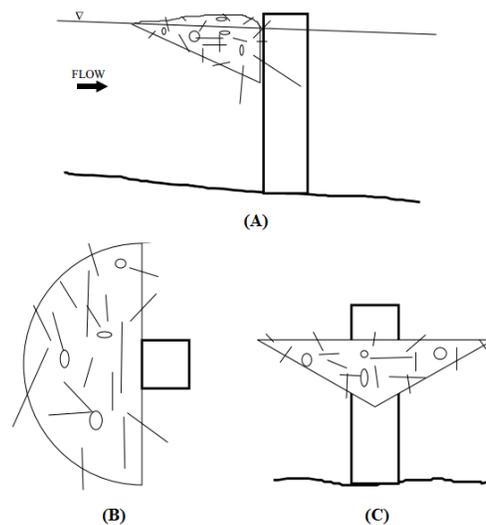
Figure 2- 10 Common form of debris at bridge pier observed in the USA. (Side view (A)), (Plan view (B)), (Front view(C)) [6].

2.4 Review of field survey, numerical and experimental researches on bridge stability

In this section a review of relevant experimental and numerical fluid forces on bridges is presented. Although the main causes of submerged bridge failures are quite similar for river floods, storm surges, and tsunamis, there are some differences in the physics and boundary conditions of each of these situations. Therefore, this section of the report is divided into three categories of hydrodynamic bridge failure caused by tsunamis, river floods, and storm surges. Each category is also divided into the following 3 subcategories: field surveys, numerical simulations, and physical modelling.

In the special case of the collapse of a river bridge, the bounded domain might lead to a deviation of forces coefficient from the cases of infinite domains. For very large rivers and bridges with high freeboard, the system shifts towards an unbounded domain and the effects of channel walls and the floor become negligible. However, this case rarely exists in reality and its application is severely limited.

Tsunami

Different mechanisms of bridge failure during past major tsunamis are determined. In this section, only the failure of the superstructure of bridges is considered. The failure of the bridge piers under tsunami conditions is related to the bridge substructure and is of less importance based on the scope of this research.

Field surveys
Utatsu bridge (2011)

Tohoku Tsunami, which occurred as a result of the 2011 Great East Japan Earthquake, damaged almost 300 bridges on the east coast of Japan [15]. The state of the Utastsu highway bridge after the tsunami is shown in the picture below.

Figure 2- 11 Utastsu bridge situation after Tohoku Tsunami (2011) [15].

As seen in the picture, the piers remained intact while superstructures were washed away, which indicates the lack of proper connections between superstructures and piers. Another interesting observation is the rotation of deck numbers S8 to S10 after being floated and pushed by the tsunami, Figure 2- 12.

Figure 2- 12 Utastsu bridge situation after the Tohoku Tsunami (2011) [16].

The mechanism of this type of failure is shown below. In the case where the deck floats after being uplifted, installation of vertical restraints between decks and piers is suggested [16].
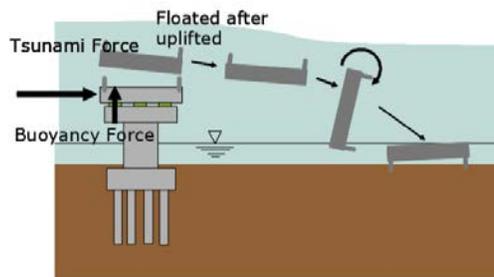
Figure 2- 13 Mechanism of failure of decks that were rotated after being submerged by tsunami [16].

Hirouchibashi bridge (2011)

Unlike the Utatsu Bridge, in this case, the deck was only moved horizontally without being overturned. The absence of critical damages to anchor bars suggests that the deck must have been lifted up before it was moved landward.

Figure 2- 14 Horizontal movement of bridge deck towards landside during tsunami (left picture). Absence of damage to anchor bars on the seaward side (right picture) [17].

Numerical simulations

Bricker et al. (2014) investigated the failure of the Utatsu Bridge during the 2011 Great East Japan Tsunami. By applying a two-dimensional OpenFOAM model, lift and drag forces and overturning moments on the bridge were calculated. Results showed that several factors contributed in the failure of the bridge including the seawall on the landward side of the bridge, the inclination of the deck, the amount of sediment in the water, and the air trapped between girders. The following aspects of their work also are of high importance:

➢ Bridge failure could not have happened without being fully submerged.
➢ The presence of a seawall near the bridge elevated the hydrodynamic forces dramatically and can be seen as the main cause of the transverse variation of displaced deck locations.
➢ The drag force for the inclined-deck (base) case increased initially as the submergence ratio increased. After this initial increase, it reached the constant value with small variations.
➢ The lift force also increased with increasing submergence ratio as buoyance force outweighed the downward force due to the acceleration of flow below the deck. Although after the full submergence of bridge the buoyancy force remained constant, due to lower flow speed under the deck and increase of flow speed above the deck, lift force continued to increase. The overturning moment followed the same trend as the lift force.
➢ Flow separation and hence lower pressure on the top seaward side of the deck, which was caused by the inclination of the deck, contributed greatly to the overturning moment of the deck. This flow separation for a level deck was much smaller than for the inclined deck [18].

Another recent study on the failure of the Utatsu Bridge was done by Salem et al. (2014). The Applied Element Method (AEM) which is included in Extreme loading for structures software (ELS), was used to simulate a 3D collapse of the bridge superstructure. One of the advantages of using the AEM method is that it is capable of capturing large deformations of structures under severe forces such as tsunamis. Another advantage of AEM over the Finite element method (FEM) is that it is more computationally efficient. However, since ELS is made for structural analysis, it is not able to model fluid-structure interaction and the pressures of fluid acting on structures should be input into the software or should be estimated based on the iterative approach with some simplification. Results of their study showed that AEM can successfully simulate bridge collapse in structural aspects. The findings also suggested that trapped air between girders played a key role in bridge collapse [19].

Bricker et al. (2015) investigated the causes of failure of the Hirouchi-bashi bridge, which occurred due to the Great East Japan tsunami (2011). The main aspects of their research related to this thesis are as follows:

➢ The Kobe University Large Eddy Simulation (KULES) code coupled with solid body motion analysis was applied to simulate flow solid-body interaction. Moreover, the whole bridge deck including four girders and the slab are assumed as one solid body.
➢ Three scenarios were considered:
  1- The deck is fully submerged (the top of deck 1 metre below water level) with a steady flow (5m/s, which is a probable speed of tsunami at that location). In this case, forces are not capable of moving the deck and applying higher velocities only increases downward forces. Moreover, three areas of rapid flow with low pressure are recognized to be below and above the seaward edge of the deck and the area near the landward edge.
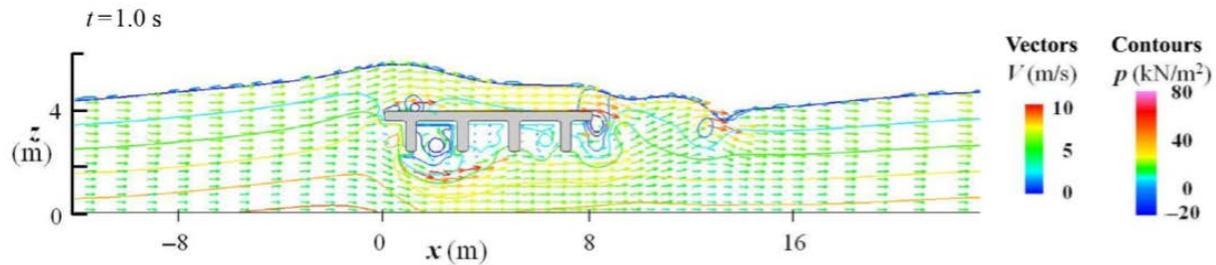
Figure 2- 15 Three areas of high velocity adjacent to bridge [17].

2- The deck is just above water level and wave height of 2 m with a flow speed of 5m/s hits the structure. In this situation, noticeable vertical forces can occur [20]. Though at first, the uplift force is quite high, it gradually reduces as water starts to flow over the deck.

3- The deck is fully submerged at a flow speed of 1m/s. This results in maximum buoyancy force and a negligible downward force. A wave of 1 m height with a flow speed of 5 m/s was also considered in this scenario. When higher flow speeds reach the bridge due to the blockage effect, the water level and pressure increases, resulting in a higher overturning moment and finally rotation of the deck. The small horizontal wave force is then enough to push the deck horizontally.

Authors concluded that wave surge of high flow velocity on a fully submerged deck can increase the moment enough to tilt the bridge deck. After reaching this point, the lift force also increases considerably, resulting in the complete separation of the deck from abutments [17].

Physical experiments

Maruyama et al. (2013) performed a 1/10 relatively large-scale physical experiment to assess the forces caused by the tsunami on bridge girders of the Numata overpass. They investigated the influence of flood velocity, water depth, and a solitary wave.

➢ For the case of uniform flow, several submergence ratios from 1 to 4.6 were considered. Results showed that for all submergence ratios, the uplift forces were negative, meaning that decks were pushed downward. By increasing the velocity, this downward force also increased. As a result, no movement of the deck was recognized in this case.

➢ In the case of a solitary wave, submergence ratios of 0 to 2 were considered. Results indicated that the deck was easily moved when the submergence ratio was 0 and the solitary wave hit the deck.

➢ They also recognized the role of trapped air during inundation, which results in additional buoyancy. Results revealed that the presence of air-vents could notably reduce uplift force [21].

River flood

Field surveys

One of the most recent river bridge failures is the collapse of Hammond Bridge near Dora in the USA, which occurred after heavy flooding in April 2017. After being fully submerged by 10 feet of water above the deck, the bridge deck was washed a hundred metres downstream and settled on the river bank. Although no scientific research has been done yet on this failure, lack of damage to the leading side of

one of the pier caps and damage to the rear side of the cap suggests that the deck might have been uplifted on the leading side and then pushed away in a horizontal direction by the flood and debris. One of the two piers of the bridge had completely collapsed.

Figure 2- 16 Hammond Bridge before 2017 flood (left) [22], Hammond Bridge after the flood(middle), Lack of damage to the leading side of the pier cap and presence of damage and scratch on the trailing side(right) [23].

Numerical simulations

Chu et al. (2012) investigated the effect of the blockage ratio, Froude number, and the submergence ratio on the forces exerted on the fully submerged bridge. By solving the Navier-Stokes equations and applying an LES model they simulated the flow field. The free surface was also captured by a VoF model. Important aspects of their work are as follows:

➢ The drag coefficient increased as h^* increased from zero to one, simply due to an increase of the frontal submerged area. However, for h^* values higher than 1.2, the drag coefficient started to decrease due to changes in the blockage ratio. For h^* values higher than 4, the drag coefficient became nearly constant around 1.8.

➢ The lift coefficient started with negative values and continued to decrease when $h^* < 1$. After the deck is fully submerged the lift coefficient increased and levelled off to around zero for $h^* > 3.5$ due to the fact that pressure is symmetric on the upper and lower part of the deck.

➢ By considering a constant inundation ratio of 2, the results show that by increasing the blockage ratio in the subcritical flow the drag coefficient increases. This is due to the higher pressure on the front side of the deck and lower pressure on the back side. This indicates that a drag coefficient around 2~2.2 suggested by Hamill (1999) cannot be considered for bridges with blockage ratios higher than 0.23 [24].

Patil et al. (2009) applied STAR-CD software to analyse the forces on bridge-decks for a wide range of flooding conditions on open channel flows. Their 2D simulation results showed significant variation in changing turbulence models. After comparing the results with the experimental model of the Turner

Fairbank Highway Research Center (TFHRC), they concluded that the RNG turbulence model gives more reliable results. The variation of the lift coefficient in their results was in agreement with the results of Bricker et al. (2014).

Physical experiments

Jempson M, (2000) performed a scaled experiment to assess the effect of flood, debris, Froude number, submergence ratio, and distance of superstructure from the bottom channel, on drag, lift, and moment coefficients. Six types of superstructures and three types of piers were included in more than 500 physical experiment tests. The result of his experiment provides a valuable data set that can be used for further studies on loading of flood and debris on submerged bridges. Based on the results, design charts and revised methodology for calculating loadings on fully and partially submerged bridges were proposed. Results also revealed that the proposed drag coefficient in the Australian bridge design code is relatively low when there is debris in the flood.

Malavasi and Guadagnini (2005) analysed the hydrodynamic loadings on a bridge deck with a rectangular cross-section for several submergence and Deck Froude numbers. They suggested a Deck Froude number as follows:

$$F_s = \frac{V}{\sqrt{gs}}$$
(2-11)

The main findings of their report that are of importance for this thesis are as follows:

➢ When a bridge is fully submerged and the flow velocity is very low, the worst situation in terms of the vertical stability of the deck is most likely.
➢ Inundation ratio and Deck Froude number play key roles in determining the magnitude of moment and force coefficients.
➢ A drag coefficient of 3.4 for a practical flow range was suggested as an upper boundary limit. This upper limit can be considered for a ratio of deck length to deck thickness of three or higher.
➢ In order to fully understand the behaviour of C_D and C_L on bridge decks, more detailed information of the flow field around a bridge is required, which can be achieved by numerical simulation [25].

The U.S. Department of Transportation in 2009 published a report on the hydrodynamic forces on inundated bridge decks based on both physical experiments and numerical simulations. Two- and three-dimensional simulations were done using the Fluent and STAR-CD software. Three types of bridges, including six and three girders and streamlined deck shapes, were investigated against lift and drag forces and overturning moments. The following points related to the scope of this thesis can be extracted from this research:

➢ By comparing the results of the 2-D model with the 3-D model, it was concluded that a 2-D model can be reliable for calculating forces and moments on bridge decks. However, more detailed information could be extracted from a 3-D model.
➢ In the case of a Fluent model, an unstructured mesh was applied. The Volume of Fluid (VoF) method was used to capture free surface elevation. K-ε and an LES (Large Eddy Simulation)

turbulence model was used as a turbulence model. Results of the LES model were more reliable but required longer computation time.

➢ For the case of traditional six girders bridges, the drag coefficient shows a drop as inundation ratio (h^*) is between 0.5 to 0.8. This reduction in drag force happens when the water level starts to inundate the top of the girders and to overtop the deck. At higher inundation ratios of 1.5, the drag coefficient becomes almost constant with a value of 2. This trend is also seen for three girder bridges, where the final drag coefficient levelled off to around 1.8.

➢ Experimental results revealed that lift coefficients are negative for all inundation ratios for six girder bridges. The minimum lift coefficient occurs at $h^* = 0.65$ and it starts to increase and returned to its initial 0 value as the inundation ratio exceeds 3. This trend is also seen for three girder bridges. However, the minimum value is more negative, in this case.

➢ The peak moment coefficient occurs when the bridge is almost halfway inundated. By increasing inundation ratios, moment coefficients decrease and when h^* is around 1.7 it becomes negative for Froude numbers higher than 0.28 [13].

Storm surge

Field surveys

During Hurricane Katrina, I-10 Twin Span Bridge over Lake Pontchartrain was damaged significantly. The collapse of this bridge was puzzling because the two nearby bridges only experienced slight damage. Two types of span failure were recognized by field surveys: 1. Partial or complete failure of spans into the water. 2- Lateral displacement of spans which was confined by the existence of pedestals.

Figure 2- 17 Total displacement of spans. One end of span in the water, another side on the bent cap beam [26].
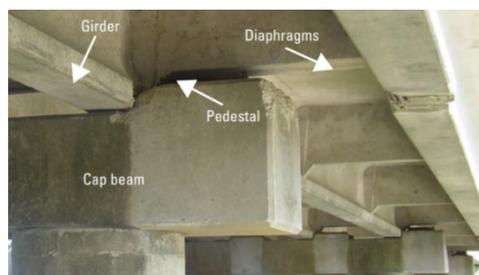
Figure 2- 18 Lateral displacement of deck to the point which was stopped by pedestal [26].

At first glance, the lateral displacement of spans might indicate that wave forces and storm surge currents are responsible for this lateral movement. However, this idea is not supported by the field survey, where

21

no significant damage to girders or the cap beam was observed. Considering the failure mechanism of the I-10 Twin Span Bridge and comparing the differences in the superstructure of the bridge with that of two nearby bridges that only underwent small damages suggests that the role of trapped air in increasing the uplift force and reducing frictional resistance must have been significant. In fact, the existence of holes in diaphragms and the smaller height of girders led to less trapped air and hence less damage of Highway 11 Bridge (adjacent to the I-10 bridge).

Numerical simulations

During Hurricane Ivan in 2004, more than 120 spans of Escambia Bay Bridge were damaged. Considering the relatively sheltered and shallow area near the bridge, large waves could not reach the bridge. In order to answer the question of what was the main cause and situation that led to the failure of the superstructure of this bridge, Huang et al. (2009) performed a numerical test model. The numerical model was set based on the Reynolds averaged Navier-Stokes equation. The k-ε turbulence model was applied and the VOF method was employed to capture the free surface level. In their numerical simulation, three locations of bridge deck bottom were considered: ¼ of wave height above surge elevation, ¼ of wave height below surge elevation, and at surge water elevation. The results showed that when the bottom of the deck was at storm surge level, the uplift force was significant enough to lift the deck, which was then pushed away by horizontal wave force. It was also concluded that when the elevation of the bridge deck is ¼ of wave height higher than the surge level, the uplift force is not capable of lifting the bridge deck. However, the horizontal force exerted by waves is strong enough to overcome the horizontal friction force [27].

Chen et al. (2009) also investigated several highway-bridge collapses in the Gulf Coast that occurred after Hurricane Katrina. By employing an ADCIRC model, they calculated surge height and velocity. Wave characteristics were simulated by applying a SWAN model. It was concluded that the heightened water level due to storm surge and subsequent wind waves were responsible for the bridge deck failure [28].

Physical experiments

In order to investigate the role of air trapped beneath a bridge deck, Chen et al. (2005) performed a laboratory test. They modelled the bridge deck as a simple box with the open face downwards. The results of their experiment showed that an increase in buoyancy and the resulting reduction of frictional resistance were the main causes of the failing of the bridge deck. They concluded that under this condition even a relatively small horizontal force can easily push away the bridge deck. After the removal of trapped air, the deck settled again but in a different location. However, the exact role of storm surge and wave action remains unclear [26].

2.5 Review of hydrodynamic forces for on bridge superstructure based on international standards

A summary of international standards for calculating hydrodynamic forces on bridge superstructure is presented here. It should be noted that only the relevant parts of each standard are presented here. For a more comprehensive overview of each standard, the reader is referred to the original standard listed in the references section.

2.5.1 Australian Bridge Design code AS 5100

Lift force

Two lift coefficients based on relative submergence are presented in the Australian bridge design code. In order to be conservative, the upper value should be used for calculating the vertical stability of the bridge deck and for the resistance of the bridge to overturning moments. The downward force should be calculated for the required size of foundations, piers and deck girders.
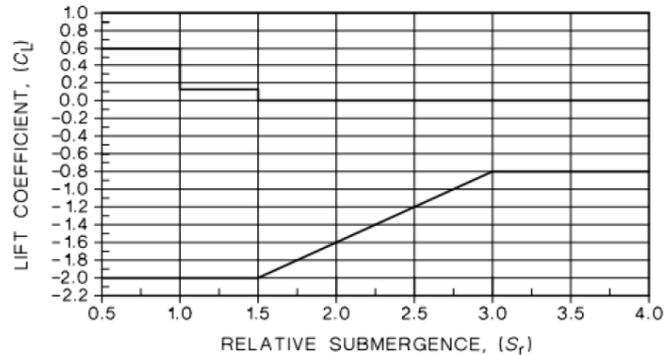
Figure 2- 19. Lift coefficient versus relative submergence based on Australian bridge design code [29].

Drag force

In the Australian design code, the drag force is presented based on the relative submergence and proximity ratio of the bridge as follows:
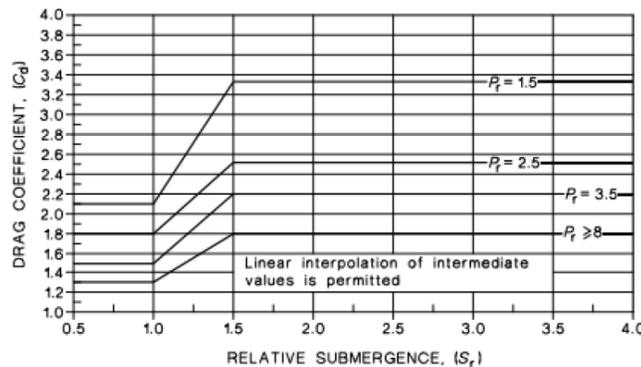
Figure 2- 20. Drag coefficient based on Australian bridge design code [29].

$$S_r = \frac{d_{wgs}}{d_{sp}}$$

(2-12)

S_r: relative submergence

D_{wgs}: vertical distance between upstream water level and deck soffit

D_{sp}: wetted depth of the upstream side of the deck (including railings)

$$p_r = \frac{y_{gs}}{d_{ss}}$$ (2-13)

P_r: Proximity ratio

y_{gs}: vertical distance between deck soffit and channel floor

d_{ss}: wetted depth of the upstream side of the deck (excluding railings)
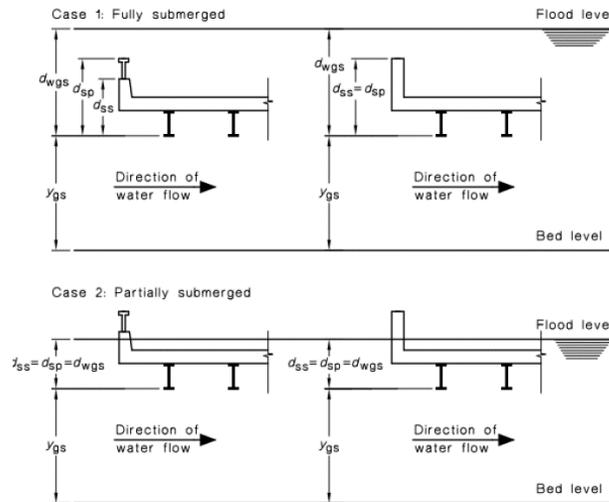
Figure 2- 21. Required parameters for drag force calculation based on Australian bridge design code [29].

2.5.2 Eurocode 1991-1-6

Based on the Eurocode design, three parameters contributing to the hydrodynamic forces on the immersed structures are as follows: water depth, velocity, and shape of the structure. The horizontal force can be determined by:

$$F_{wa} = \frac{1}{2} k \, \rho_{wa} h b \, v_{wa}^2$$ (2-14)

V_{wa} average water velocity (m/s);

P_{wa} water density kg/m3;

H water depth (m);

b width of the structure (m);

K is determined based on the shape of the structure:

K = 1.44 for a rectangular or square cross-section

K= 0.70 for a circular cross-section

3   CFD Modelling using ANSYS – Fluent

The first section of this chapter provides the reader with the fundamental governing equation that are used in the CFD simulation. In the second part the experimental configuration of Federal Highway Administration (FHWA) is presented and numerical model is constructed based on that. The comparison of numerical results with experimental results of FHWA is provided in the third part of this chapter. In the last section, the second validation of model against the experimental data of Malavasi and Guadagnini (2003) is presented.

3.1 Governing Equations

The governing equations that are used in CFD simulations are described in this section. For each time step and each individual cell, these set of equations is solved iteratively to predict the characteristics and location of flow. When the residuals are small enough, the solution is converged, and once again the equations are solved for the next time step.

3.1.1 Navier-Stokes Equations

In a global term, the motion of fluid can be described by Navier-Stokes equations. For a compressible Newtonian fluid, conservation of mass and momentum are described based on the following equations respectively:

$$\frac{\partial \rho}{\partial t} + \nabla.(\rho u) = 0 \tag{3-1}$$

$$\rho \left(\frac{\partial u}{\partial t} + u.\nabla u \right) = -\nabla P + \mu \nabla^2 . u + F \tag{3-2}$$

For incompressible fluid the equations can be rewritten as follows:

$$\frac{\partial U}{\partial x} + \frac{\partial V}{\partial y} + \frac{\partial W}{\partial z} = 0 \tag{3-3}$$

$$\frac{\partial U}{\partial t} + U\frac{\partial U}{\partial x} + V\frac{\partial U}{\partial y} + W\frac{\partial U}{\partial z} = -\frac{1}{\rho}\frac{\partial P}{\partial x} + v\left(\frac{\partial^2 U}{\partial x^2} + \frac{\partial^2 U}{\partial y^2} + \frac{\partial^2 U}{\partial z^2} \right) + F_X \tag{3-4}$$

$$\frac{\partial V}{\partial t} + U\frac{\partial V}{\partial x} + V\frac{\partial V}{\partial y} + W\frac{\partial V}{\partial z} = -\frac{1}{\rho}\frac{\partial P}{\partial y} + v\left(\frac{\partial^2 V}{\partial x^2} + \frac{\partial^2 V}{\partial y^2} + \frac{\partial^2 V}{\partial z^2} \right) + F_Y \tag{3-5}$$

$$\frac{\partial W}{\partial t} + U\frac{\partial W}{\partial x} + V\frac{\partial W}{\partial y} + W\frac{\partial W}{\partial z} = -\frac{1}{\rho}\frac{\partial P}{\partial z} + v\left(\frac{\partial^2 Z}{\partial x^2} + \frac{\partial^2 Z}{\partial y^2} + \frac{\partial^2 Z}{\partial z^2} \right) + F_Z \tag{3-6}$$

Where P is pressure; U, V, and W are velocities in x-, y-, and z-direction respectively; F_X, F_Y, and F_Z are external forces in x-, y-, and z-direction respectively; v is kinematic viscosity; t is time; ρ is fluid density; μ is dynamic viscosity.

The first four terms on the left-hand side of the equation represent inertia forces. The first term on the RHS represents pressure forces. The second term in RHS represents viscous forces and the last term correspond to the external forces.

So far, we have seen that there are 4 equations (1 continuity and 3 conservation of momentum) and also 4 unknowns (3 velocities and 1 pressure). It suggests that by having the magnitude of velocities and pressures at boundaries, the problem can be solved. However, due to non-linearity, analytical solutions can only be found for simple cases when viscosity dominates the whole system.

3.1.2 The RANS Equations

In most of the cases in reality such as river flow, Reynolds number is high and flow is turbulent. In these cases, no exact solution has been found yet and only an approximate numerical solution is possible. Three different approaches can be considered as follows:

- Direct Numerical Simulations (DNS): in which Navier-Stokes equations are numerically solved in an explicit way with all detail time and length scales. However, the application of DNS is limited to simple cases with low Reynolds number as the computational cost of this method is really high.
- Large Eddy Simulations (LES): The main idea of LES is to increase efficiency of the numerical simulation by removing small length scales through a method of low-pass filtering of the NS equations. The larger motions that have a higher influence in the flow field are resolved.
- Reynolds-averaged Navier-Stokes (RANS): RANS is the most common method that provides a less accurate but pragmatic way. This method is used in this thesis and described in more details in the following paragraphs.

Reynolds decomposition is used to derive the RANS equation from NS equations. Velocity and pressure are decomposed into an ensemble average and a fluctuating part.

$$u_i = \bar{u} + u'$$
(3-7)

$$P = \bar{p} + p'$$
(3-8)

Inserting Reynolds decomposition for velocity and pressure into the NS equations, and after averaging of the equations, the RANS equation will be derived.

$$\rho(\frac{\partial}{\partial t}(\bar{u}_i) + \frac{\partial}{\partial x_j}(\bar{u}_i \bar{u}_j)) = -\frac{\partial \bar{p}}{\partial x_i} + \mu \frac{\partial^2 \bar{u}_i}{\partial x_j \partial x_i} + \bar{F}_i - \frac{\partial}{\partial x_j}(\rho \overline{u'_i u'_j})$$
(3-9)

This equation has an extra term in comparison with the NS equations. The last term on the right-hand side of the equation has been produced by the nonlinear advection term and is related to Reynolds stresses:

$$q_{ij} = \rho \overline{u'_i u'_j}$$
(3-10)

27

$$i = j : q_{11}, q_{22}, q_{33} \qquad Normal\ Stresses$$

$$i \neq j : s_{ij} \qquad Shear\ Stresses$$

The RANS equation can be more simplified by assuming that: 1- In case of turbulent flow, the pressure gradient is the dominant term and much bigger than the gradient in the normal stresses. 2- In case of high Reynolds number, turbulent shear stresses are of higher importance than the viscous shear stresses [30]. One should note that near the wall the second assumption does not hold anymore where viscous stresses are dominant.

Considering the above-mentioned assumptions, the simplified RANS equation can be written as:

$$\rho(\frac{\partial}{\partial t}(\bar{u}_i) + \frac{\partial}{\partial x_j}(\bar{u}_i \bar{u}_j)) = -\frac{\partial \bar{p}}{\partial x_i} + \bar{F}_i - \frac{\partial}{\partial x_j}(s_{ij}) \qquad (3\text{-}11)$$

Presence of Reynolds stresses terms add 3 unknowns, which leaves us with a non-closed set of equations. Turbulence models are required to close this set of equations. Each model has its own advantages and disadvantages and provides some estimation of Reynolds stresses.

3.1.3 Turbulence model

One of the most well-known turbulence models is the semi-empirical K-ε model. Although it has a simple framework in comparison with other turbulence models, due to robustness and reasonable accuracy, it has been used for a wide range of turbulent flow simulations. Turbulence length and time scales in the K-ε method are determined by solving two different sets of equations. One should note that the primary assumptions behind the k-ε model are the facts that the flow is completely turbulent, and also the molecular viscosity is really small. In Fluent there are also two modified versions of K-ε: the realizable k-ε and the RNG k-ε. The following equation gives a relationship between turbulent kinetic energy k, turbulent dissipation rate ε, and turbulent viscosity μ_t:

$$\mu_t = \rho\, C_\mu \frac{k^2}{\varepsilon} \qquad (3\text{-}12)$$

C_μ is a constant.

One of the other well-known turbulence models is the K-ω model. The shear stress transport (SST) K-ω models also includes transport of the turbulent shear stress by turbulent viscosity. This advantage makes K-ω SST mode more reliable in predicting the magnitude and location of flow separation.

These two models will be considered in the calibration simulations and the proper one will be chosen for the rest of this research.

3.1.4 Two-phase flow modelling

The volume of fluid model (VOF) is used to capture the free surface. This method contains three main parts: a method to locate the interface, a method to track the surface through a grid mesh, and special boundary condition for the interface.

For each fluid in the domain, a variable called fraction function (α) is defined for each cell. Fraction function for each phase basically describes what percentage of the cell is occupied by that phase. Sum of fraction functions in each cell should be one. As an example, the fraction function for the fluid phase (blue phase) is shown in the figure below.
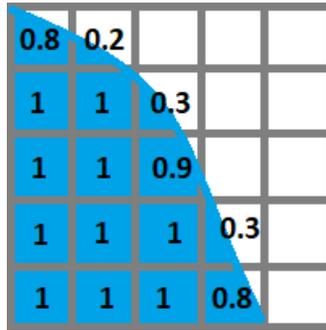
Figure 3- 1 Fraction function for the blue phase in the VOF method.

Based on the α factor, appropriate properties of the fluid are given to each cell. As an example, density follows this equation [31]:

$$\rho = \gamma \rho_i + (1 - \gamma) \rho_j \qquad (3\text{-}13)$$

Conservation of the mass equation for fraction function of each phase should be achieved to be able to track the free surface. For the ith phase, the volume fraction equation takes the form of:

$$\frac{1}{\rho_i}\left[\frac{\partial}{\partial t}(\alpha_i \rho_i) + \nabla(\alpha_i \rho_i u_i) = s_{\alpha_i} + \sum_{j=1}^{n}(\dot{m}_{ij} - \dot{m}_{ji})\right] \qquad (3\text{-}14)$$

Where $\dot{m}_{ij}$ is the mass transfer from phase *i* to phase *j* and $\dot{m}_{ji}$ is the mass transfer from phase *j* to phase *i*. s_{α_i} is source term which is by default zero.

In locations where a cell has only one phase, the standard interpolation method is used as it is the case for one phase flow. In the interface region, the Geometric Reconstruction Scheme which is based on the linear method is used. This linear form of interface is used for calculation of advection of fluid through the cell [32].

Bearing in mind accuracy and computational cost, effects of various modelling parameters were investigated by doing several simulations:

- Mesh sensitivity analysis
- influence of channel wall
- Effects of turbulence models
- Effects of the free surface

3.2 Model setup

One of the first stages which are required for any numerical simulation is a validation of the model. To validate the model, the results of the Fluent model are compared by the results of the experimental research on hydrodynamic forces on bridge deck which was done by the U.S Department of Transportation. Same dimensions of the bridge deck and the experimental hydrodynamic situation is used in a numerical simulation which is described in more details in the following sections.

3.2.1 Overview of the Experimental setup

Forces acting on three different types of bridge deck (Six girder deck, three girder deck, and streamlined deck) were measured in the experimental research which was done by the U.S Department of Transportation. To validate the Fluent model, three girder deck is chosen and dimension of that and its railings are shown in the figures below. The experimental flume was 12.8m long, 0.4 m wide, and 0.5 m high which was made of Plexiglas. The bridge deck was also made of PVC at 1:40 scale.
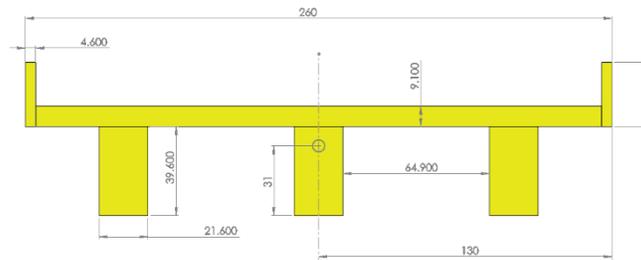
Figure 3- 2 Dimensions of three girder bridge deck.
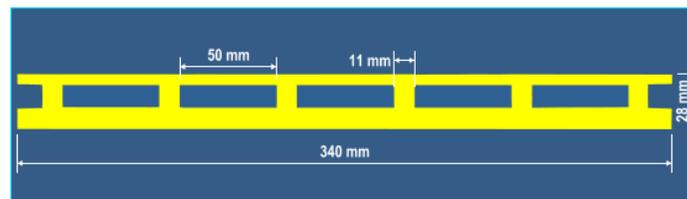
Figure 3- 3 Railings of three-girder bridge deck [13].

3.2.2 Determining the required length of the numerical flume

In order to be computationally more efficient, a smaller length of numerical flume is more favourable. However, length of the flume in front of the bridge should be large enough to allow development and formation of a fully turbulent boundary layer. As a rule of thumb, the required length of the flume for formation and development of boundary layer is at least 20 times of water depth. Since the water depth

was kept 0.25m for all inundation ratios, the required length of the flume in front of the bridge is at least 5 metres. In order to check what length of flume is required for the development of a boundary layer, a simple open channel flow model was made with 7 metres length and 0.25 metre water height. The development of the boundary layer was monitored at each one metre interval from the inlet.
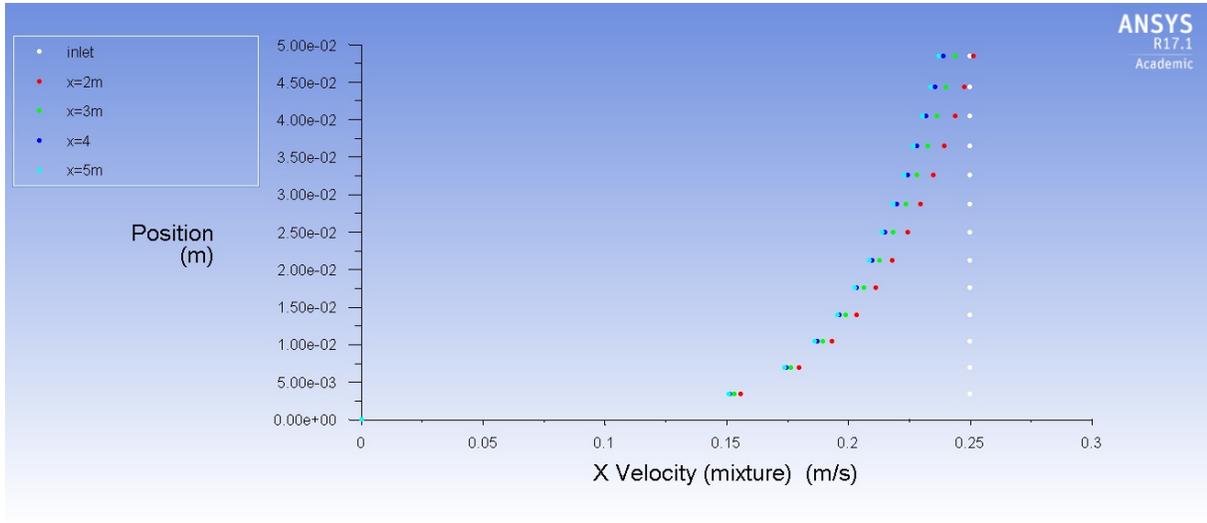
Figure 3- 4. Development of boundary layer at 2,3,4, and 5 metres from the inlet. Uniform inlet velocity at the inlet is shown in white.

As can be seen from the Figure 3- 4, the initial uniform velocity at the inlet starts to deform due to the presence of the bottom channel. The difference between boundary layer at 4 and 5 metres from the inlet is negligible, indicating the boundary layer has reached to almost its final shape and sufficiently has been developed.

The fully developed turbulent boundary layer has a logarithmic profile which can be written based on the Law of the wall as below:

$$\log z = \frac{k}{U_*} U_z + \log z_0 \tag{3-15}$$

K: Von Karman constant (0.4)

Z: distance from the bottom wall (mm), Z_0: roughness length (mm)

U_z: velocity in x-direction (mm/s), U_*: shear velocity (mm/s)

It should be noted that the smallest length scale that exists in flow is known to be the Kolmogorov length scale which forms the viscous sub-layer. The microscale Kolmogorov length scales are several orders of magnitude smaller than one millimetre. As the grid cell size near the wall is approximately 3mm in the above simulation, it can be concluded that the Kolmogorov scales are not resolved in this simple open channel flow simulation.

The semi-logarithmic velocity profile at x = 2, 3, 4, and 5 metres from the inlet are shown in Figure 3- 5. The R-squared and fitted exponential line are also shown in the graph. The gradual development of the boundary layer can be seen by moving along the channel from the inlet towards the outlet. The small

difference between the r-squared value at x = 4 and x = 5 depicts that the boundary layer is sufficiently developed at x = 5m. This development of boundary layer indicates the validity of the open channel model in the simulation.
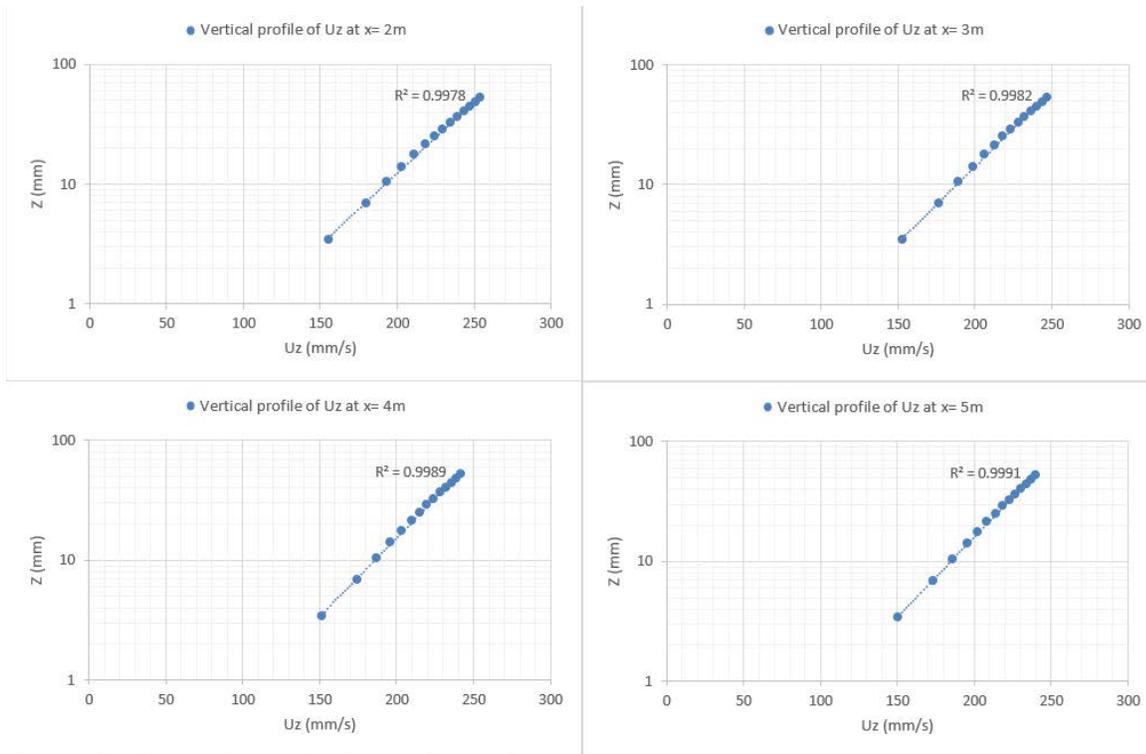
Figure 3- 5. Time-averaged horizontal velocities at x = 2, 3, 4, and 5 metres from the inlet.

3.2.3 Geometry and mesh

The geometry of bridge and numerical flume was first constructed in DesignModeler software and then was exported to be used for meshing. The height of numerical flume was chosen the same as the experimental one (0.5m). The length of the flume in front of the bridge was 5m as described in section 3.2.2. The other end side of flume was located 2m away from the leading side of the bridge to allow enough space for formation and transportation of wake zone on the trailing side of the bridge.
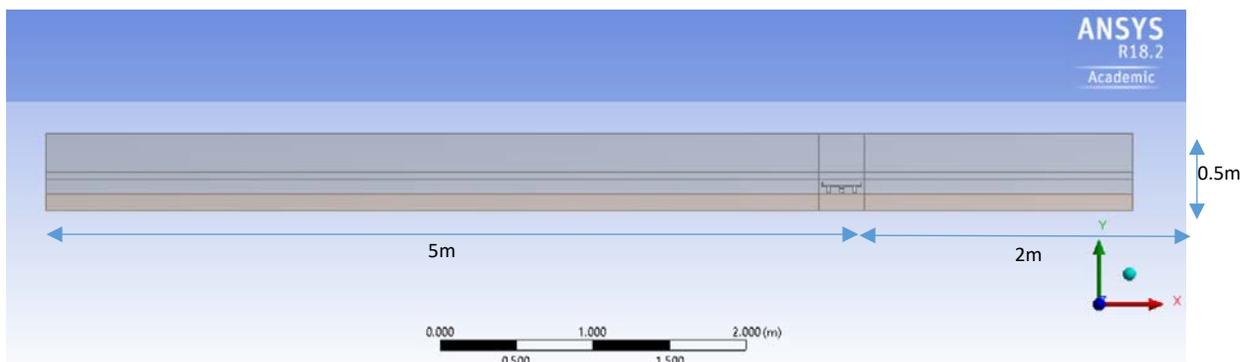
Figure 3- 6. Geometry of Numerical flume.

After constructing the geometry, it was imported to the ANSYS meshing software. The higher number of cells increase both the accuracy of results and the computational cost, hence a reasonable number of mesh that satisfy the accuracy criteria and at the same time does not increase computational time dramatically is favourable. For the first several simulations, different size of uniform mesh in the whole domain was used (ranging from 1cm to 3mm). In the next step, in order to have an efficient distribution of mesh in the domain, a multi-block technique was used in which the domain was divided into several blocks. Depending on the importance of location, the number of mesh and distribution of that was determined.
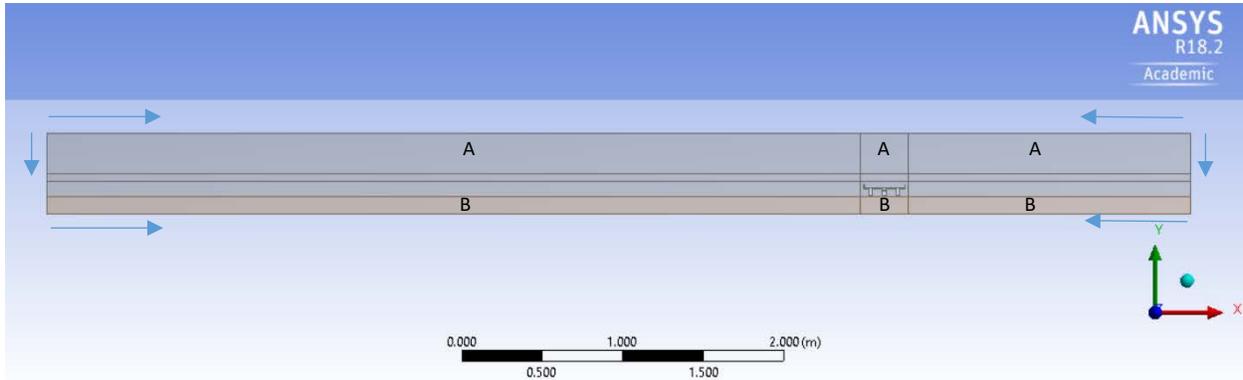
Figure 3- 7. Different mesh block in the domain.

Areas which are shown by A, form the upper 0.25cm of the domain which is occupied by air. Since this area is of lesser importance, it has the bigger size of mesh. On the other hand, the areas near the bridge and areas near the bed (shown by B) are the interest areas and have higher resolution of mesh. The arrows indicating the direction in which the mesh size becomes smaller.
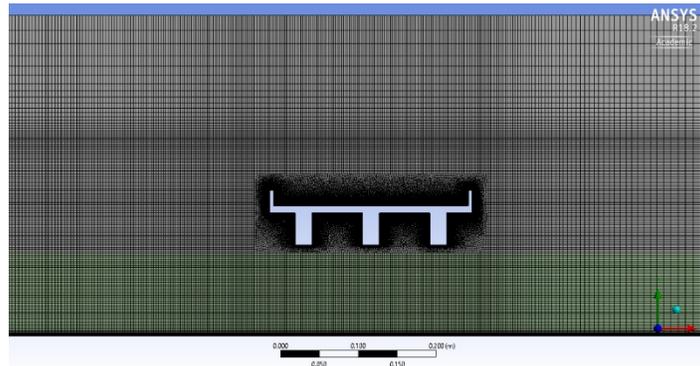
Figure 3- 8. Mesh distribution around the bridge.

A summary of mesh convergence study for h*=0.71 is shown in Table 3- 1. The multiblock mesh with 161471 elements was chosen as an appropriate mesh size since there are no changes in force coefficients for finer mesh size.

Table 3- 1. Summary of mesh convergence study.

Mesh type	Elements	shape	CD	% Difference	CL	% Difference
Uniform mesh	35748		1.83	101 %	-4.0	225 %
	55194		1.64	80 %	-1.89	52%
	141386		1.29	42 %	-1.5	20 %
	394188		0.87	4.6 %	-1.4	11 %
Multi block mesh	79953		0.81	11 %	-1.15	7 %
	161471		0.87	4.6 %	-1.24	0.4 %
	200521		0.87	4.6 %	-1.24	0.4 %
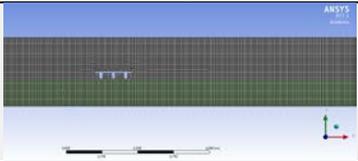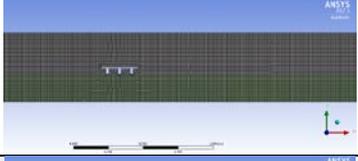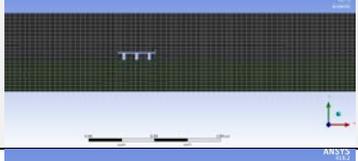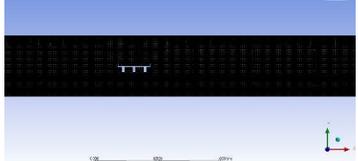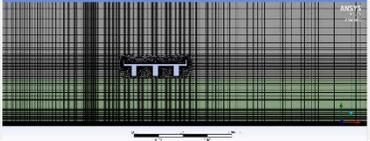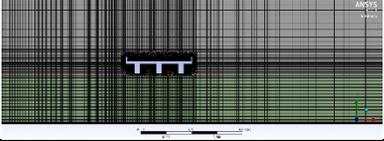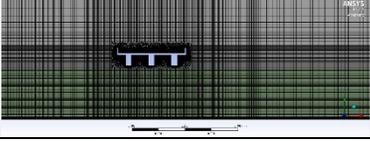
3.2.4 Boundary condition and solution method

The boundary condition of numerical simulation is shown in Figure 3- 9. At inlet constant, a uniform velocity depending on the desired Froude number was defined with the constant water depth of 0.25m. The pressure at the top side of the domain was set at atmospheric pressure. Fluent open channel boundary condition with a constant water depth of 0.25m, which can be defined in Pressure outlet section, was defined at outlet. Bottom bed and bridge were defined as a wall with no-slip condition with specific roughness. Near wall treatment of standard wall function is activated in the turbulence model.
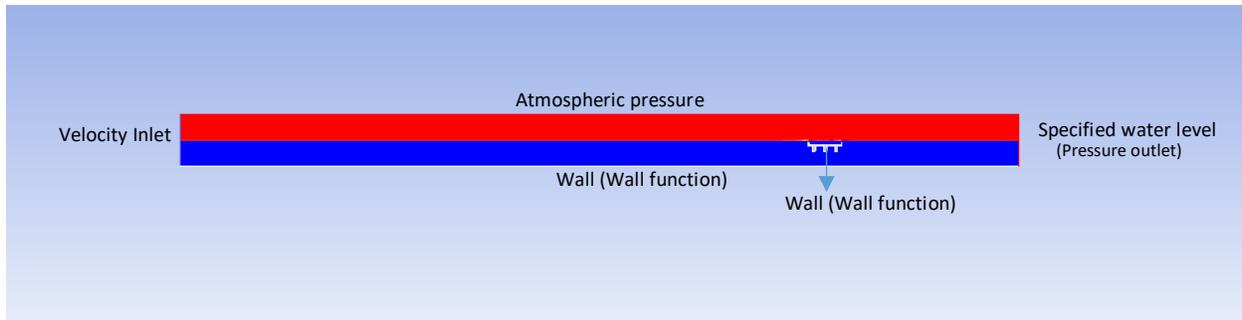
Figure 3- 9. The boundary condition of numerical simulation.

The Volume of Fluid (VOF) method was used for capturing free surface. 20 iterations per time step is applied to reduce the residuals of x and y velocity and continuity equation. The residual for convergence of continuity and turbulence parameter was set to 10^{-6}. SIMPLE scheme was used for coupling pressure-velocity. Second order upwind was used for discretization of momentum, turbulent kinetic energy, and turbulent dissipation rate. In order to get better convergence, under relaxation factor for pressure was 0.3 and other terms were reduced to 0.7. Drag, Lift, and overturning moment were monitored for all scenarios. The solution was initialized from the inlet with the flat open channel initialization method.

3.2.5 Effects of time step on force coefficient

Similar to the mesh size, the smaller time step results in more accurate results. However, a smaller time step means more time for simulation and also it cannot be chosen regardless of mesh size. In order to define the efficient time step there are generally two approaches:

- Defining Courant number: Courant-Friedrichs-Lewy (CFL) is an indispensable part of each numerical simulation that should be satisfied to avoid divergence problems. Smaller Courant number results in smaller time step and vice versa. Although Courant number of 0.5 can be used as a first guess, there is no specific way of determining the appropriate Courant number.

– Applying time step convergence simulation same as mesh convergence study. In this way, based on the ultimate results, an appropriate constant time step is determined. This method was chosen in this study and results of time step convergence study is shown in the figure below (for inundation ratio of 0.7 and Froude number of 0.16). As can be seen, the changes of average drag and lift coefficient in the last 20 seconds of simulation, for time steps of 0.01s and 0.005s is negligible (less than 1 per cent), hence the time step of 0.01s is appropriate for simulations. It should also be noted that for higher velocities, a smaller time step is required. After several simulations for higher velocities, it was found that the time step of 0.005 is appropriate for Froude number of 0.5. To be consistent in the all simulations, the constant time step of 0.005s was chosen for all simulations ranging from Froude number of 0.16 to 0.5.
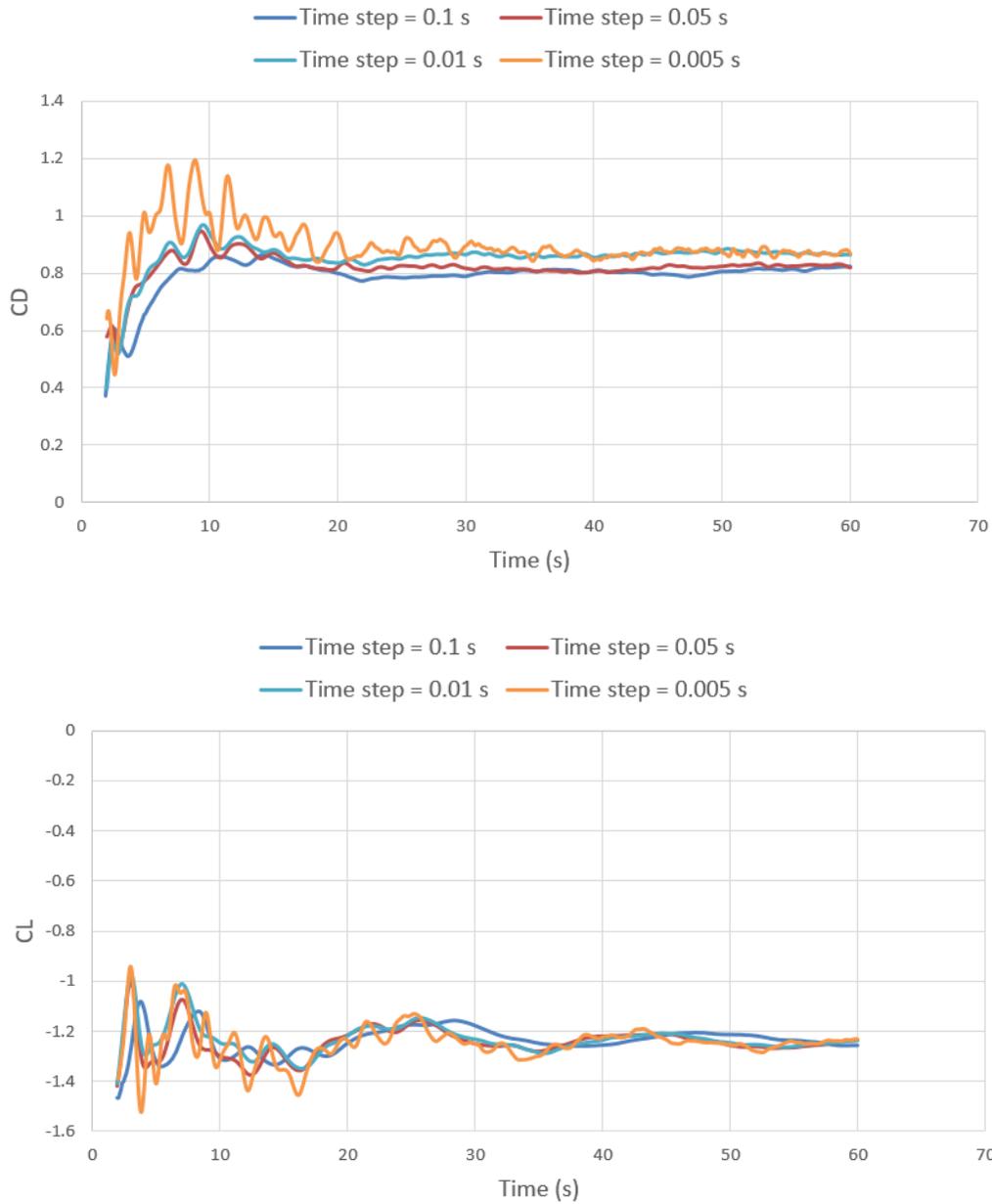
Figure 3- 10. Time step convergence study.

3.2.6 Effects of Turbulence model

Amongst several available turbulence models in Fluent, Re-Normalization Group K-ε model, Realizable k-ε and K-ω SST (Shear Stress Transport) were chosen. The first two models have been successfully used for surface strained flow. They give a reasonable estimation of turbulent viscosity in front of the bridge (stagnation point) [33]. The last turbulence model performs well in situations where separation flows and adverse pressure gradient exist [33].

Drag, lift, and moment coefficient results for these three turbulence models were compared against experimental data in the table below (for inundation ratio of 0.7 and Froude number of 0.16). Results of

K-ε Realizable model and K-ε – RNG model are quite close together. As can be seen, K-ω SST model provides better results for drag and lift coefficient and hence it is chosen for the simulations.

Table 3- 2.Comparison of different turbulence models.

Turbulence model	C_D	% difference	C_L	% difference	C_M	% difference
K-ε - RNG	0.97	6.6	-1.35	8.87	0.0058	95.5
K-ε - Realizable	0.96	5.5	-1.32	6.45	0.0074	94.3
K-ω SST	0.87	4.4	-1.238	0.16	0.0035	97.3

3.2.7 Velocity profile

Since velocity distribution around the bridge has a significant effect on force coefficients, it is essential to have a qualitative (or if possible quantitative) comparison of the velocity profile of numerical simulation with that of experimental. However, there is no precise velocity profile of the experiment. Hence the velocity vector of numerical simulation is analysed based on the expected velocity vector qualitatively.
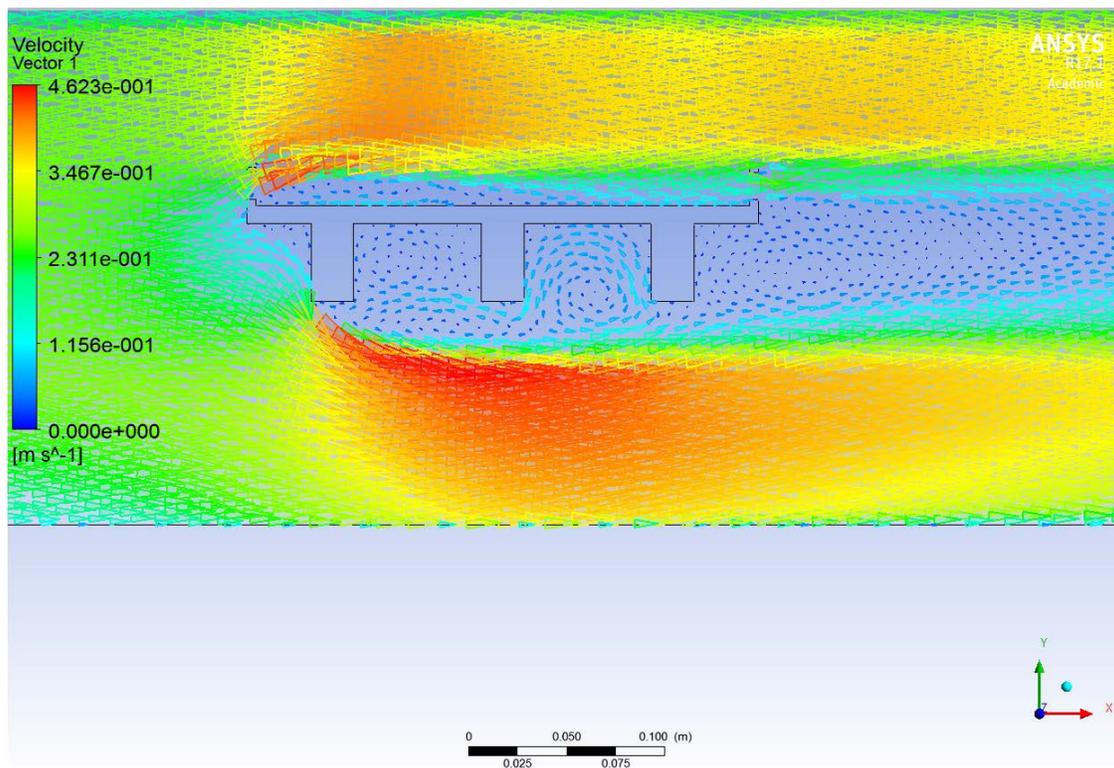
Figure 3- 11. Velocity vector around the bridge deck (Fr=0.16, inundation ratio of 2)

Figure 3- 11 indicates an increase in velocity above and below the deck due to the presence of the deck and hence reduction of the area of the channel. Two vortex zones between girders and the other enormous one downstream of the bridge are depicted. The increase of velocity between railings especially on the leading side of the bridge is shown as expected. The separation of the boundary layer from the bottom of first girder and top of railings are also interesting features in the above velocity vector. In general, it can be concluded that velocity profile shows a strong agreement with expected velocity profile around a bluff body.

3.3 Results of validation of model against experimental data of Federal Highway Administration (FHWA)

Results of numerical simulation for several inundation ratios were compared against experimental data (Hydrodynamic Forces on Inundated Bridge Decks [13]) in terms of drag, lift, and moment coefficient. The experimental data shows the average of several trials for each Froude number and each inundation ratio. In the results, two lines of upper and lower fitting equations are shown which approximately bound the maximum and minimum coefficients in the experimental data. As they form an envelope around the experimental data, they can be named as envelope curves. It should be mentioned that moment coefficient is calculated around the centre of gravity and negative sign of that implies a tendency to overturn.
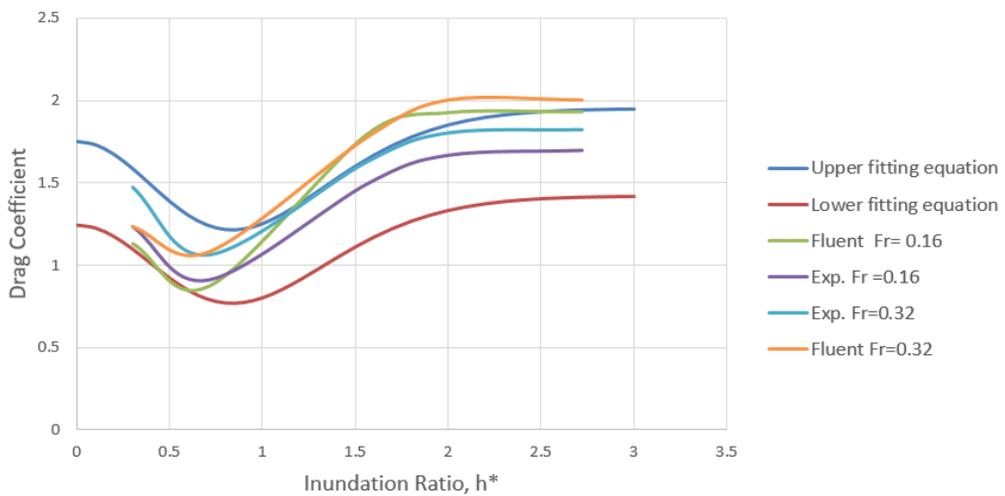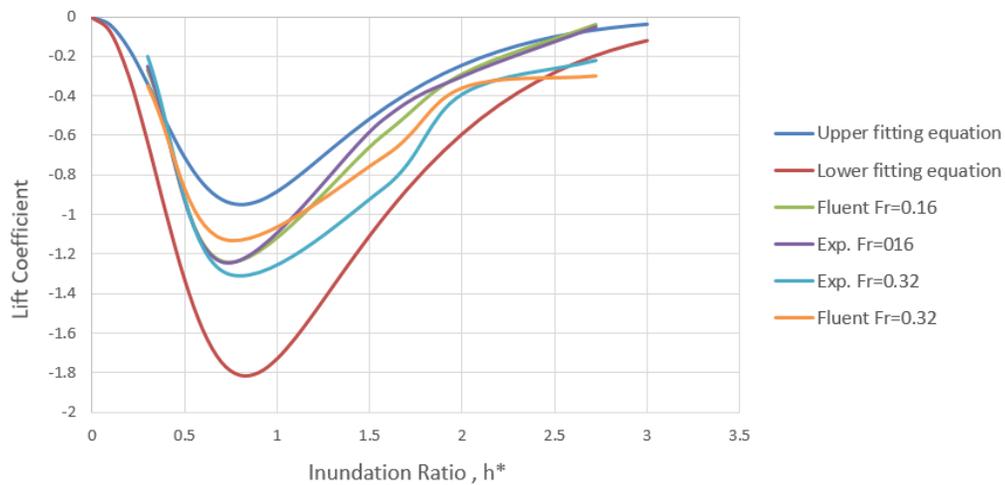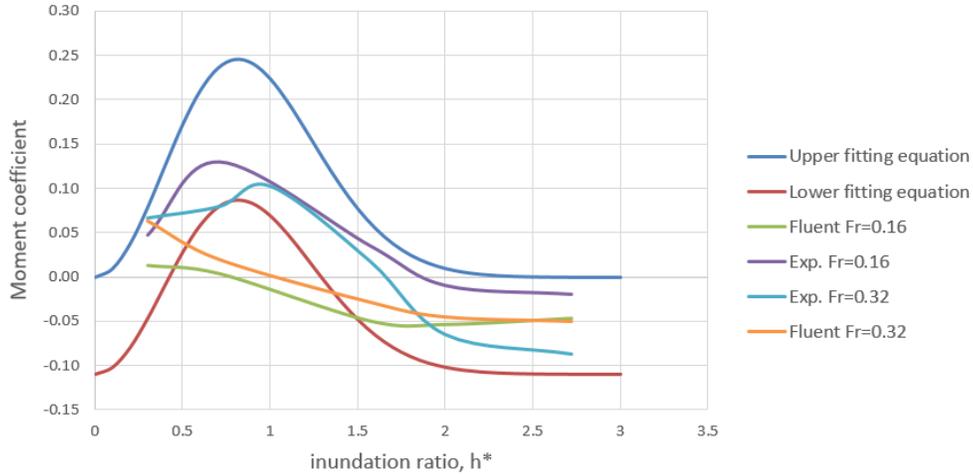
Figure 3- 12. Comparison of results of numerical simulation and experimental data in terms of drag, lift, and moment coefficient.

The results show clear agreement between numerical simulation and experimental data in terms of drag and lift coefficient. However, the moment coefficient of CFD simulation did not closely follow the experimental data. This lack of agreement was also mentioned in the CFD simulation (using Fluent and STAR-CD model) by Kornel et al. [13]. Also in the numerical simulation by OpenFOAM model, a significant difference in both the magnitude and the sign of centroidal moment coefficient was reported by Bricker et al. [18].

Comparison of results of CFD simulation with experimental data for Froude number of 0.32 shows the same trend as Froude number of 0.16. However, the difference between the experimental and numerical value of the lift coefficient is more pronounced here.
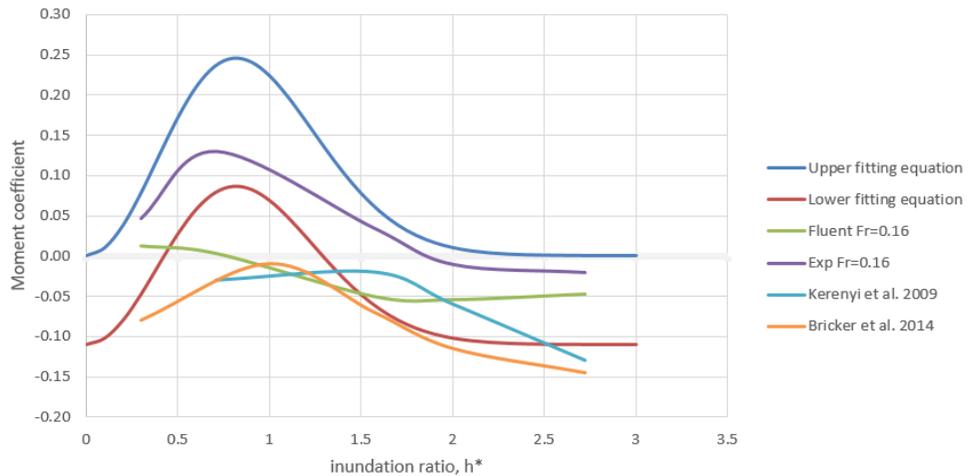
Figure 3- 13. Comparison of results of moment coefficient of this study with other researches.

As can be seen from Figure 3- 13, although none of the CFD simulations follow exactly the experimental data for moment coefficient, results of this study capture a better trend of changes in the moment coefficient shown in the experimental data.

3.4 Results of validation of model against experimental data of rectangular cylinder

In the previous section, a satisfactory agreement between numerical results and experimental data of FHWA, in terms of force coefficients, was established. However, in terms of moment coefficient, some doubts remained. To improve the confidence in the final results, simple geometry (a rectangular cylinder) is used to validate the numerical model. The experimental data for this second validation was extracted from the research of Malavasi and Guadagnini (2003). The experimental conditions are as follows:

Rectangular cylinder (length = 0.18 m, thickness= 0.06 m, width equal to the width of the flume = 0.5 m) was placed in a 5-m long flume. The distance from the underside of the cylinder to the flume bottom (h_b) is kept as 0.14m. The cylinder is fixed at a distance of 3.35 m from the inlet. The upstream water depth (h_u) is within the range of 0.17 to 0.4 m which is equivalent to the inundation ratio of 0.5 to 4.3. The Froude number is in the range of 0.1 to 0.15.
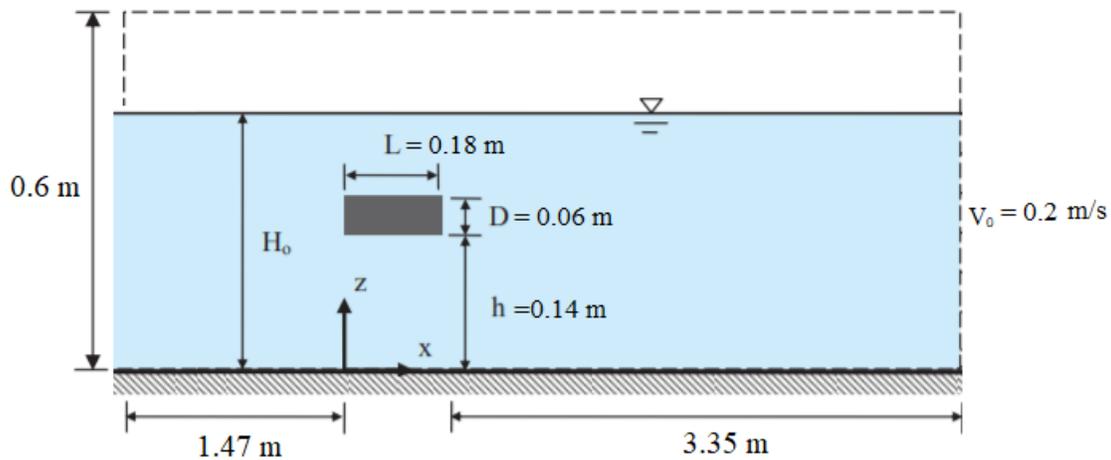
Figure 3- 14. Experimental condition of Malavasi and Guadagnini (2003).

The numerical model is built with the same dimension, water depth, and velocity as the experimental condition. The other numerical parameters such as time step, boundary condition, mesh size, and turbulence model are kept equivalent to the first validation model. The simulation is run for 60 seconds with the last 20 seconds of average drag, lift, and moment being monitored during the simulation. The comparison of numerical and experimental results in terms of force and centroidal moment coefficients are shown in Figure 3- 15. From this figure it can be seen that the drag, lift, and moment coefficients strongly agree with the experimental data, proving the capability of the model at calculating forces on submerged objects. Further explanation of the dependence of hydrodynamic forces on the hydraulic situation and bridge configuration is given in the next chapter.
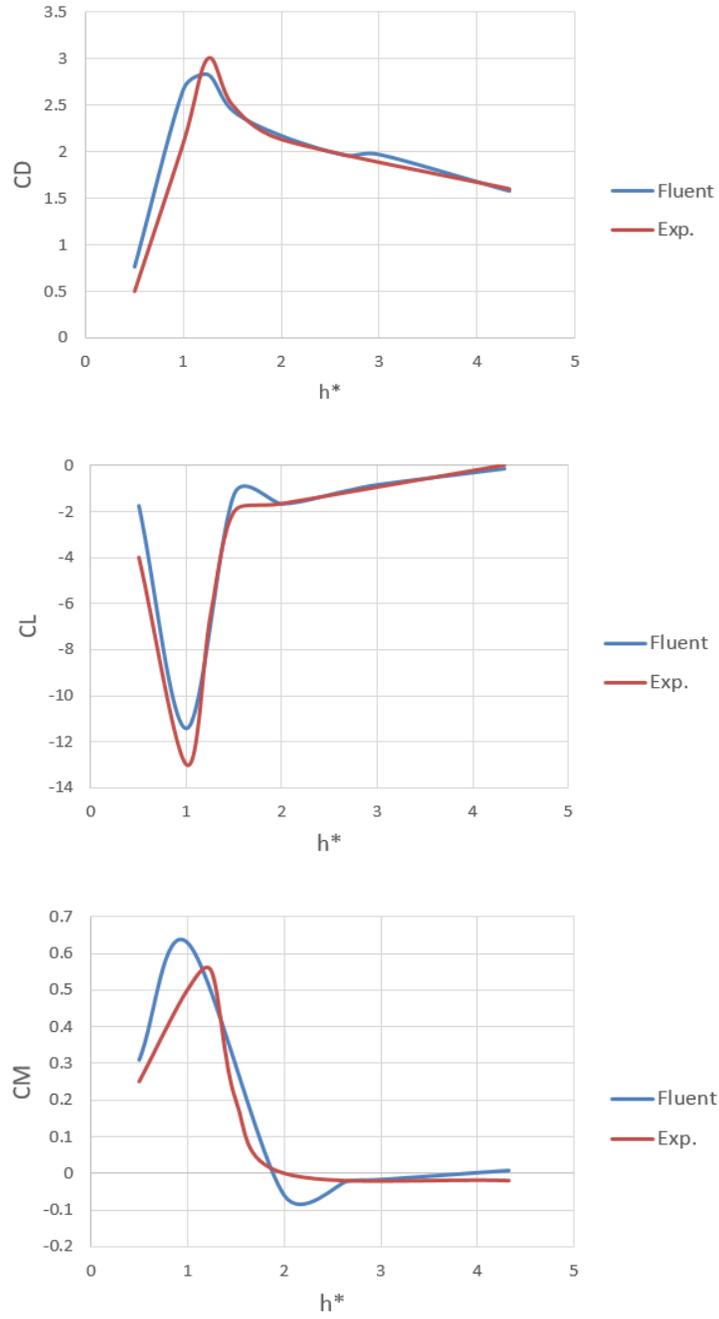
Figure 3- 15. Comparison of numerical and experimental results in terms of force and moment coefficients on the submerged rectangular cylinder.

4 Results and Analysis

The main findings of this research are presented in this chapter. The first three parts of this chapter aim to answer the main research question of this thesis which is "What are the critical hydrodynamic situations that lead to the failure of river bridges?" The dependence of hydrodynamic forces with submergence ratio (h*), flood velocity (V), and blockage ratio (Br) is investigated (look at Figure 2- 7 for schematic diagram). Moreover, the effect of the presence of the bridge close to the free surface or bottom channel is discussed. The next two parts discuss the role of super elevation (angle of attack) and bridge aspect ratio in the failure of bridge decks. The efficiency of possible countermeasures is discussed in section 4.6. The effects of scaling on hydrodynamic forces and centroidal moment are discussed in the last part of this chapter.

4.1 Hydrodynamic forces on bridge deck

Discussion and results of the hydrodynamic forces on the bridge deck are presented in this chapter. As it was noted in the previous chapter, results of this numerical model were more reliable in case of simple geometry such as a rectangular cylinder, hence the bridge deck was modelled as a rectangular cylinder. This uniform geometry also provides a chance to better understanding the mechanisms governing the interaction of flood with bluff bodies such as bridge deck.

In order to fully investigate the hydrodynamic loadings on the bridge deck, three sets of experiments were performed as shown in Figure 4- 1. The dimensions of the rectangular cylinder are shown in the first picture of Figure 4- 1.
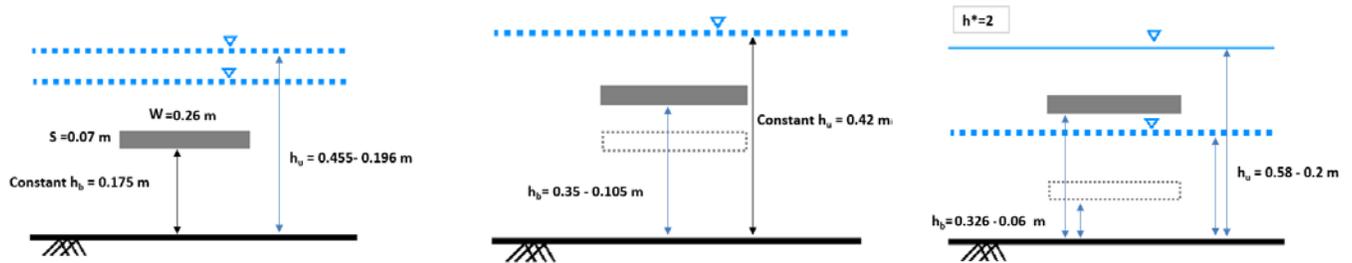
Figure 4- 1 Bridge and water depth configurations. Scenario1 (left picture): fixed position of bridge h_b = 0.175m. Scenario 2 (middle picture): Constant water depth h_u = 0.42 m. Scenario3 (right picture): Constant inundation ratio h^*=2.

4.1.1 Effect of inundation ratio on hydrodynamic loadings

In the first set of experiments, in order to analyse the effect of inundation ratio on hydrodynamic forces on the bridge deck, the distance of channel floor to the bottom of cylinder was kept at 0.175 m, while the water level was in the range of 0.196 to 0.455 m. The inundation ratio is in the range of h^* = 0.3 to 4. In order to have subcritical flow in the upstream, flood velocity was in the ranges from 0.2 to 0.8 m/s which is equivalent to Froude number of 0.09 to 0.58. This configuration of water depth, velocity, and bridge thickness keeps the upstream flow subcritical, resulting in a wide range of deck Froude number (F_{rd}, Froude number based on the thickness of the deck, *s*) from subcritical, 0.24, to almost critical flow, 0.97.

The simulation is conducted for 60 seconds, with the average drag, lift, and overturning being recorded in the last 20 seconds. Unlike the validation section where centroid moment was calculated, as the overall stability of bridge deck is important for this chapter, the overturning moment acting about the bottom downstream corner of the cylinder was also considered in this section. More negative moment implies a higher tendency to overturn.

4.1.1.1 Effect of inundation ratio on drag coefficient

The dependence of drag and lift coefficient on inundation ratio (h*) and velocity are shown in Figure 4- 2 and Figure 4- 6 respectively. These two figures clearly highlight the fact that force coefficients are dependent on the deck Froude number and there are two distinct trends for V< 0.5 m/s and V > 0.5 m/s. For deck Froude number of less than or equal to 0.6, the drag coefficient increases with increasing h* up

to h* around 1 - 1.2 depending on the incoming velocity, after which it starts to drop. The increasing slope of the graph indicates an increase in inundation of the frontal area of the cylinder. The decreasing slope indicates a reduction in the blockage ratio (blockage ratio, Br, is defined as the frontal area of the cylinder divided by upstream water depth). However, it is not straightforward to distinguish between the effect of blockage ratio and submergence ratio by considering this configuration, i.e. fixed bridge and variable water depth. As the submergence ratio increases, h*≥3.5, drag coefficient approaches the constant value of about 1.6. This drag coefficient is close to the experimental result of Yu and Kareem (1996), CD= 1.56, which was done for an unbounded flow.
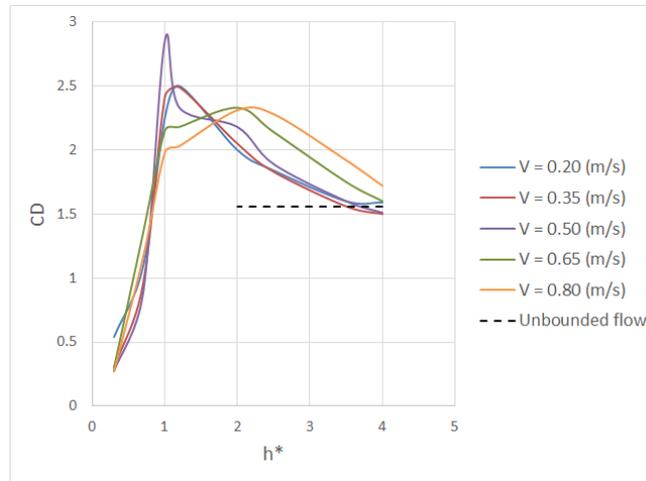
Figure 4- 2 Drag coefficient versus inundation ratio for different upstream velocities.

Another point which should be discussed in Figure 4- 2 is the peak drag that occurs for deck Froude number of 0.6 (velocity 0.5 m/s) at h*=1. The water surface elevation for h*=1 and velocities of 0.2 and 0.5 m/s is shown in Figure 4- 3. When the velocity is 0.2 m/s, the effect of blockage due to the bridge is small and water is able to pass beneath the bridge by acceleration. When the velocity is big enough, 0.5 m/s, water accumulates in front of the bridge and starts to overtop the bridge. This accumulation of water in front of the bridge is equivalent to drop of the free surface behind the bridge which causes a significant pressure difference between leading and trailing edge of the cylinder and hence an increase in drag coefficient [34]. This point clearly shows that the drag coefficient is dependent on both the h* and Froude number. For inundation ratio of higher than 2, higher deck Froude number results in higher C_D.
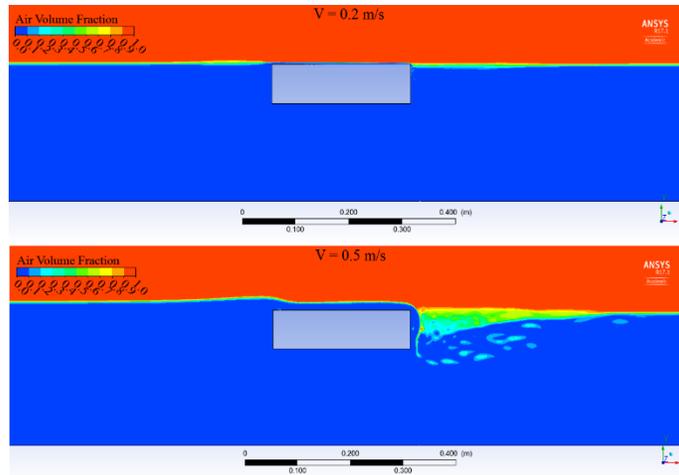
Figure 4- 3 Volume fraction of water and air for inundation ratio of 1 and velocity of 0.2 – 0.5 m/s.

When the velocity is larger than 0.5 m/s, the maximum peak of C_D occurs at h* of around 2. This shift of maximum C_D for higher inundation ratios can be attributed to the occurrence of hydraulic jump just downstream of the bridge, Figure 4- 4. In this case, Froude number based on the water depth above the deck becomes supercritical (Fr>1) and the hydraulic jump occurs just downstream of the deck. Higher flow velocity in hydraulic jump results in a higher pressure drop and hence a higher pressure difference between trailing and leading edge of the bridge i.e., higher C_D, Figure 4- 5.
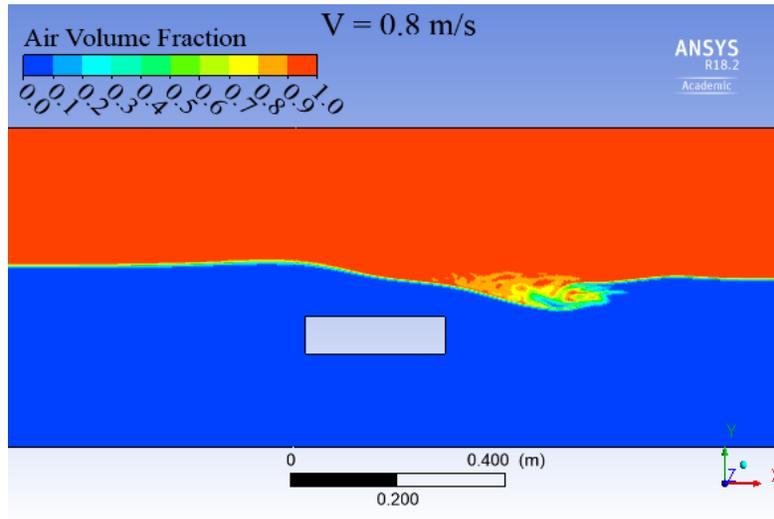
Figure 4- 4 Hydraulic jump downstream of the bridge, h=2.*

In order to show pressure distribution around the cylinder in the non-dimensional form, pressure coefficient can be defined as follows:

$$C_p = \frac{p - p_0}{\frac{1}{2}\rho V_0^2}$$

(4-1)

P_0: hydrostatic pressure, P: total pressure, ρ: water density, V_0: upstream velocity.

46
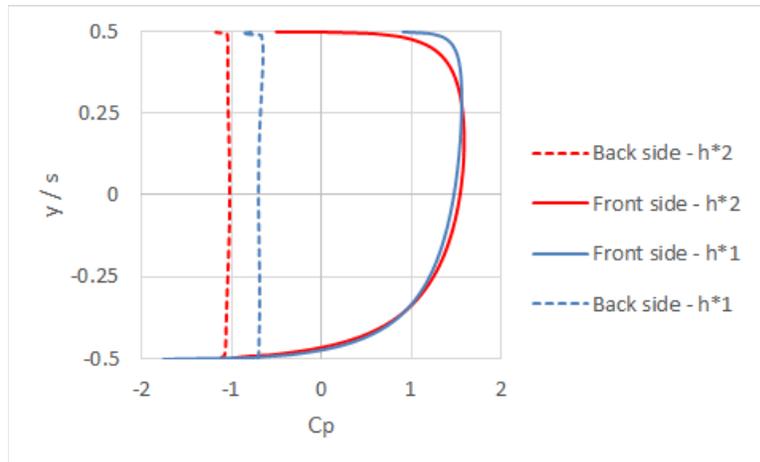
Figure 4- 5. Pressure coefficient in front and back side of the cylinder, V=0.80 m/s.

4.1.1.2 Effect of inundation ratio on lift coefficient

Dependence of lift coefficient with h* and velocity is shown in Figure 4- 6. When $0 \leq h^* \leq 1$, there is no water flow on the upper part of the cylinder and flow acceleration only occurs at the bottom of the cylinder which results in negative pressure. More inundation ratio in this range results in more flow acceleration and hence more suction. When water starts to flow over the upper part of the cylinder, pressure distribution becomes more symmetric and hence downward lift decreases. For higher inundation ratios than 3.5, the situation is close to unbounded flow and lift coefficient is close to zero.

Increasing upstream velocity results in more negative lift coefficient for all inundation ratios except h*=1. As was disused for drag coefficient, based on Figure 4- 6, the accumulation of water in front of the bridge (due to blockage effect of the bridge and high flow velocity) and subsequent flow of water on top of the bridge results in more symmetric pressure distribution between bottom and top of the bridge. This is the cause of less negative lift coefficient for higher velocities when inundation ratio is 1.
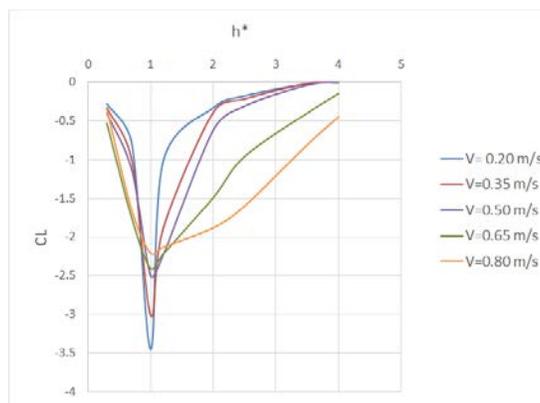
Figure 4- 6. Lift coefficient versus inundation ratio for different upstream velocities.

A higher negative value of lift for higher velocities (except for h*=1), indicates that for the vertical stability of the bridge, smaller velocities are more dangerous. Figure 4- 7 depicts the difference between buoyancy (without flow) and lift force (buoyancy + hydrodynamic lift). It is interesting to note that for the upstream

47

velocity of 0.8 m/s, the downward lift force exceeds the static buoyancy force when 0.5<h*<1.2. In fact, the combination of small velocity with a higher inundation ratio than 2 results in a more critical situation for the vertical stability of the bridge deck.
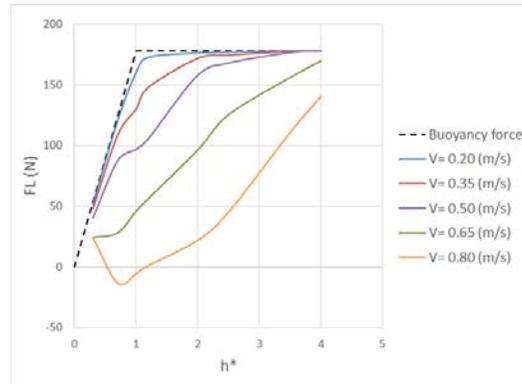
Figure 4- 7. Difference between buoyancy and lift force.

4.1.1.3 Effect of inundation ratio on moment coefficient

Dependence of moment coefficient with h* and velocity is shown in Figure 4- 8. As for drag coefficient, two distinct patterns of changes in centroidal moment exist for V< 0.5 m/s and V > 0.5 m/s. Whilst centroidal moment is positive (anti-clockwise direction) for all range of studied upstream velocities when h* ≤ 1.5, the sign of moment for low velocities (0.2 to 0.35 m/s) becomes negative for h* of around 2. The reason for this different sign of centroidal moment is discussed in the following two paragraphs as well as in the section 4.1.4 of this chapter.
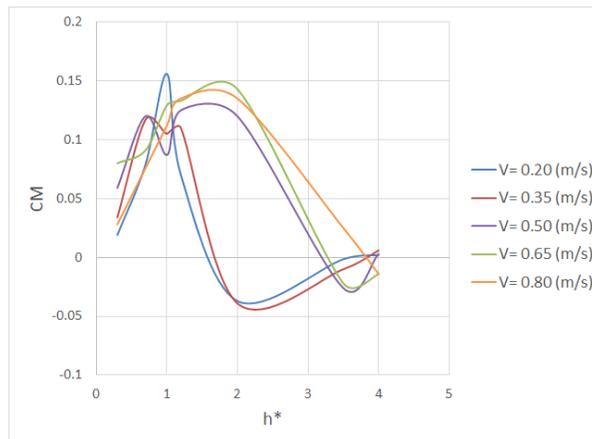
Figure 4- 8. Centroidal moment coefficient versus inundation ratio for different upstream velocities.

In case of V≥ 0.5(m/s), and for higher inundation ratio than 2, the centroidal moment shifts from positive value towards negative value. To analyse the cause of this trend, average velocity profile and pressure around the cylinder are extracted from the results of simulations. Figure 4- 9 depicts the velocity profile and water surface elevation for h*=2, 3.5 and an upstream velocity of 0.65 m/s. The equivalent average pressure coefficient is shown in Figure 4- 10. Left graph in Figure 4- 10 indicates the pressure distribution

in the front and back side of the cylinder. Since pressure is relatively symmetric in the vertical direction, it does not dramatically change the centroidal moment. On the other hand, deformation of water surface and subsequent changes in pressure distribution on the upper side of the cylinder is the main cause of changes in pressure distribution.

When h* is 2, due to the higher blockage effect of the bridge, the deformation of the free surface is higher. This uneven water surface results in lower velocities in the upstream end, and higher velocities in the downstream end of the upper side of the bridge. Both the higher pressure on the upstream end and the higher suction on the downstream end of upper side of the bridge determine the positive value of centroidal moment (anticlockwise direction).

By increasing h*, the effect of blockage of the bridge is smaller, and there is less deformation in the water surface elevation. The water flows at nearly the same speed on the upper side as the lower side and hence the lift effect becomes smaller. Distribution of pressure also in the front and back side of the cylinder is almost symmetric in the vertical direction, left graph in Figure 4- 10. Ultimately, neither drag nor lift significantly influence the centroidal moment which results in a centroidal moment of close to zero for higher inundation ratio than 3.5.
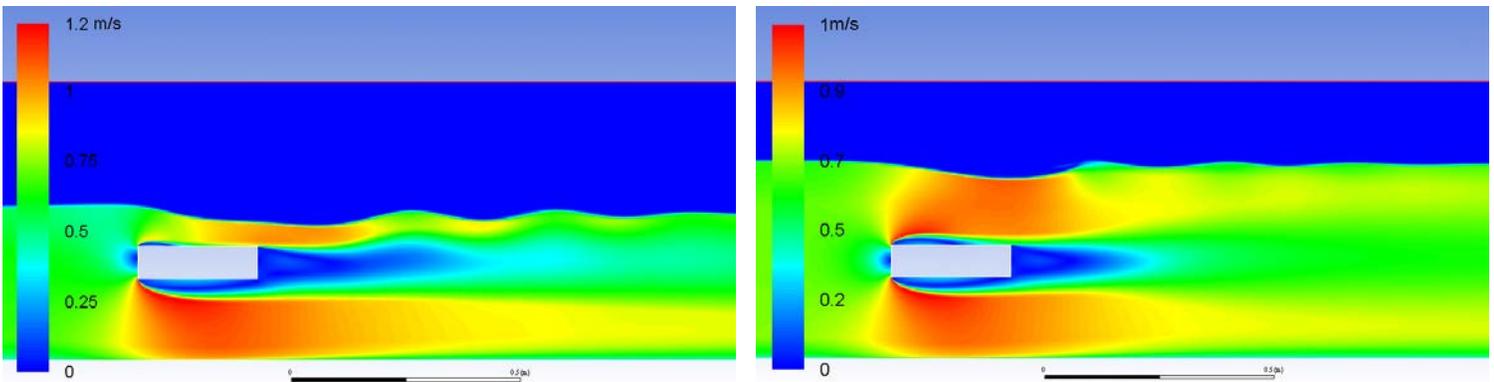
Figure 4- 9. Water profile and average velocity distribution for the upstream velocity of 0.65 m/s, left figure: h=2, right figure h*=3.5.*
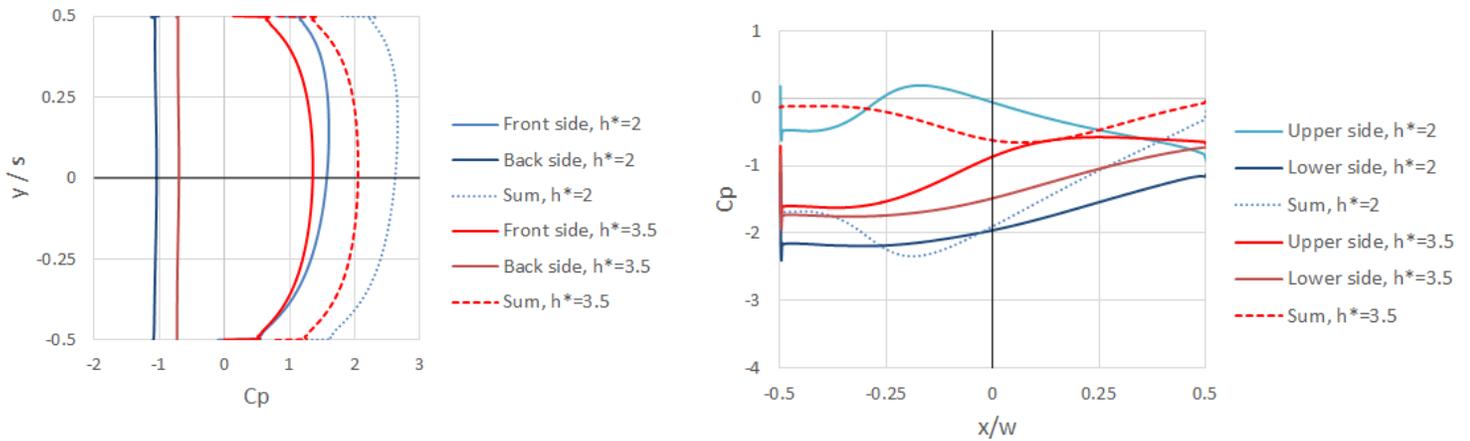
Figure 4- 10. Pressure distribution around the cylinder for h=2, 3.5 and the upstream velocity of 0.65 m/s.*

49

In case of V< 0.5 (m/s), when inundation ratio is larger than 2, the centroidal moment shifts from negative value towards zero value. Average velocity profile and pressure around the cylinder for the upstream velocity of 0.2 m/s and for inundation ratio of 2 and 3.5 are shown in Figure 4- 11 and Figure 4- 12. Unlike the deck Froude number of equal or higher than 0.6, for lower velocities the changes in water level are negligible. However, even in this case, for the lower inundation ratio than around 3, the distribution of velocity on the top of the cylinder is affected by free surface and it is not equal to the velocity on the bottom of the cylinder. In fact, in this case, the separated boundary layer on the top side of leading edge of the cylinder is forced to reattach to the cylinder near the centre line of the cylinder (left graph in Figure 4- 11). This uneven distribution of pressure is the main cause of negative centroidal moment as indicated in the right graph of Figure 4- 12.
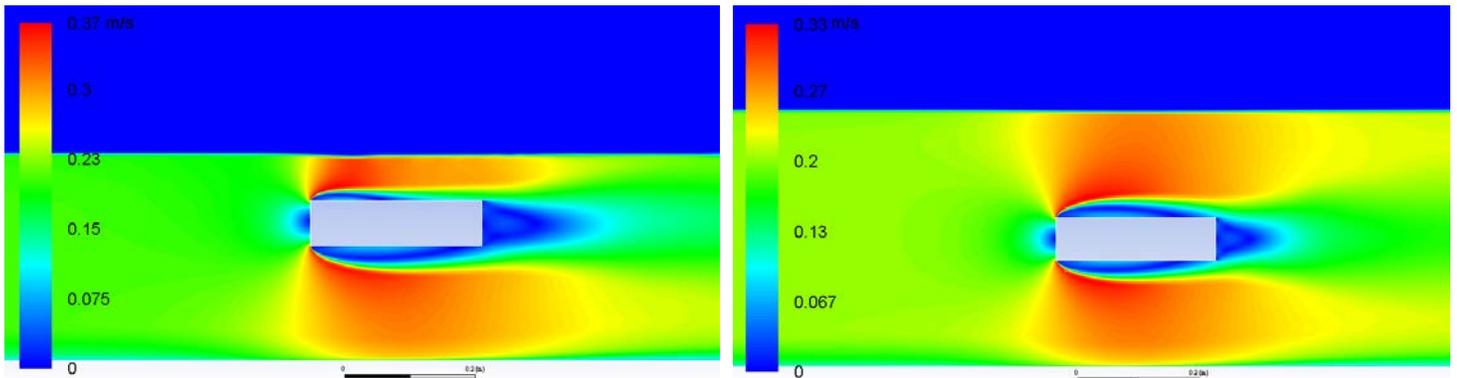
Figure 4- 11. Water profile and average velocity distribution for the upstream velocity of 0.2 m/s, left figure: h*=2, right figure h*=3.5.

For low velocities, V<0.5 (m/s), an increase of inundation ratio results in fairly symmetric pressure distribution around both vertical and horizontal axis passing through the centre of gravity of the cylinder (right graph of Figure 4- 11). This pressure distribution induces no centroidal overturning moment.
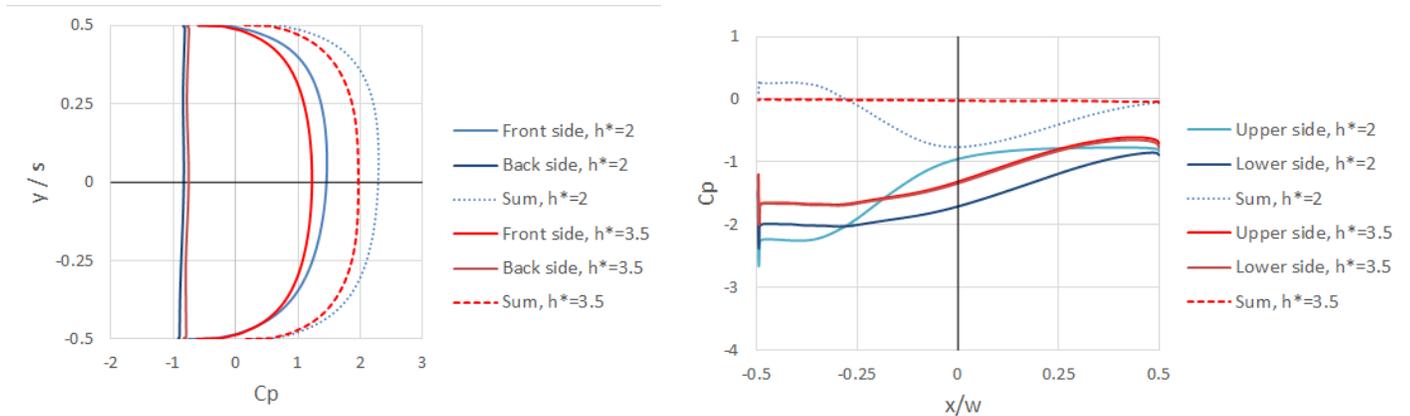
Figure 4- 12. Pressure distribution around the cylinder for h*=2, 3.5 and upstream velocity of 0.2 m/s.

4.1.2 Effect of free surface and channel floor on hydrodynamic loadings

In the previous section, we noticed that blockage ratio and boundaries (free surface and bottom channel) have an influence on force coefficients. In order to investigate the effect of boundaries independently, the water depth is kept constant, 0.42m, whilst the position of the bridge is changed from almost the

bottom of the channel (h_b=0.105m) to the free surface (h_b=0.35m). In this way, blockage ratio will remain constant during all simulations (Br=0.17).

4.1.2.1 Effect of free surface and channel floor on drag coefficient

The effect of boundaries on drag coefficient is less significant as shown in Figure 4- 13. The drag coefficient is less sensitive to the asymmetry in the flow in the vertical direction as it is the case for the lift coefficient. Nevertheless, it can be seen that when deck Froude number is higher than 0.6, the trend of changes in CD is different than that of lower deck Froude number. Moreover, regardless of deck Froude number, by placing the cylinder closer to the bottom of the channel drag coefficient decreases. This trend of reduction of drag by moving the cylinder towards the bottom of the channel is in agreement with the experimental result of Sumer and Fredsoe (1997) for a circular cylinder in an unbounded flow. However, the drag coefficient for the circular cylinder is systematically lower than that of the rectangular cylinder.
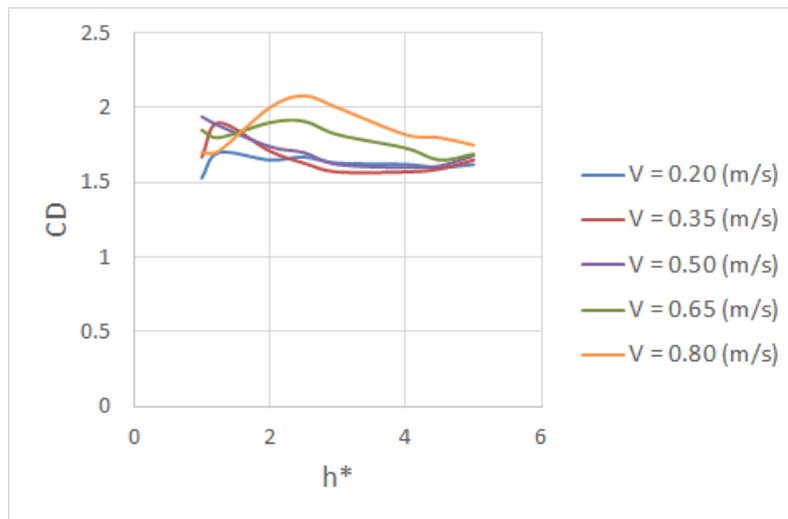
Figure 4- 13. Effect of boundaries (free surface and bottom channel) on lift coefficient for hu/s=6.

4.1.2.2 Effect of free surface and channel floor on lift coefficient

Effects of boundaries on lift coefficient is shown in Figure 4- 14. When the top of the bridge is located at the free surface, flow separation only occurs at the bottom of the bridge which results in a large negative value of lift. As the cylinder approaches the middle of the channel, 3<h*<4, flow pattern on the upper and lower part of the cylinder becomes more symmetric and hence lift approaches zero. Once the cylinder is closer to the bottom of the channel h*>4, the flow pattern becomes asymmetric, and higher suction above the cylinder causes a positive lift coefficient, Figure 4- 15.
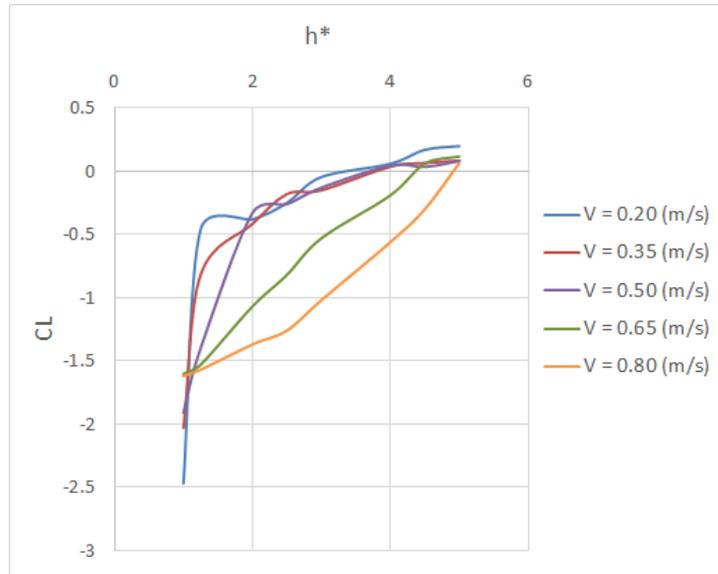
Figure 4- 14. Effect of boundaries (free surface and bottom channel) on lift coefficient for hu/s=6.
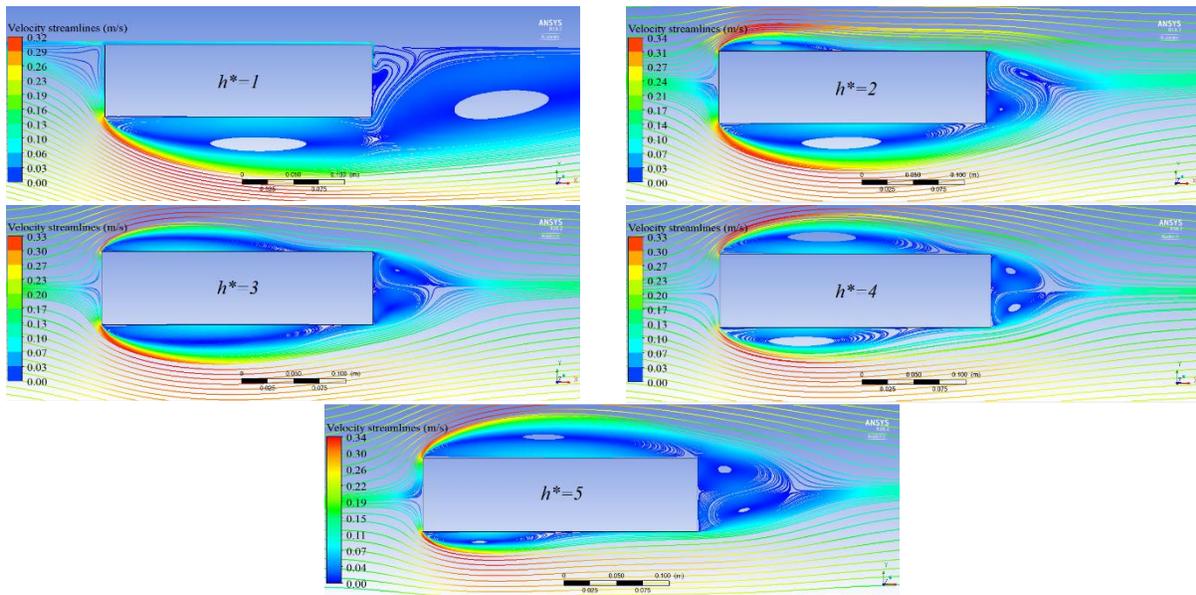
Figure 4- 15. Streamlines of mean velocities around the deck for different inundation ratios.

4.1.2.3 Effect of free surface and channel floor on moment coefficient

Effect of boundaries on moment coefficient is shown in Figure 4- 16. The trend of changes in the centroidal moment follows the same approach as the first scenario cases and can be explained by the same reasoning.
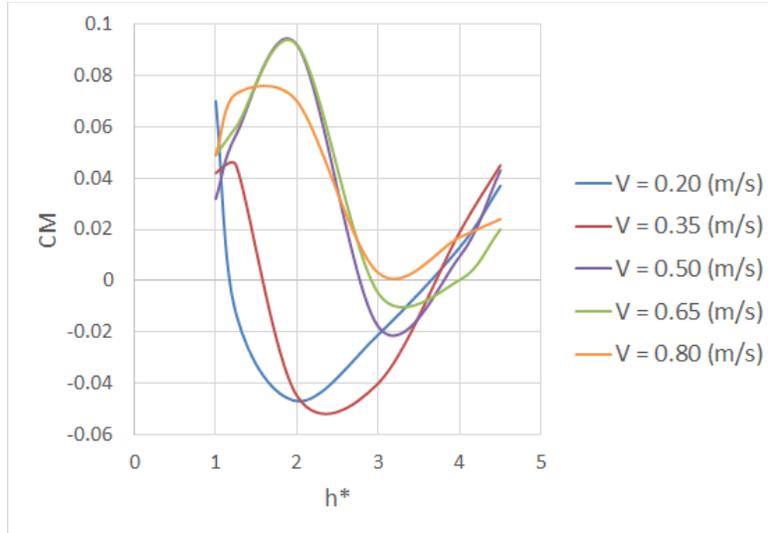
Figure 4- 16. Effect of boundaries (free surface and bottom channel) on centroidal moment coefficient for hu/s=6.

4.1.3 Effect of blockage ratio on hydrodynamic loadings

In this set of simulations, submergence ratio was kept constant by changing both upstream water elevation and distance of the bridge from the channel floor. In this way, the effect of blockage ratio can be investigated independent of submergence ratio.

4.1.3.1 Effect of blockage ratio on drag coefficient

The effect of blockage ratio on the drag coefficient is quite significant as shown in Figure 4- 18. Regardless of deck Froude number, increase in blockage ratio results in an increase in drag coefficient. This rise in drag coefficient is due to both the increase in pressure on the front side and also the increase of negative pressure on the back side of the cylinder, Figure 4- 17. This fact implies that the constant drag coefficient of 2 to 2.2 which was suggested by Hamill (1999) incorrectly neglects the effect of blockage. In fact, for higher blockage ratio than about 0.25 the drag coefficient is higher than 2.2 regardless of the deck Froude number.
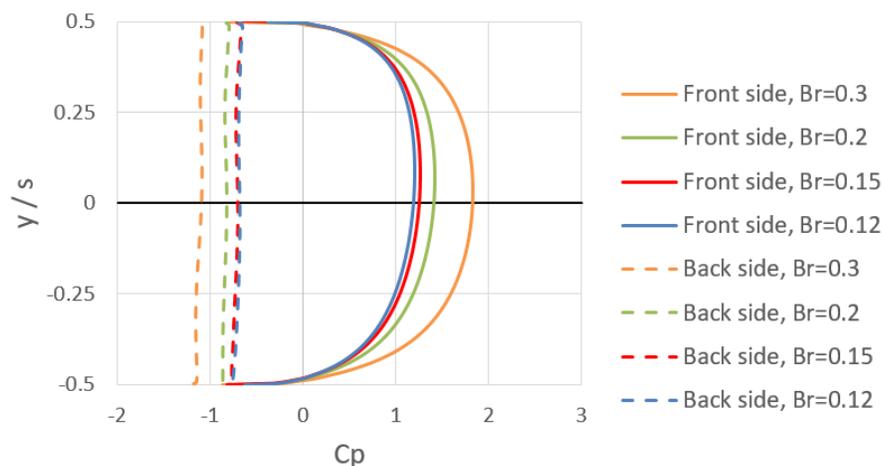
Figure 4- 17. Pressure coefficient in front and back side of the cylinder for different blockage ratio and Frd=0.24.

On the other hand, a decrease in blockage ratio shifts the drag coefficient towards the value of 1.56 for unbounded flow for the rectangular cylinder. For blockage ratio of less than 0.15, the drag coefficient is less dependent on blockage ratio (especially for deck Froude number of equal or less than 0.6). This point is in agreement with the research of West and Alpelt (1982) on a circular cylinder. According to their experimental research on drag forces on a circular cylinder in bounded flow, when blockage ratio is between 0.06 to 0.16, the drag coefficient is close to unbounded flow i.e., with zero blockage ratio.
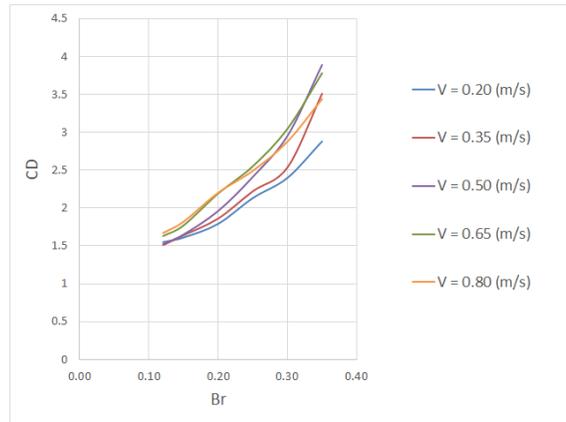
Figure 4- 18 Effect of blockage ratio on drag coefficient for a constant inundation ratio, h*=2.

4.1.3.1.1 Effect of blockage ratio on velocity magnitude

In the previous section, we noticed that an increase in the blockage ratio results in a higher drag coefficient. However, one should note that the drag coefficient was defined based on the undisturbed upstream velocity (V_u). Increase in blockage ratio also results in higher local velocity around the bridge (V_l). If we recalculate drag coefficient based on the higher velocity around the bridge, it can be seen that although there is still an increase in drag coefficient with an increase in blockage ratio, the steep rising slope of drag graph becomes much milder. In fact, a significant part of the increase in drag coefficient by increasing the blockage ratio is due to the increase in the local velocity.
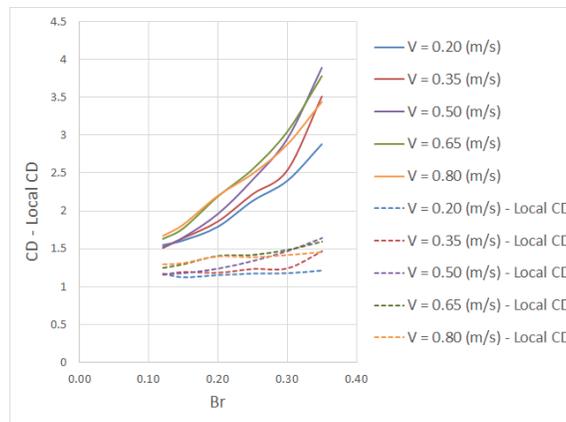
Figure 4- 19. Drag coefficient versus blockage ratio. Based on the two scenarios of undisturbed upstream velocity and local velocity (dotted lines).

These results bring the fundamental question to the general definition of drag coefficient. The drag coefficient in guidelines and design codes is defined based on the upstream velocity. The main reason for considering the upstream velocity is the fact that form drag is mainly due to the pressure difference between front and back side of the deck, hence incident upstream velocity is considered to estimate pressure on the front side. The weak point of this approach is the fact that the effect of an increase in local velocity is incorrectly ignored. Therefore, for calculating the drag coefficient, it is a better approach to consider the local velocity (V_l) instead of upstream velocity (V_u) or incident velocity (V_i). The average local velocity can be estimated by the ratio of discharge to the cross-section area of the river.
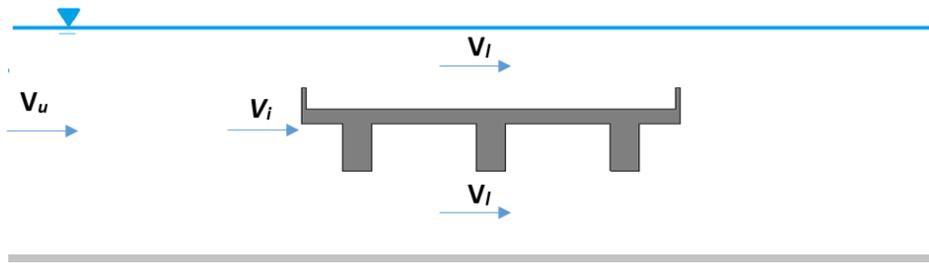
Figure 4- 20. Schematic view of the upstream undisturbed velocity (V_u), the incident velocity (V_i), and the local velocity around the deck (V_l).

4.1.3.2 Effect of blockage ratio on lift coefficient

As far as the effect of blockage ratio on lift coefficient is concerned, results can be divided into two sets of different trends. When deck Froude number is less than 0.6, there is not much change in free surface elevation and flow pattern above and below the bridge is similar as indicated in Figure 4- 21. When deck Froude number is equal to or greater than 0.6, there is an accumulation of water in front of the bridge which causes a sudden drop of free surface at the back of the bridge to satisfy continuity. The drop of water is followed by hydraulic jump on the downstream of the bridge. The uneven distribution of velocities below and above the deck causes the more negative lift in comparison to that for deck Froude number of less than 0.6, Figure 4- 22.
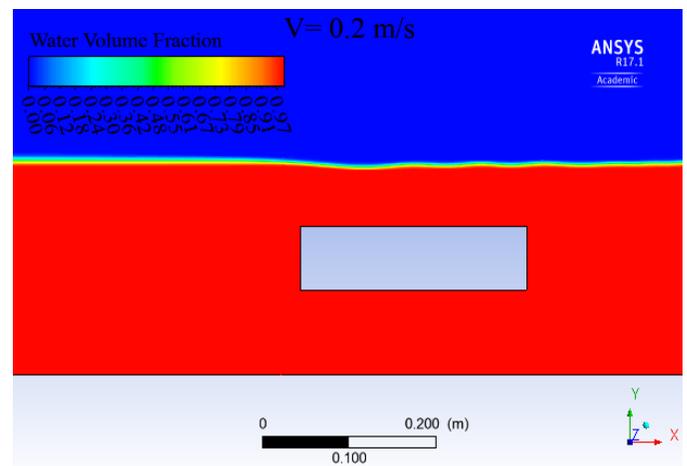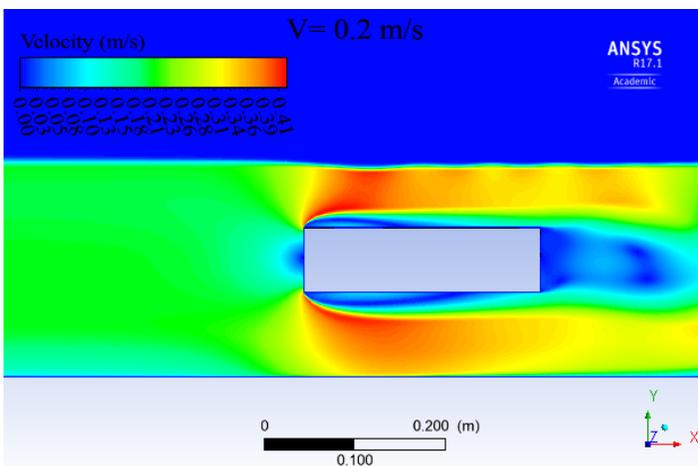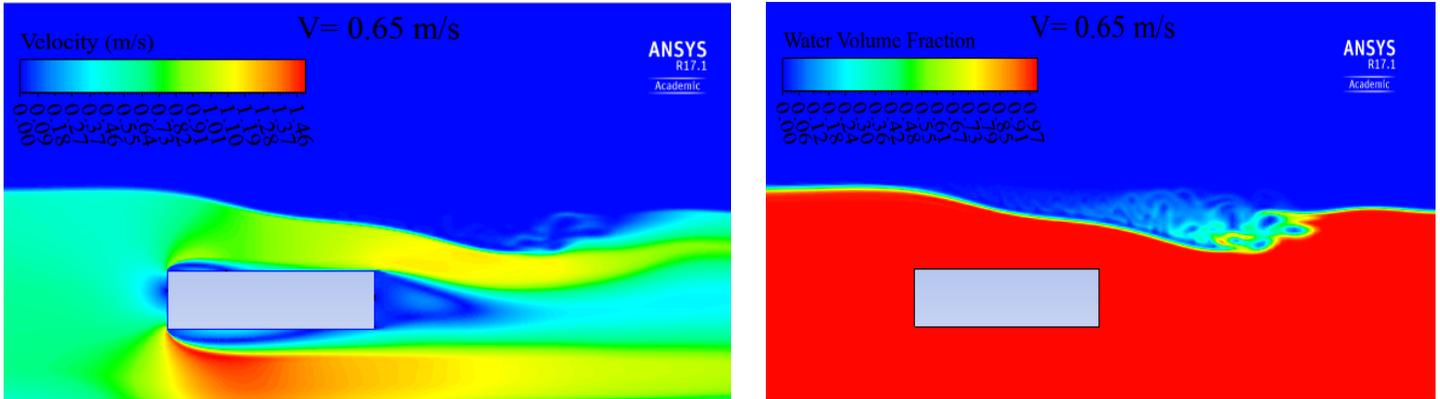
Figure 4- 21 Water profile and velocity distribution for the upstream velocity of 0.2 and 0.65 m/s. In all cases h*=2 and Br=0.30.
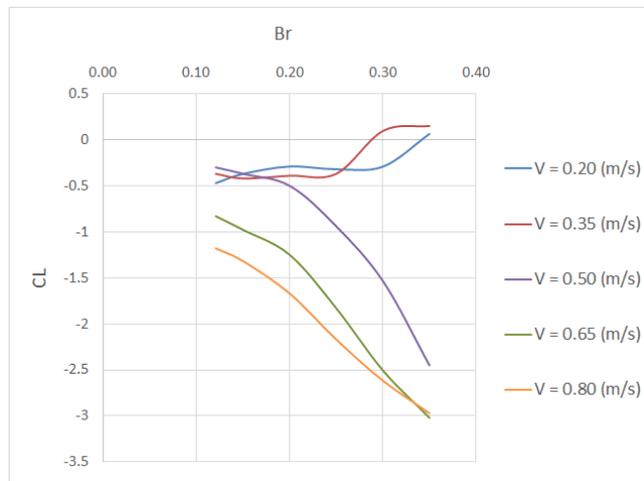

Figure 4- 22 Effect of blockage ratio on the lift coefficient for the constant inundation ratio, h*=2.

4.1.3.3 Effect of blockage ratio on moment coefficient

Effect of blockage ratio on centroidal moment coefficient is shown in Figure 4- 23. As for previous scenarios, the overall changes in CM can be divided into two different trends for velocities equal to or larger than 0.5 m/s and for velocities smaller than 0.5 m/s.
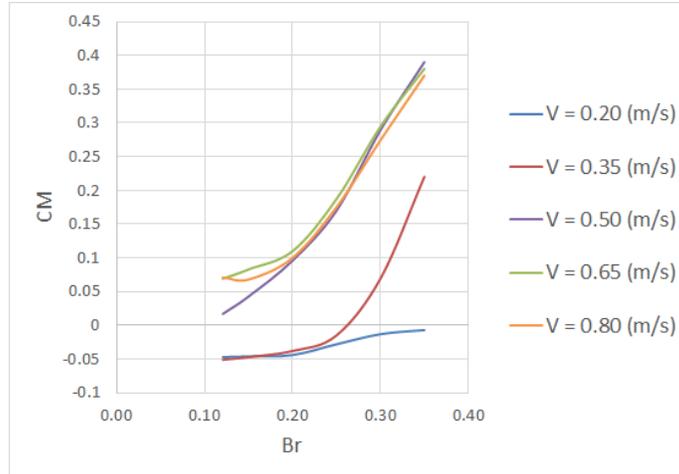
Figure 4- 23. Effect of blockage ratio on centroidal moment coefficient for constant inundation ratio, h*=2.

For all range of studied blockage ratio, CM is positive for V ≥ 0.5 m/s. To analyse the cause of this positive centroidal moment, the pressure coefficient on the upside and downside face of the cylinder for Br=0.2 and V= 0.65 m/s is shown in Figure 4- 24. On the trailing edge of the upper side of the cylinder, due to the deformation of the free surface, the flow starts to accelerate which causes higher negative pressure than that of leading edge, and hence positive moment, Figure 4- 25. The negative pressure on the lower side is larger in comparison to the upper side. The combination of pressure coefficient in the vertical direction is shown by the green dotted line, which leads to an anticlockwise (positive) moment around the centre of the cylinder.
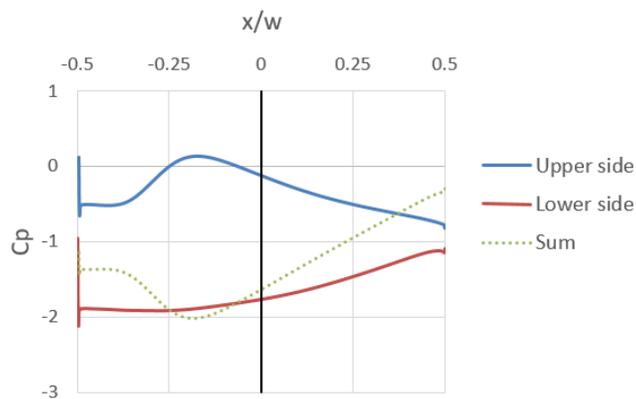
Figure 4- 24. Time-averaged pressure coefficient Cp on upper and lower side of the cylinder for Br= 0.2 and V= 0.65 (m/s).
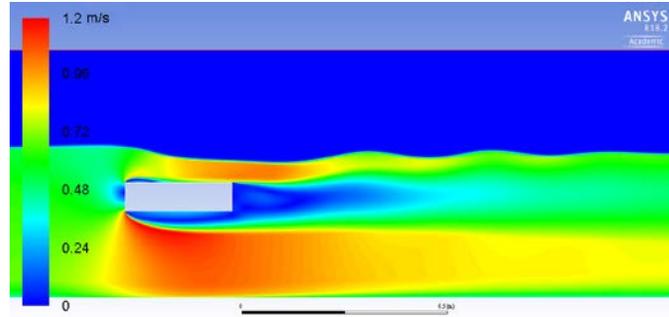
Figure 4- 25. Velocity distribution around cylinder for Br= 0.2 and V= 0.65 (m/s).

Time-averaged pressure coefficient Cp on front and back side of the cylinder for Br= 0.2 and V= 0.65 m/s is shown in Figure 4- 26. The negative pressure in the back side of the cylinder is relatively uniform. However, on the front side, there is a small asymmetry in the vertical direction which causes slightly higher pressure on the upper part of the front side of the cylinder than that of lower side. The sum of this pressure distribution results in a slightly clockwise moment around the centre of the cylinder.

In general, from Figure 4- 24 to Figure 4- 26 it can be concluded that the deformation of free surface causes asymmetric pressure distribution in the upper side of the cylinder, which ultimately results in an anti-clockwise centroidal moment.
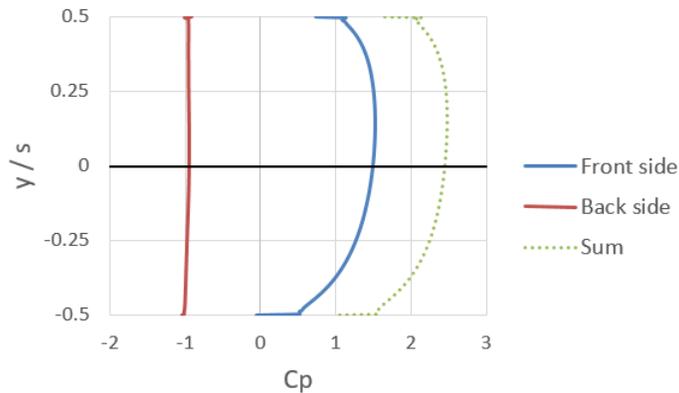
Figure 4- 26. Time-averaged pressure coefficient Cp on front and back side of cylinder for Br= 0.2 and V= 0.65 (m/s).

As was already mentioned, an increase of blockage ratio results in a higher positive centroidal moment. Figure 4- 27, depicts the pressure coefficient for blockage ratio of 0.2 and 0.3 on the upper and lower side of the cylinder when V= 0.65 (m/s). An increase of the blockage ratio does not significantly alter the flow pattern around the cylinder. In fact, higher blockage ratio only results in higher negative pressure on the lower side and an increase of pressure on the upper side of the cylinder, both of which contribute to higher positive overturning moment.
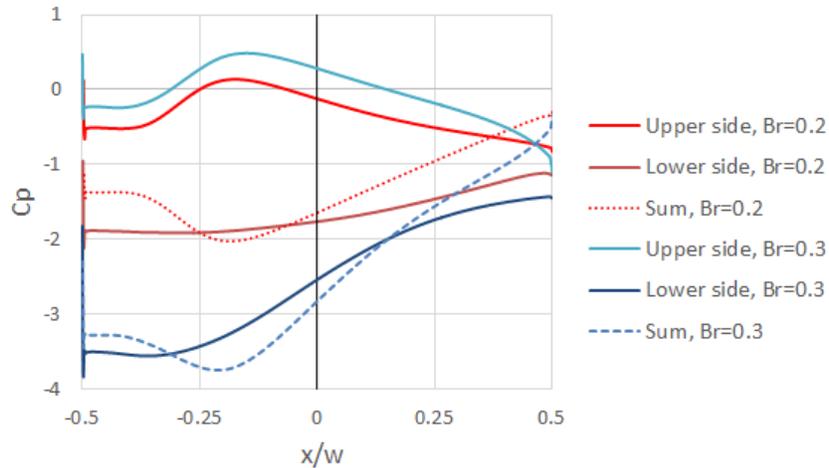
Figure 4- 27. Time-averaged pressure coefficient Cp on upper and lower side of cylinder for Br= 0.2, 0.3 and V= 0.65 (m/s).

As far as the other trend in Figure 4- 23 is concerned, i.e., changes in pressure for velocity smaller than 0.5 m/s, it can be seen that for small blockage ratio, the centroidal moment is negative. As the blockage ratio increases, centroidal moment approaches towards a positive value.

Whilst for these low velocities, the pressure distribution on the front, back, and lower side of the cylinder is not fundamentally different than that of higher velocities, the pressure distribution on the upper part is completely different for these low velocities. In fact, in this case, there are no significant changes in water surface, and velocity distribution above and below the cylinder is more symmetric, Figure 4- 29. The higher velocity and higher suction in the upstream end of the upper side of the cylinder participate in the negative centroidal moment for low velocities.
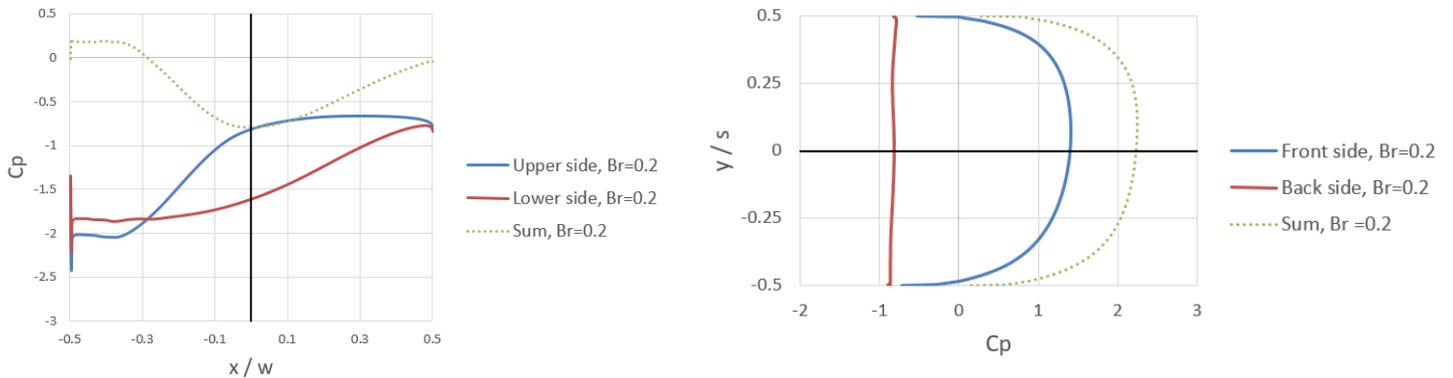

Figure 4- 28. Time-averaged pressure coefficient Cp around all four sides of cylinder for Br= 0.2 and V= 0.20 (m/s).

59
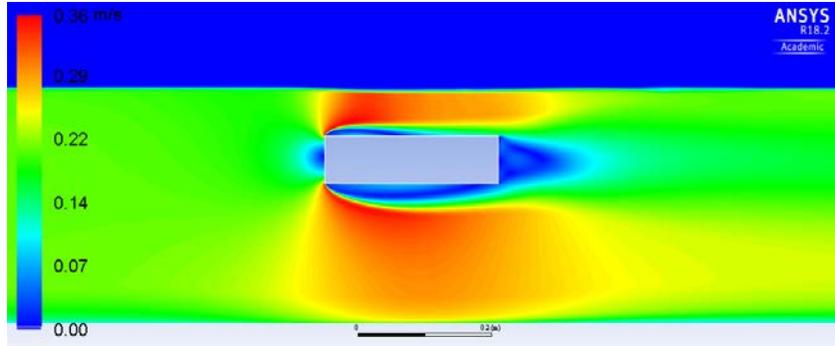
Figure 4- 29. Velocity distribution around cylinder for Br= 0.2 and V= 0.20 (m/s).

4.2 Comparison between box deck and three girder deck

The comparison between hydrodynamic forces on box deck and three girder deck is presented in this section. Results show that the trend of changes in force and moment coefficients for these two cases are quite comparable. However, the magnitude of these coefficients can quite differ depending on the shape of the deck and h*.
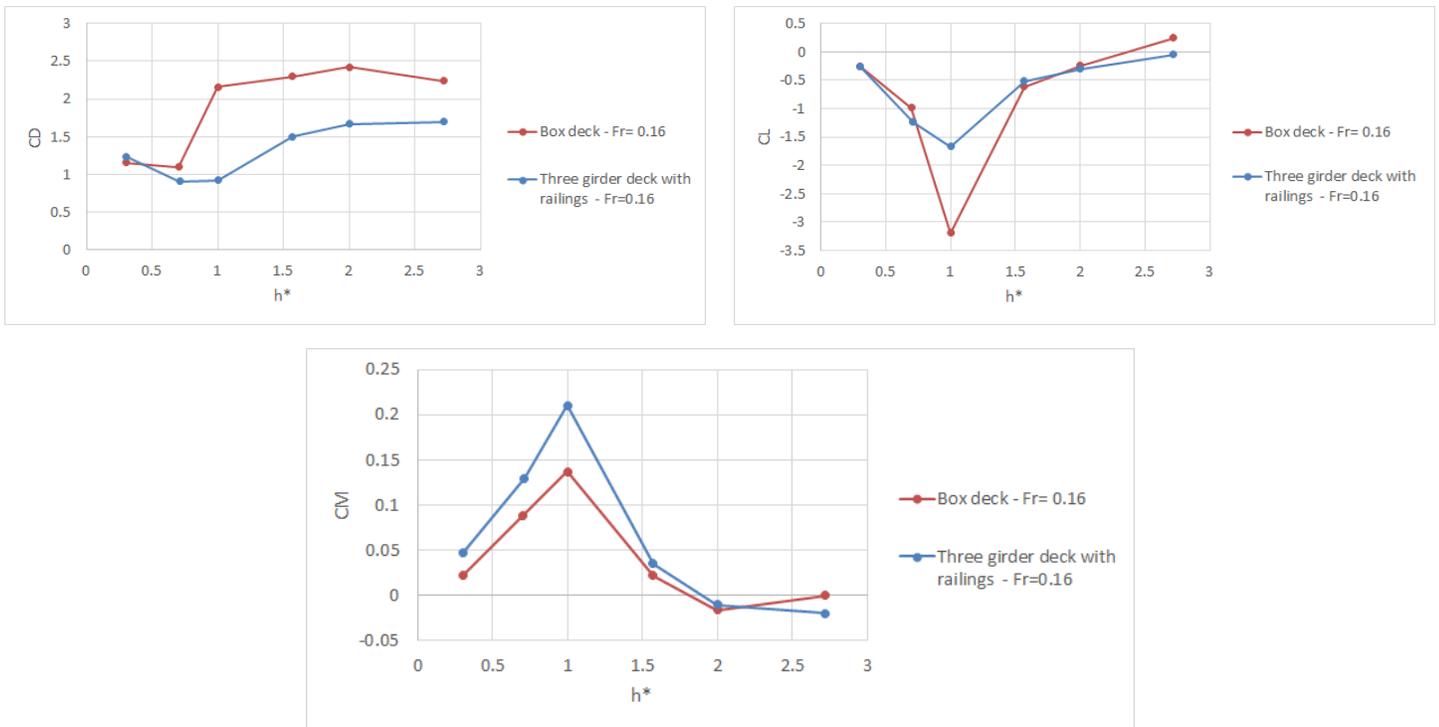
Figure 4- 30 Comparison of hydrodynamic forces on box deck and three girder deck.

As far as the changes in lift coefficient are concerned, it can be seen that results for two decks are relatively close except the inundation ratio of 1. This difference in lift coefficient is because of the presence of the railings in three girder deck which results in a flow of water on top of the deck even for inundation ratio of 1. This flow of water on the girder deck results in less negative lift value and hence significant difference with the box deck.
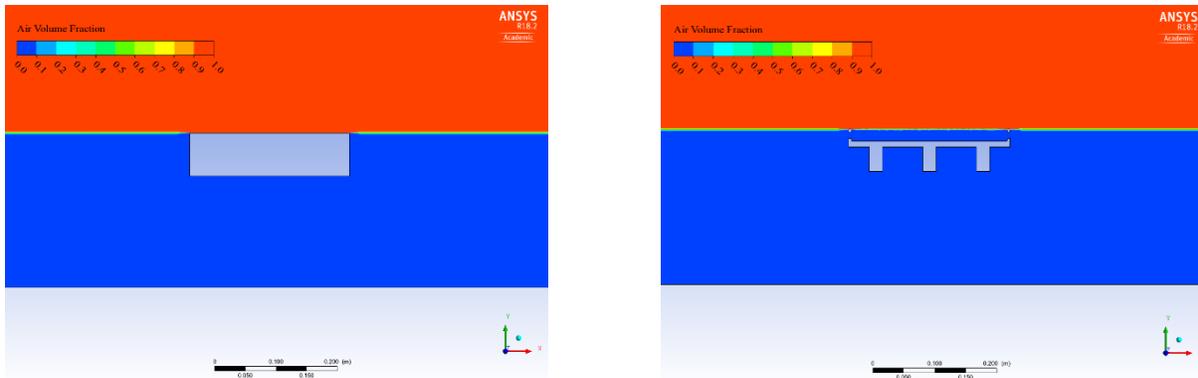
Figure 4- 31. Comparison between water level of box deck and three girder deck with railings, h*=1.

The different shape of the deck for these two cases have enormous influence on flow pattern around the deck, Figure 4- 32. The wake area in the trailing side of the box deck is wider with larger eddies, which results in lower pressure and an increase in drag force. Moreover, the average positive pressure in the leading edge of the girder deck is smaller due to the presence of small recirculation zone in front of the upper part of the first girder, Figure 4- 33. However, it should be noted that the frontal area of these two cases are not the same (Three girder has smaller frontal area due to the presence of the railings) which brings some difficulties in the comparison of these two cases.
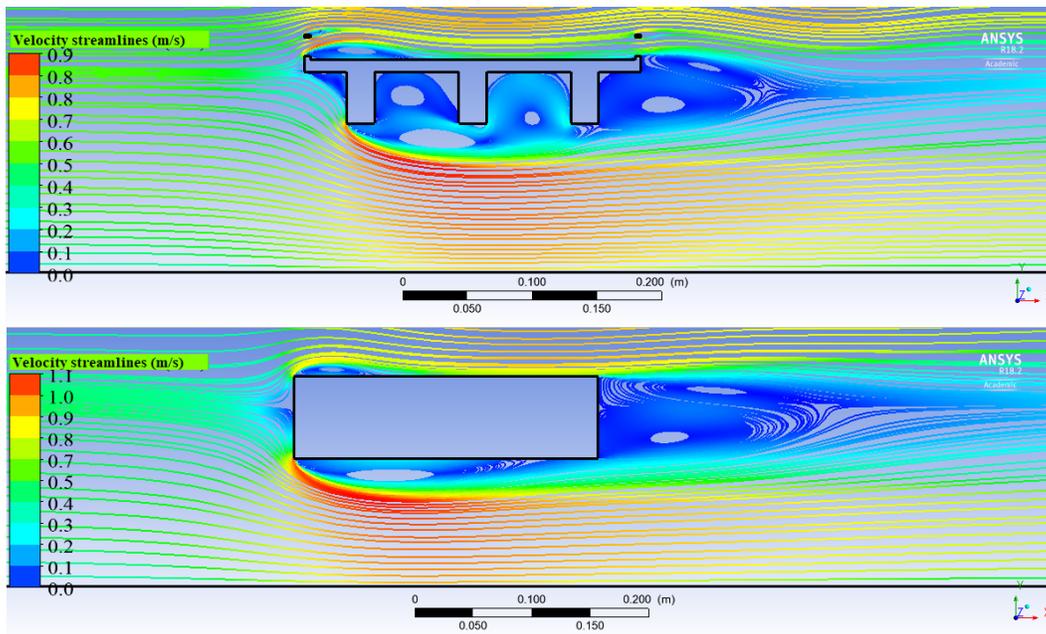
Figure 4- 32 velocity streamlines for three girder deck and box deck, Fr= 0.32, h*=2.
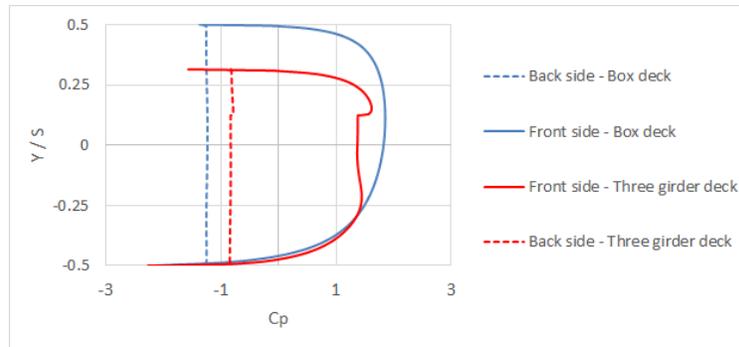
Figure 4- 33. Pressure coefficient in front and back side of the cylinder versus three girder deck, Fr =0.32, h*=2.

4.3 Incipient failure analysis

In the previous section, it was shown how inundation ratio (h*), proximity ratio (P_r), and blockage ratio (B_r) are influencing the hydrodynamic forces on the bridge deck. However, it is not straightforward to understand when the failure of the bridge is occurring by only considering force coefficients. In this section, incipient failure analysis is performed to calculate the threshold of motion of bridge (which is considered as the starting point of failure). The bridge deck is considered as a Hollow box girder with 48% of voids inside the box. One typical cross-section of a hollow box girder is shown in Figure 4- 34.
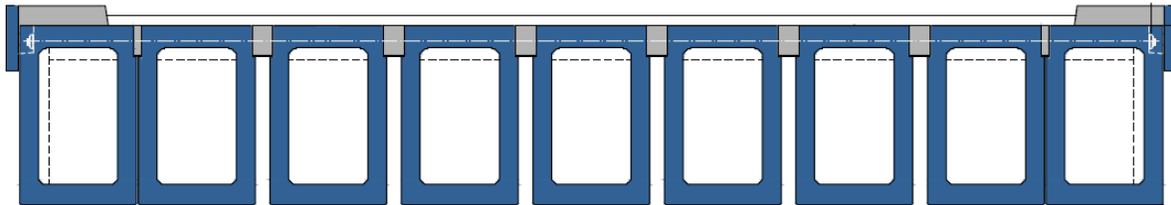
Figure 4- 34. Typical cross-section of a hollow box girder [35].

4.3.1 Incipient failure of Bridge deck with rectangular cross-section (hollow box girder)

By combination of four Froude numbers (0.3, 0.45, 0.65, 0.8), four inundation ratios (0.5, 1, 2, 3), and four proximity ratios (1.5, 2, 2.5, 3), 64 simulations were performed to calculate hydrodynamic forces on the bridge deck. The forces from numerical simulations were compared with the resisting forces, and failure was defined when the ratio of driving forces divided by resisting forces becomes equal or greater than 1. The resisting force in the horizontal direction is provided by frictional force. The weight of the deck is the resisting force in the vertical direction. The positive moment, which is caused by the weight of the deck, acts as a resisting moment. The reader is referred to Appendix 4 for more information about resisting and driving forces.

One important factor in terms of resisting forces is the type of bearing which determines the friction coefficient. Bearings allow built-in movement of the bridge deck to accommodate thermal expansion and shear stress strains. They are also used to transfer forces from the superstructure to the substructure. Several types of bearings are available, each of which has its own characteristic and friction factor. Elastomeric bearings are one of the most commonly used bearing types that are now in service in tens of

thousands of bridges. This type of bearing has a friction factor in the range of 0.2 to 0. 3 [36] [37]. Hence friction factor of 0.25 is considered for the incipient failure analysis.

Figure 4- 35 Example of elastomeric bearing between bridge pier and deck [38].

Simulations were performed for four different proximity ratios, p_r, ranging from 1.5 to 3. Results of stability analysis for the highest proximity ratio, 3, is shown here. Results of other proximity ratios are shown in Appendix 2.
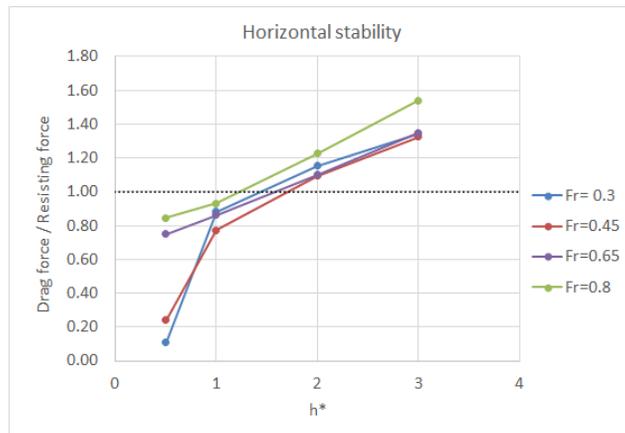
Figure 4- 36 Horizontal stability of hollow box girder with P_r= 3.
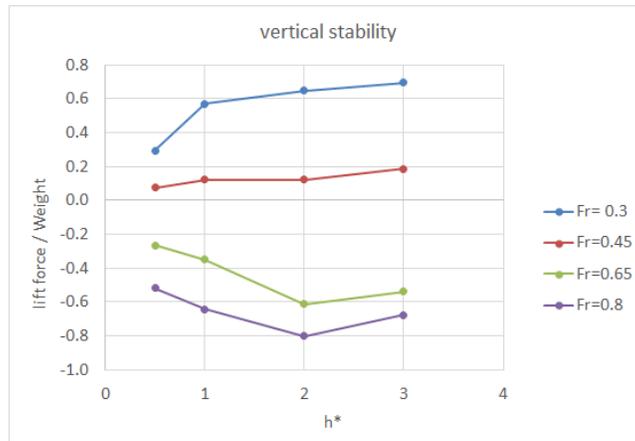
Figure 4- 37 Vertical stability of hollow box girder with P_r= 3.
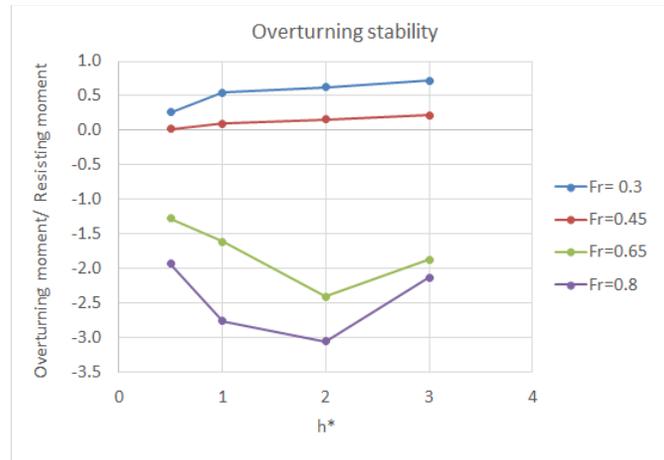
Figure 4- 38. Overturning stability of hollow box girder with $P_r = 3$.

Regardless of proximity ratio and Froude number, the bridge deck collapsed when the inundation ratio was in the range of 1 .3 to 2. This indicates that the deck is more susceptible to high water levels than flood velocity or distance to the channel floor. Moreover, no failure of bridge occurred for inundation ratios lower than 1.3, indicating that the deck must be deeply submerged to fail. No failure resulted due to the vertical instability or overturning moment for the range of studied h*, P_r, and Froude number. However, as was indicated in Chapter 2, several failures of bridge decks by overturning moment have been reported in the real world. It can be said that the two parameters contributing to the overturning instability are probably the trapped air beneath the girder and the accumulated debris in front of the deck. Neither of these two parameters was part of these simulations, resulting in no failure due to overturning moment.

By extracting the starting point of failure for different h*, P_r, and Froude numbers, contour lines of the threshold of failure can be extracted, Figure 4- 39. The numbers in the graph demonstrate the blockage ratio (B_r) for each failure points.

Figure 4- 39 depicts that for P_r higher than 2 (which is common for bridges), by increasing the proximity ratio, failure occurs at lower h*. In fact, a lower level of water is enough to cause failure of the bridge when it is located further from the channel floor. This indicates that a higher distance of the deck from the channel floor is more dangerous for the stability of the bridge. Figure 4- 39 also indicates that most of the failure starts to happen in the relatively small range of blockage ratio between 0.22 to 0.28.
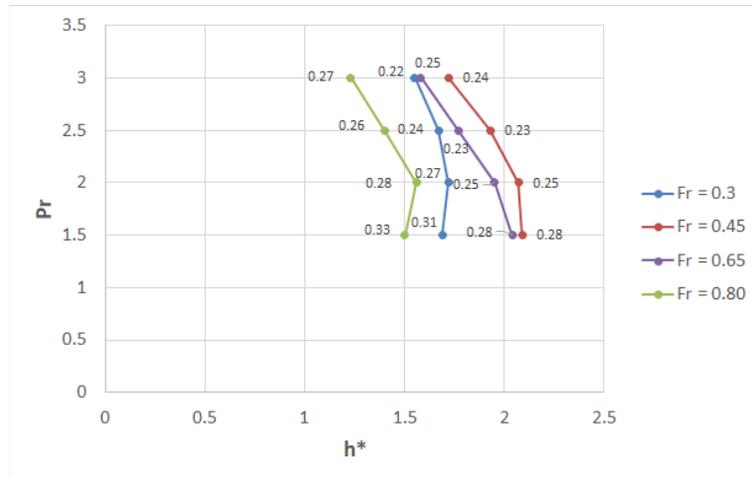
Figure 4- 39 Contour lines of the threshold of failure for box deck with different h*, P_r and Froude number.

These contour lines of the starting point of failure can be considered as a great tool for bridge designers to assess the stability of the bridge under extreme hydrodynamic forces. This graph provides the basis for a more accurate estimate of failure of the bridge due to flood loadings and can be considered to be included in the bridge design codes and guidelines. In fact, this proposed method is more sophisticated than the traditional method of considering a constant value of drag and lift which is still present in some guidelines such as AASHTO Load and Resistance Factor Design (LRFD) Bridge Design Specifications and Eurocode.

As was indicated in section 2.5.2, based on the Eurocode design code, the drag coefficient for a rectangular cross-section deck is 1.44. Based on this constant drag coefficient, contour lines of the threshold of failure are shown in Figure 4- 40. Since the effect of lift is not considered in Eurocode, the stability of bridge is lower, which results in an incorrectly conservative approach.
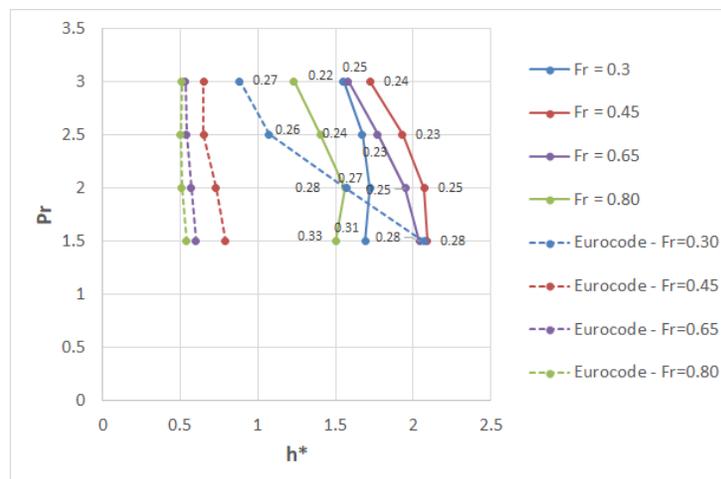
Figure 4- 40. Comparison of contour lines of the threshold of failure between Eurocode (CD=1.44) and this research for a box deck.

It should be noted that in establishing above figures some assumptions have been made. One of the critical assumptions was the friction factor between the deck and pier. To avoid additional assumptions,

65

drag coefficient can be plotted based on the inundation ratio, proximity ratio and Froude numbers, Figure 4- 41.
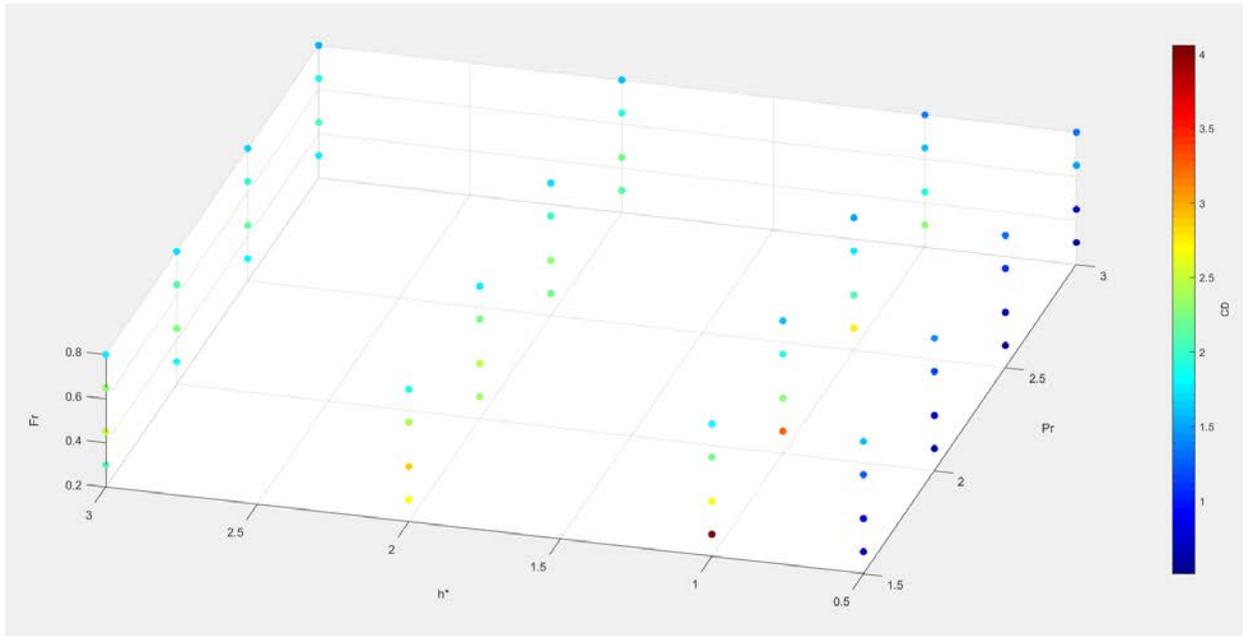
Figure 4- 41. Drag coefficient for box deck based on the proximity ratio (p_r – 1.5,2,2.5,3), inundation ratio (h^*- 0.5,1,2,3), and Froude number (Fr – 0.30,0.45,0.65,0.80).

4.4 Comparison of the stability of hollow box deck versus slab deck

Typical section of hollow box deck, Figure 4- 34, has a lower aspect ratio (ratio of length over the height of the deck) than that of slab deck, Figure 4- 42. This higher aspect ratio of the slab deck could result in lesser drag force and hence more stability of the deck. To compare the stability of these two types of decks under an extreme hydrodynamic situation, incipient failure analysis was performed for two decks with aspect ratios of 5.7 and 18, representing the average aspect ratios for hollow box girder and slab deck, respectively.
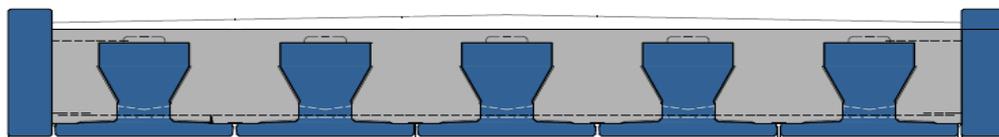
Figure 4- 42. Typical cross section of a slab deck [35].

Figure 4- 43 depicts that hollow box deck has a lower horizontal stability ratio than that of slab deck. In fact, the failure of the bridge only occurred for hollow box deck at low velocities, Fr=0.3. It is important to note that although slab deck is completely filled with concrete, it has a lower weight than hollow box girder, Table 4- 1. This fact implies that not only the slab deck is more favourable from a hydraulic perspective but also it is more economical.
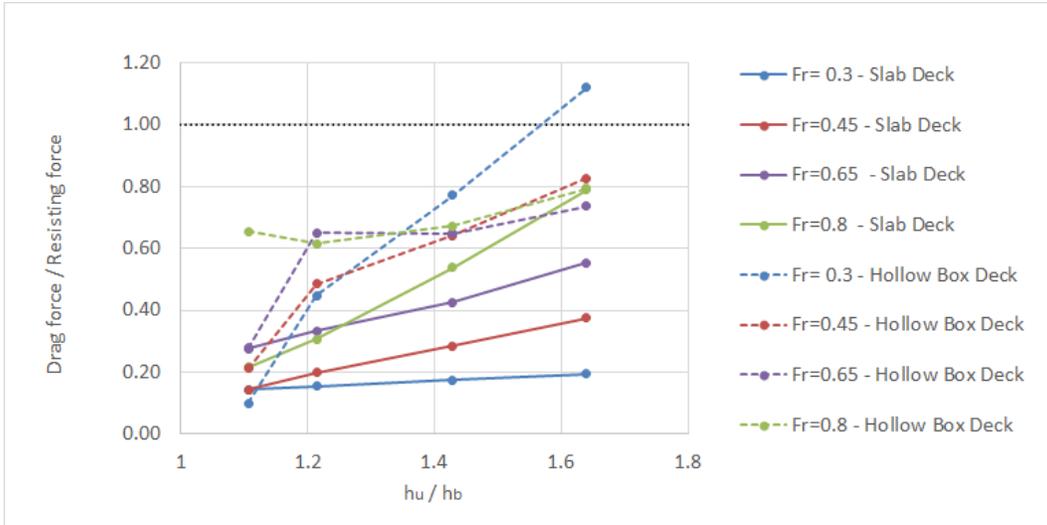
Figure 4- 43. Comparison between the horizontal stability of hollow box girder versus slab deck stability.

	Length (m)	Height(m)	Aspect ratio	Void %	Filled volume (m3)
Hollow box deck	0.26	0.045	5.7	48	$6*10^{-3}$
Slab deck	0.26	0.0144	18	0	$3.7*10^{-3}$

Table 4- 1. Dimension of hollow box deck versus slab deck.

Neither slab deck nor hollow box failed due to vertical or overturning instability. However, it is not straightforward to establish a general trend of changes in vertical or overturning stability for the two studied decks.
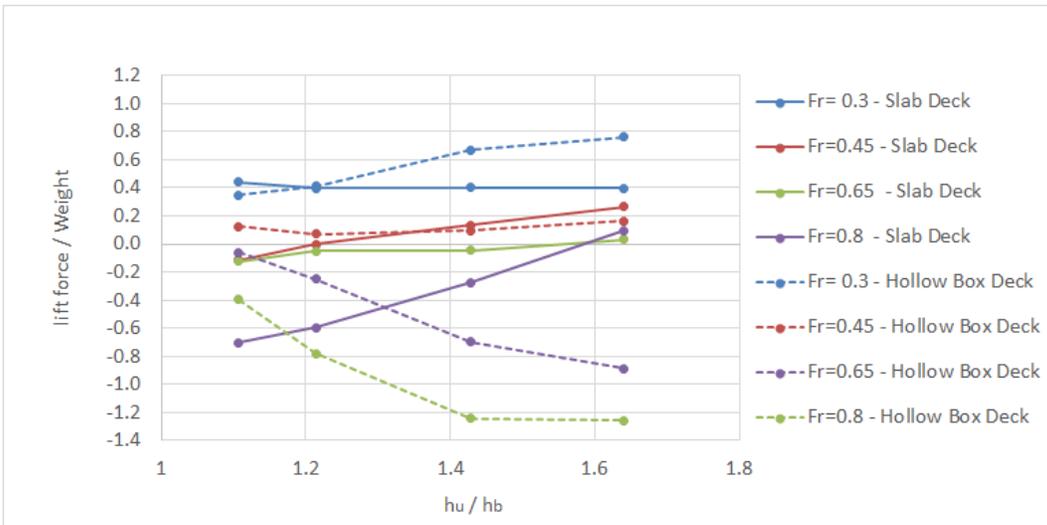
Figure 4- 44 Comparison between the vertical stability of hollow box girder versus slab deck stability.

67
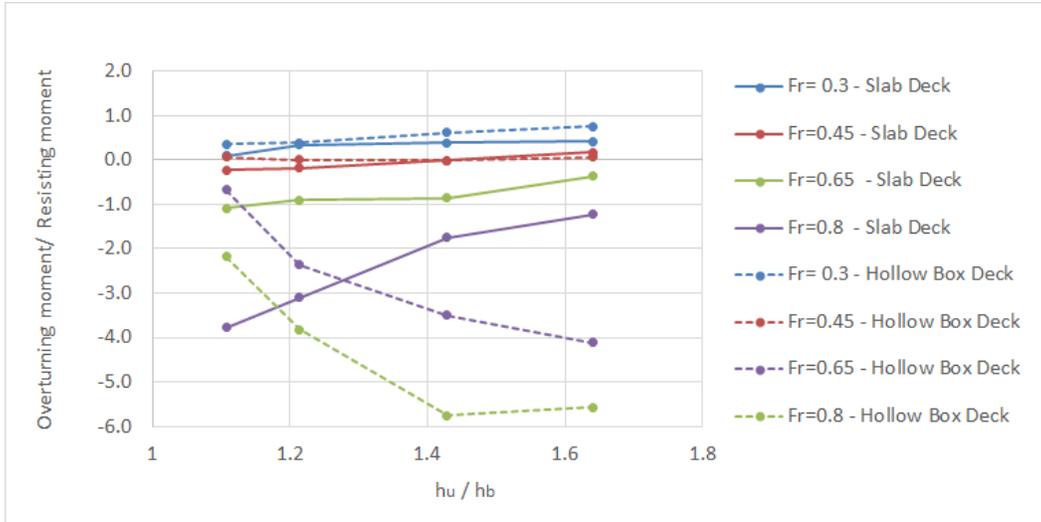
Figure 4- 45 Comparison between the overturning stability of hollow box girder versus slab deck stability.

4.5 Effect of inclination on the stability of hollow box girder

In some cases when the bridge is located on the curvature, introducing superelevation is unavoidable to provide more safety for high-speed vehicles. The rate of superelevation depends on several factors including maximum allowable speed, the degree of curvature, and weather conditions. To investigate the role of superelevation on the flow pattern around the bridge, box deck superelevated 5 degrees on the upstream side was placed in the numerical flume for Froude number ranging from 0.15 to 0.45. The average velocity distribution for level and inclined deck at Froude number of 0.3 is shown in Figure 4- 46.
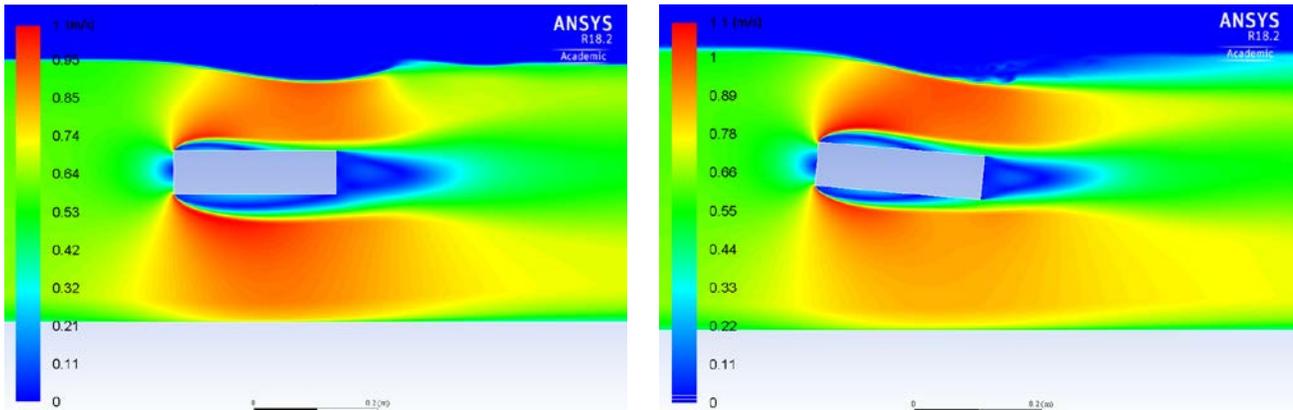
Figure 4- 46. Average velocity distribution around level and inclined box deck, Fr=0.3, h*=3.

The deformation of the free surface is higher in case of the inclined deck than that of the level deck which results in higher velocities above the inclined deck and hence positive lift, Figure 4- 46 - Figure 4- 49. Moreover, distribution of streamlines around the deck demonstrates that in case of inclined deck, formation and distribution of eddies around the deck are symmetric in horizontal axis which results in the same trend of pressure distribution on the upper and lower face of the deck, Figure 4- 48.

68
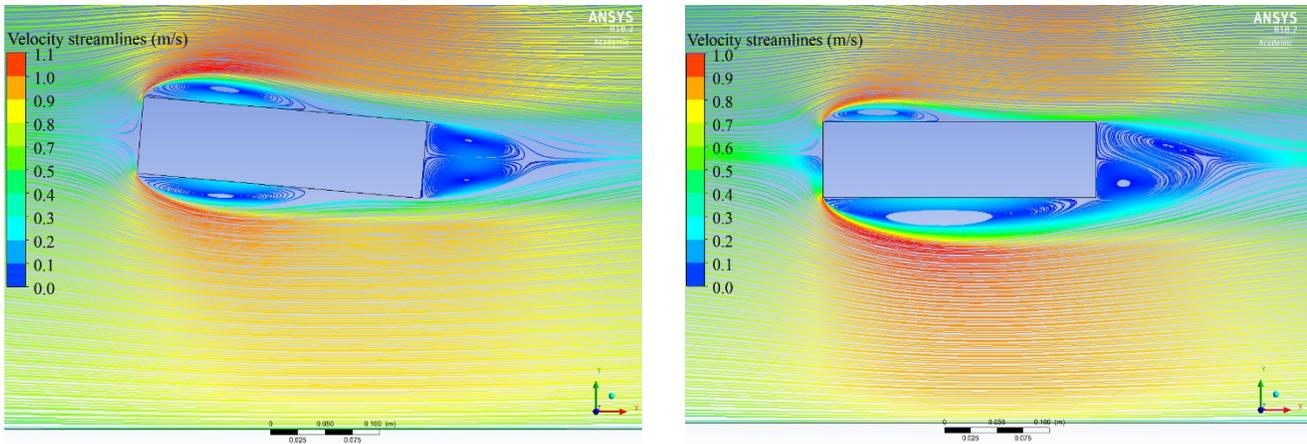
Figure 4- 47. Velocity streamlines for level deck and inclined deck (5^0), Fr= 0.32 , h*=3.
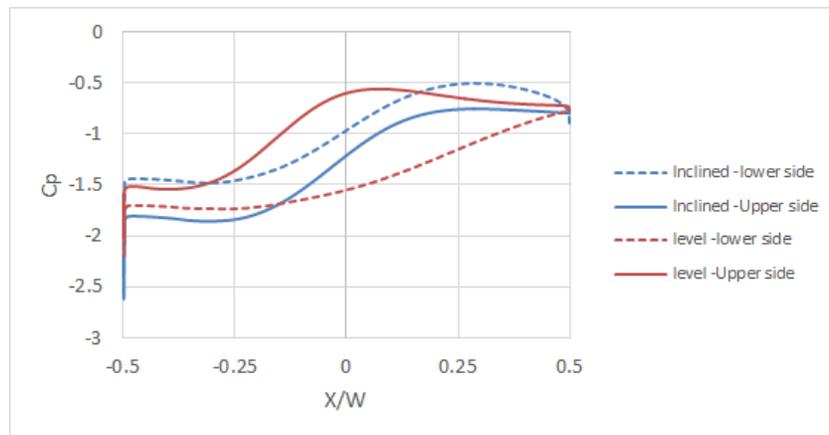
Figure 4- 48. Pressure distribution around inclined and level deck for h*=3, Fr= 0.32.

Regardless of h* and Froude number, the level deck has more negative lift coefficient. The inclination of the deck also results in reattachment of the boundary layer in the bottom side of the deck which did not occur for the level deck. It can also be seen that the detached boundary layer on the leading edge of top side of the deck reattaches to the deck at the further downstream side of the deck.
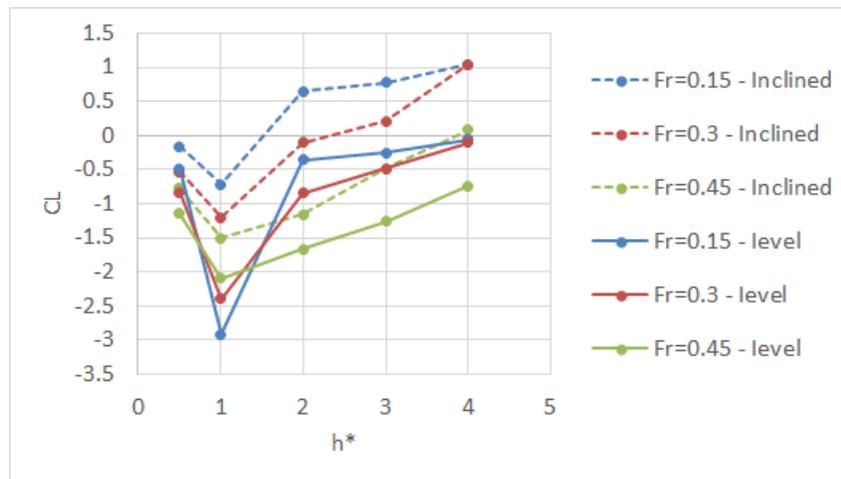
Figure 4- 49. Comparison of lift coefficient of level and inclined box deck.
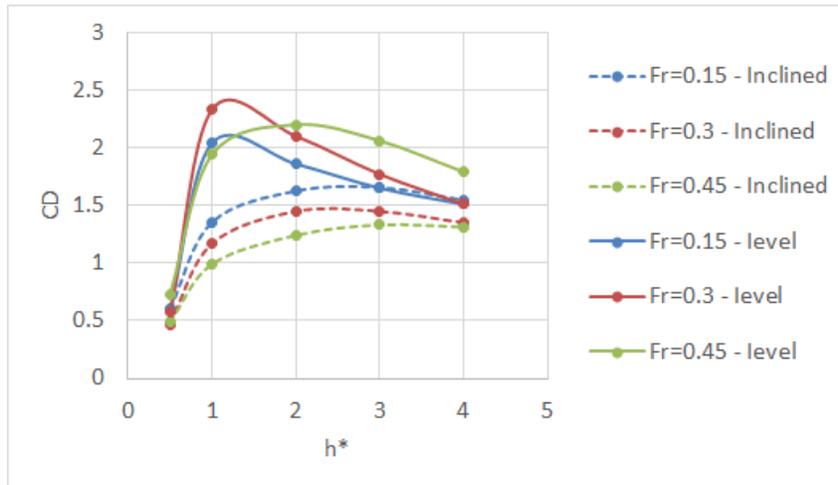
Figure 4- 50. Comparison of drag coefficient of level and inclined box deck.

Results of incipient failure analysis also indicate that the overall stability of the deck is reduced when there is inclination of the deck. Whilst the level deck did not collapse for Froude number of 0.15, 5% inclination of the deck resulted in the horizontal failure of the deck at h*=3.5. Moreover, the vertical and overturning stability of the deck is reduced for the inclined deck, however, not sufficiently to have caused a failure.
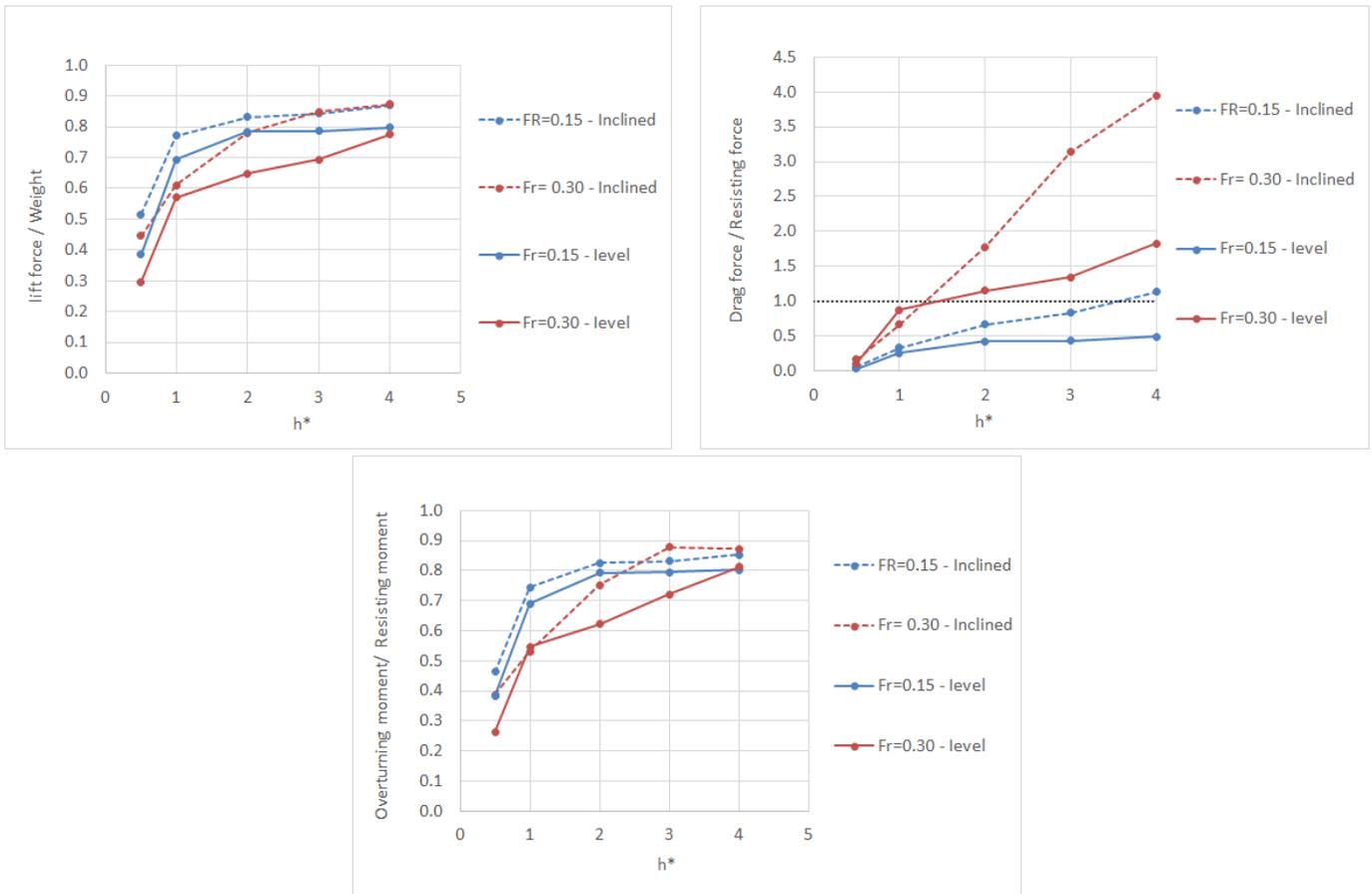
Figure 4- 51. Incipient failure analysis for level and inclined box deck.

70

4.6 Countermeasure for mitigation of flood effect on bridge decks

In the previous section it was depicted that when the deck is fully submerged, the collapse of the bridge is highly probable due to the lack of resistance to the horizontal flood force. Failure of the bridge deck is affected not only by the severance of flood but also by the geometry of the deck. In this section, it is proposed that by adding wings to the sides of the deck, the stability of the bridge could be increased. In order to assess this hypothesis, six types of wings were considered as follows:
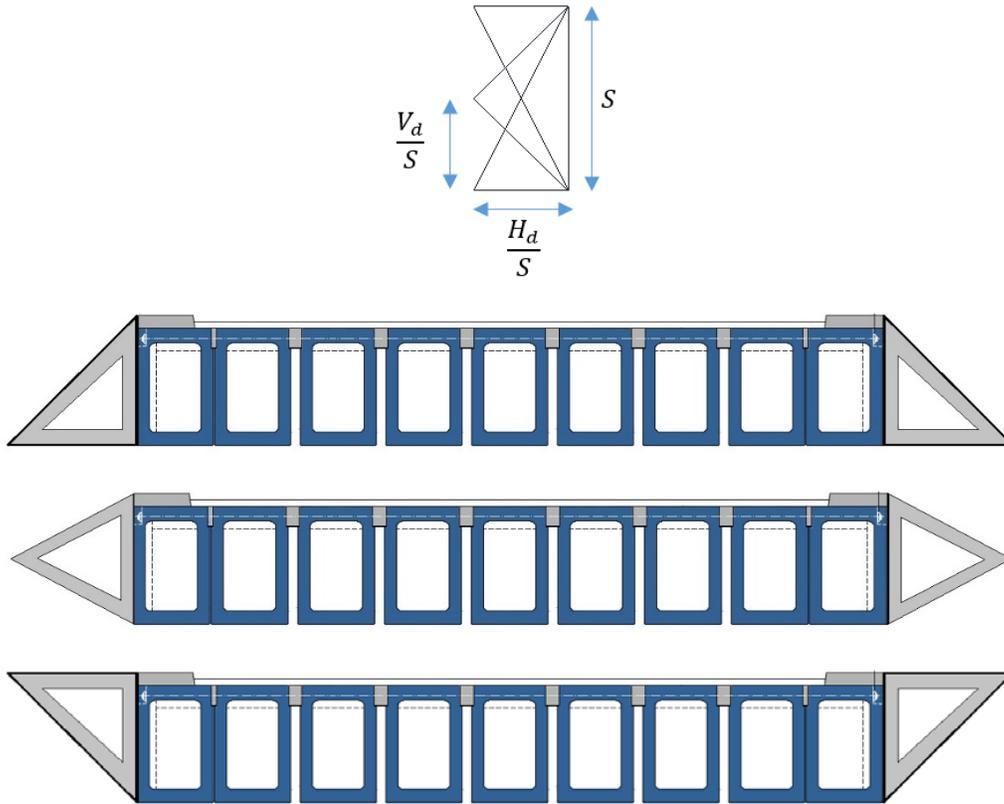
Figure 4- 52. Schematic shape of the deck using wings for mitigating flood effect.

	Scenario 1	Scenario 2	Scenario 3	Scenario 4	Scenario 5	Scenario 6
$\dfrac{V_d}{S}$	1	0.5	0	1	0.5	0
$\dfrac{H_d}{S}$	0.5	0.5	0.5	1	1	1

Table 4- 2 dimension of the wings to the side of the deck as the countermeasures.

To investigate the efficiency of each of these wings in reducing hydrodynamic forces, simulations were performed for each scenario separately.
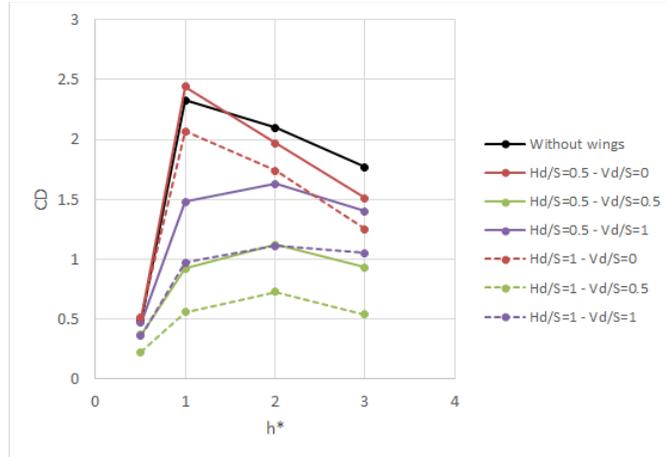
Figure 4- 53 Drag coefficient versus h* for six different geometry of wings. (P_r =3, F_r =0.3).

Figure 4- 55 indicates that for all the scenarios (except Scenario 3 at h*1) adding wings to the superstructure results in lower drag force in comparison with the deck without any wings. However, the magnitude of this reduction in drag force is highly dependent on the profile shape of the wing. The wing with the sharp corner at the middle height of the deck, $\frac{Vd}{s} = 0.5$, results in the lowest drag force. In contrast, the reduction in the drag force is smallest when $\frac{Vd}{s} = 0$. Moreover, regardless of the magnitude of $\frac{Vd}{s}$, increase of $\frac{Hd}{s}$ amplifies the effect of the wing, which results in a lower drag force.
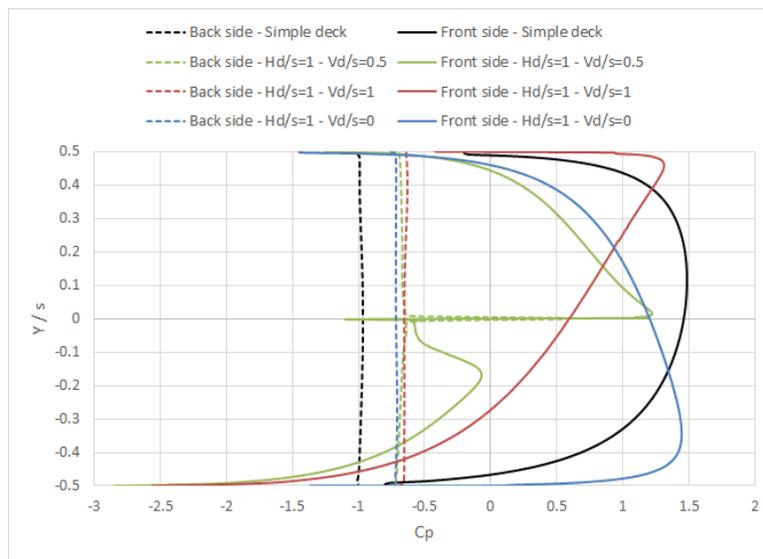
Figure 4- 54. Pressure coefficient in front and back side of the deck for six different geometry of wings, h=3, Fr =0.3.*

Less negative pressures at the back side of the deck, as well as the smaller positive pressure in the front side of the deck, contribute to the smaller drag force in case of the deck with wings, Figure 4- 46. It can also be seen that the smallest drag force that occurs for $\frac{Vd}{s} = 0.5$, is mainly due to the suction at the lower slope of the front side of the deck.
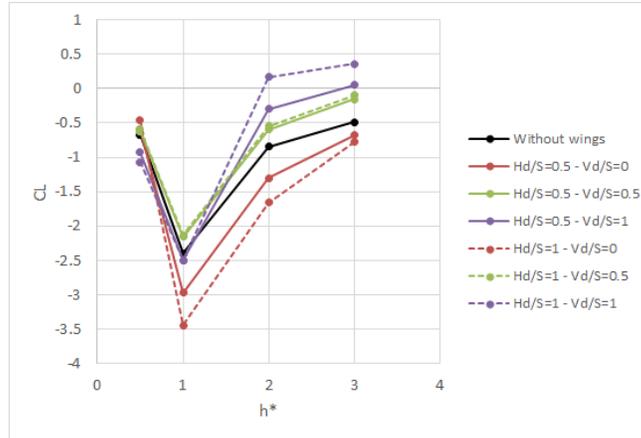
Figure 4- 55 Lift coefficient versus h* for six different geometry of wings. (P_r =3, F_r =0.3).

Figure 4- 55 depicts that the influence of wings on the lift force can differ dramatically based on the shape of the wings. Generally, whilst the wing with $\frac{Vd}{s}$=0 results in a more downward force, other wings result in lower downward force in comparison with the deck without any wings. Same as the influence of $\frac{Hd}{s}$ for drag force, an increase of $\frac{Hd}{s}$ amplifies the effect of the wing, which results in higher downward force for $\frac{Vd}{s}$=0, and lower downward force for the two other cases. However, the effect of increase in $\frac{Hd}{s}$ on lift force is not as significant as the effect of that on drag force. This indicates that lift force is more sensitive to the $\frac{Vd}{s}$ than $\frac{Hd}{s}$.

In the incipient failure analysis, it was seen that the failure of the deck due to the horizontal forces is more probable than that of the vertical or overturning moment. Considering that in mind, the wing shape that results in lower drag force is more favourable, hence, from the hydrodynamic perspective, the Scenario 5 wing type ($\frac{Hd}{s} = 1$, $\frac{Vd}{s} = 0.5$) can be considered as the more efficient type of wings amongst the studied six scenarios. However, Scenario 5 is not the most economical case as it does not increase the upper surface of the bridge. Scenario 4 can be considered as the most efficient type of wing because it reduces the drag force and also it provides an additional area on top of the deck that can be used as a pedestrian area.

In order to assess the capability of this countermeasure in the extreme hydrodynamic conditions, the incipient failure analysis was performed for the deck with the Scenario 5 wing. Results were compared with the deck without any wings.
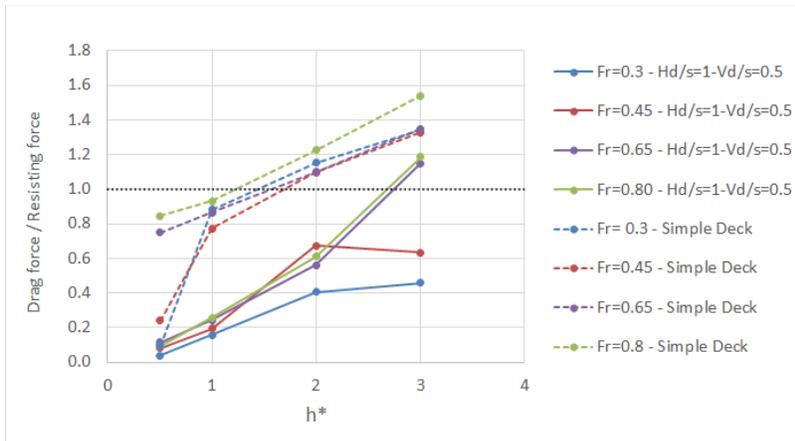
Figure 4- 56. Comparison of horizontal stability of simple deck with Scenario 5 wings attached to the deck.

Figure 4- 56 indicates that the Scenario 5 wing type can be considered as a good mitigation measure for the horizontal stability of the superstructure of the bridge. Whilst for the simple deck shape, failure occurred for all the range of studied Froude number, in case of the deck with Scenario 5 wing, failure only occurred for the significantly high flow velocities, i.e., Froude number of 0.65 and higher. Moreover, failure, in this case, was postponed to the inundation ratio of greater than 2.5. However, one should note that under inundation ratio of greater than 2.5 and with Froude number of greater than 0.65, concerns about the safety of the deck might not be the first priority as compared with the risk of flooding of the large part of the upstream land. Therefore, the proposed countermeasure can be considered as a robust solution for the wide range of probable floods in the real world.
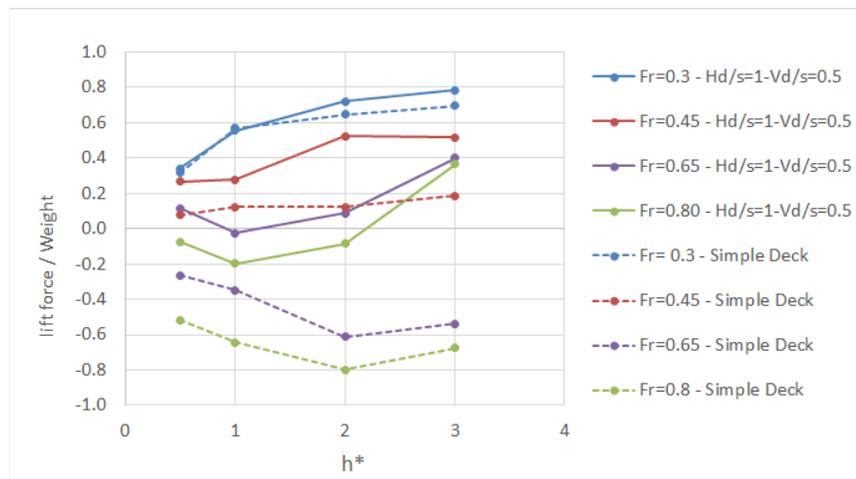
Figure 4- 57 Comparison of Vertical stability of simple deck with Scenario 5 wings attached to the deck.
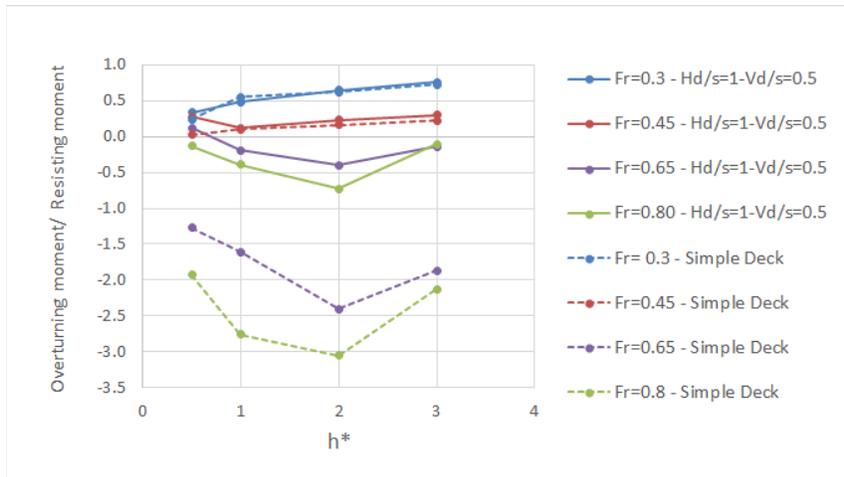
Figure 4- 58 Comparison of overturning stability of simple deck with Scenario 5 wings attached to the deck.

As far as the stability of the bridge in the vertical direction or resistance against overturning moment are concerned, it can be seen that the simple deck without any wings has a little higher stability value than that of the deck with wings. However, the stability of the deck is not endangered by the lift force or overturning moment as the stability ratios in these cases are far away from the failure point.

By extracting the starting point of failure for different h*, P_r, and Froude numbers, contour lines of the threshold of failure can be extracted for the case of the deck with attached wings (scenario5), Figure 4- 59. The numbers in the graph demonstrate the blockage ratio (B_r) for each failure points.
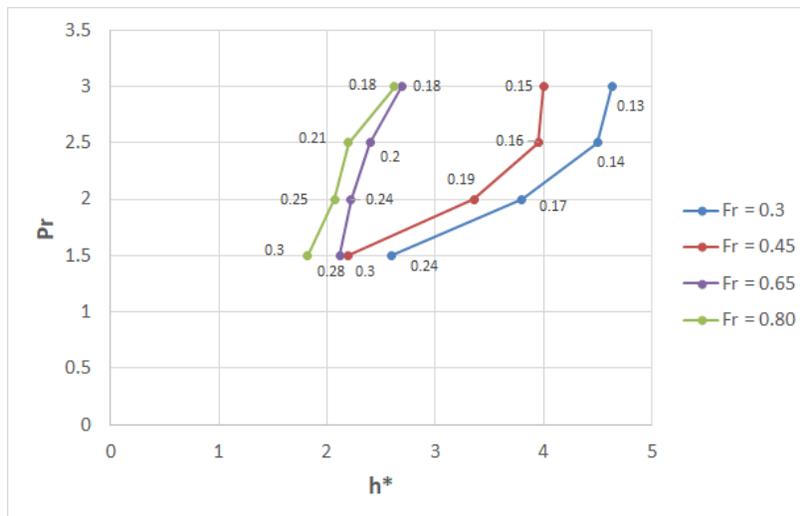
Figure 4- 59 contour lines of the threshold of failure for Scenario 5 wings attached to the deck.

By comparing Figure 4- 39 with Figure 4- 59 it can be seen that adding wings to the deck has resulted in more stability of the deck. Whilst for the simple deck starting points of failure mostly occurs between h* of 1.5 to 2, Figure 4- 39, in the case of the deck with wings (Scenario 5) failure occurs at higher inundation ratios up to h*=4.5, Figure 4- 59.

4.7 Effect of scaling on hydrodynamic forces and the centroidal moment

To investigate the effect of scaling on the hydrodynamic forces on the deck, the lab dimension of the deck (width= 0.07m, length= 0.26m) was scaled to the real size dimension by a scale factor of 40. Figure 4- 61 shows that the trend of changes in forces and centroidal moment coefficients will not differ by scaling up the model. However, there are small differences in terms of the magnitude of forces and centroidal moment coefficients.
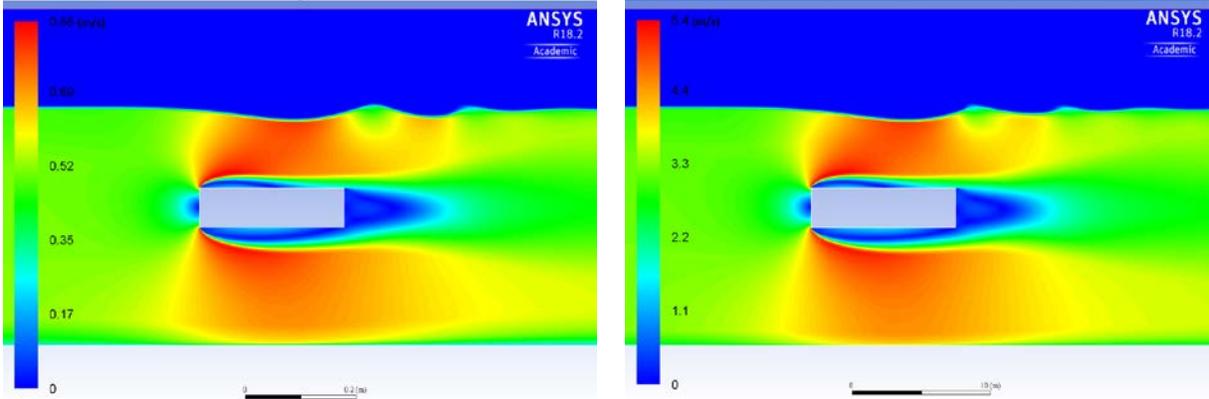
Figure 4- 60. Comparison of velocity profile around the deck for lab size (left) and big scale deck (right), Fr= 0.25, h* =3, Pr=3.
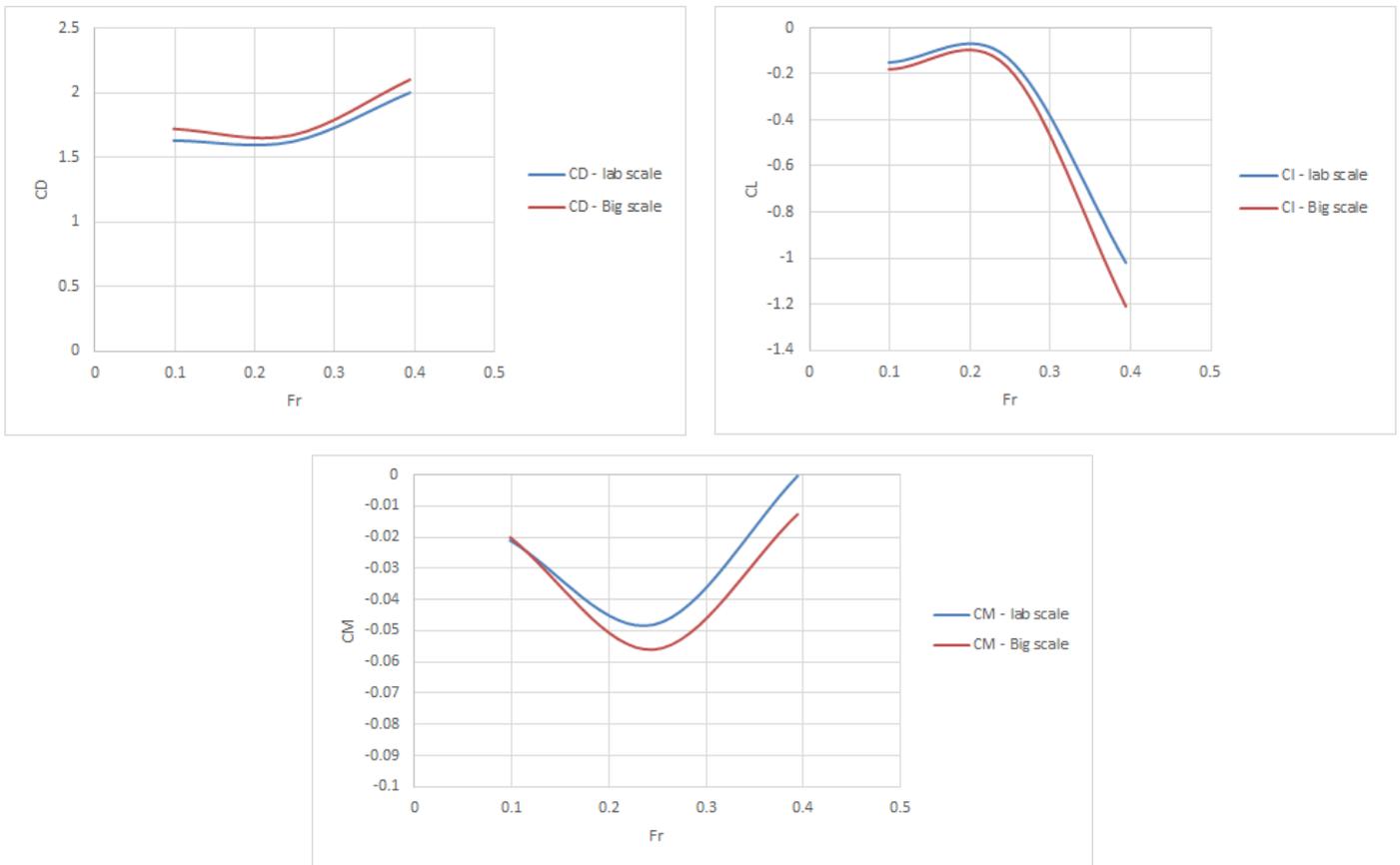
Figure 4- 61. Effect of scaling on the drag, lift, and overturning moment.

While for streamlined geometries without sharp edges, drag force is highly dependent on the separation point and hence Reynolds number, it can be considered that for the sharp-edged geometries drag force is relatively independent of the Reynolds number. However, results of this simulation depict that there is a small difference between drag, lift and, moment coefficient of lab scale (low *Re*) and full-scale (high *Re*). There are some points that could explain the possible cause of this difference:

- While for sharp-edged bodies in unbounded uniform flow, drag force is relatively independent of the Reynolds number, the presence of free surface might influence the validity of this statement for bounded flow.
- The relative importance of inertia force compared with surface tension can be expressed by the Weber number as follows:

$$W_e = \frac{\rho V^2 L}{\sigma}$$ (4-2)

Where *V* is the flow speed, *L* is the characteristic length (depth of water above the deck), *ρ* is water density, and *σ* is surface tension (0.072 N/m). Approximate values for Reynolds, Froude, and Weber number for lab scale and full scale is shown in Table 4- 3.

|	Re	Fr	We
Lab Scale	$84000 - 336000$	0.1 -0.4	76-1228
Full Scale	$2.1*10^7 - 8.5*10^7$	0.1 -0.4	$1.2*10^5$ - $1.9*10^6$

Table 4- 3. Comparison of Reynolds, Froude, and Weber number of lab-scale and full-scale.

As the Froude number was used for scaling, it is the same for lab and full scale. If Reynolds number is greater than 10^5, effects of viscosity can be neglected [39]. While in the full-scale size, Reynolds number is way higher than 10^5, for some cases in the lab size Reynolds number was less than 10^5 which can cause some scaling effect.

In literature, a wide range of minimum Weber numbers is presented above which the effects of surface tension should be negligible. The upper and lower boundaries of this critical Weber number can be considered as 120 [40] to 500 [39]. While in the full-scale size, Weber number is way higher than 500, for some cases in the lab size Weber number was less than 500 which can cause some scaling effect.

- Results of some experimental research in wind tunnel proved that the drag coefficient of a box can be increased slightly at high Reynolds number [41].
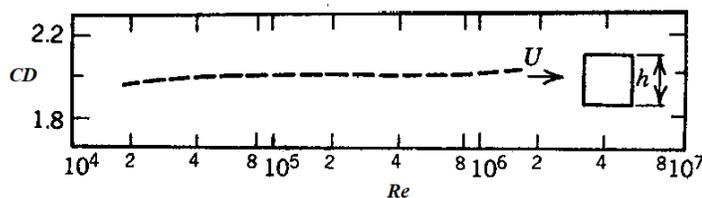
*Figure 4- 62. Drag coefficient versus Reynolds number [41].*

5 Conclusion and Recommendations

The main findings of this research are summarized in this chapter. The answers to the main research questions are given based on the results of numerical simulations. The recommendations for further researches in the realm of this topic are made based on the results and limitations of current research.

5.1 Conclusion

The main findings of this research are presented based on the key research questions:

A- What are the contributing parameters and critical hydrodynamic situations that lead to the failure of river bridges?

Results have shown that forces on the bridge deck, regardless of the shape of the deck (Box deck or three girder deck), are highly dependent on the depth of the upstream flow (hu), distance between the deck and channel floor (hb), Froude number (Fr), thickness of the deck (S), Aspect ratio of the deck, inclination of the deck, and Blockage ratio (Br). Preliminary investigation on effects of these parameters on the final stability of the deck indicated that effect of each of these parameters cannot be considered regardless of the magnitude of rest of the parameters. For instance, the effect of distance between the deck and channel floor is highly dependent on the magnitude of the upstream water level and velocity. Therefore, incipient failure analysis was performed to determine in which situation failure is expected while considering all the above-mentioned parameters into account. The summary of the main findings is presented here:

➤ By considering the trend of changes in lift and drag force simultaneously, it can be said that the combination of a small velocity and inundation ratio higher than 2 results in the most critical situation for the vertical stability of the bridge deck.

➤ Regardless of the proximity ratio and the Froude number, the bridge deck collapsed when the inundation ratio was higher than 1.3. This indicates that the deck is more susceptible to high water levels than flood velocity or distance to the channel floor. Moreover, no failure of bridge occurred for inundation ratios lower than 1.3, indicating that the deck must be deeply submerged to fail.

➤ The lift force was found to be downward unless the deck is significantly submerged (h*≥3.5) and the upstream velocity is relatively small (Frd < 0.6). In fact, for h*<3.5 the development of flow patterns on the upper side of the deck is constrained by the presence of the free surface which causes an asymmetric pressure distribution in the vertical direction and ultimately results in a downward force, Figure 4- 15. An increase in velocity results in a more downward force and hence more stability of the bridge (provided that the submergence of the bridge is not too high) which ultimately can exceed the upward buoyancy force when Frd is 0.97 or higher, Figure 4- 7.

➤ The contours representing the starting point of failure indicate that by increasing the proximity ratio, failure occurs at a lower h*, Figure 4- 39. In fact, a lower level of water is enough to cause failure of the bridge when it is located further from the channel floor. This indicates that larger the distance of the deck to the channel floor the more dangerous it is for the stability of the bridge.

➤ Regardless of the inundation ratio or Froude number, inclination of the deck results in lesser downward lift and smaller drag coefficient. Results of incipient failure analysis also indicate that the overall stability of the deck is reduced when there is an inclination of the deck.

B- What conclusion can be drawn from a comparison of box deck and girder deck?

Results show that the trend of changes in force and moment coefficients for these two cases are quite comparable, Figure 4- 30. However, the magnitude of these coefficients can differ depending on the shape of the deck and h*. Results indicate that the box deck has a notably higher

drag coefficient than the girder deck. Moreover, trapped air between the girders can increase buoyancy and contribute to the failure significantly. For establishing an accurate failure graph and analysing the stability of the bridge, one needs to consider each deck with its own force coefficients separately.

C- What conclusion can be drawn from a comparison of the stability of hollow box girder versus slab deck?

A typical section of a hollow box girder has a lower aspect ratio (ratio of length over the height of the deck) than a slab deck. Results indicate that the higher aspect ratio of the slab deck results in lower drag force and hence more stability of the deck. Moreover, the box girder has notably higher buoyancy which decreases the stability. This implies that the slab deck is more favourable from a hydraulic perspective.

D- What is the upper boundary of drag force for the box deck?

Regardless of the deck Froude number, an increase in blockage ratio results in an increase in drag coefficient. This rise in drag coefficient is due to both an increase in pressure on the front side, and also an increase of negative pressure on the back side of the deck. This implies that the constant drag coefficient of 2 to 2.2 which is suggested by Hamill (1999) incorrectly neglects the effect of blockage. On the other hand, decrease in blockage ratio shifts the drag coefficient towards the value of 1.56 for a rectangular cylinder in an unbounded flow. However, one should note that the drag coefficient was defined based on the undisturbed upstream velocity. Increase in blockage ratio also results in a higher local velocity around the bridge which can be considered as the main cause of the increase in the drag coefficient, Figure 4- 19.

In the scope of common flow conditions of practical interest for bridge designers, the upper boundary of drag coefficient for the box deck was found to be 2.8. In fact, this value of CD=2.8 can be considered as an upper boundary, since the aspect ratio of the deck was 3.7 which is close to the lower boundary of the aspect ratio of the deck.

E- Based on the results of simulations, what countermeasures can be proposed to avoid such failure mechanisms?

The result of incipient failure analysis indicated that failure due to sliding is more likely to happen than other modes of failure for the box girder. Therefore, reducing drag force, increasing downward lift force, or reducing the buoyancy force can result in more favourable conditions for stability of the deck.

Attaching some wing-shaped structures on the sides of the deck was proposed as a countermeasure to avoid failure of the bridge due to sliding. Although the projected area of the deck perpendicular to the direction of the flow was kept constant, it was expected that CD, CL, and CM would change; since they are dependent on the geometry of the deck, and the flow pattern is altered significantly due to the presence of wings.

Regardless of the shape of the wings, drag force reduced remarkably when wings were attached to the deck. However, the vertical force was strictly influenced by the shape of the wings which implies that inappropriate shape of the wings might increase the upward force and hence endanger the vertical stability of the bridge. Results of several simulations for six different shapes

of wings under different inundation ratios and Froude numbers indicated that a rational shape of the wings can significantly alter the flow pattern around the deck and postpone the occurrence of failure during conditions of really high water levels (h*>2.5) and high flood velocity (Fr>0.65). The proposed countermeasure can be considered as a robust solution for a wide range of probable floods, because of the fact that firstly, the occurrence of this extreme hydrological situation is rare, and secondly, the stability of the deck in that situation might not be the first priority, especially compared with the risk of flooding a large part of the upstream land.

5.2 Recommendations for future research

Based on the main findings of this report, some gaps in knowledge were found that can be addressed in future research:

➢ This research focused on the hydrodynamic loadings on the deck. However, the presence of other structures nearby the deck including piers and abutments can have an impact on the flow pattern and hence hydrodynamic forces on the bridge. In order to see the effect of the whole elements of the bridge at the same time, it is essential to perform a 3D simulation of flood-bridge interaction.

➢ Several failures of bridge deck due to vertical or overturning instability has been reported in the past decades. However, this research proved that horizontal instability can be the only failure mode for box deck. Two contributing factors to overturning and vertical instability which were not considered in this research are: 1- Trapped air between the girders; 2– the role of debris in failure. Further research is required to consider the role of accumulation of debris in front of the deck and also the impact of trapped air beneath the deck.

➢ The incipient failure analysis was performed in the thesis to assess the stability of the deck. Advancements in Smoothed Particle Hydrodynamic (SPH) has made it possible to perform a full fluid-structure interaction (FSI). By applying the SPH model on High performance computing cluster (HPC), it is possible to see the failure of the bridge and the effect of that on flow patterns simultaneously.

➢ During the validation of the numerical model against experimental data of FHWA for three girder deck, it was noticed that there was some discrepancy between numerical and experimental results for the centroidal moment. Considering the presence of this discrepancy in the research of other researchers (Kornel et al. [13], Bricker at al. [18]), it seems that there is a room for more reliable experimental research on the behaviour of changes of the centroidal moment for the submerged deck.

➢ By extracting the starting point of failure for several h*, Pr, and Froude numbers, contour lines of the threshold of failure were extracted for the box deck design. These contour lines of the starting point of failure can be considered as a great tool for bridge designers to assess the stability of the bridge under extreme hydrodynamic forces. Further simulations are required to establish the same type of graphs for the decks with other geometries (especially girder deck), which ultimately can be implemented in the future guidelines and recommendations for the design of bridges.

➤ This research proved that modifying the bridge geometry by adding wings to the side of the deck can significantly increase the stability of the deck. Modification of the wing geometry (such as more streamlined wing) can result in even higher stability of the deck. This finding is something that needs more investigation.

➤ Lastly, the effect of other contributing parameters such as the slope and roughness of the channel bed and the curvature of the bridge can be investigated in further research.

Appendix 1

The Graphical User Interface (GUI) of Fluent is quite advanced, which has made Fluent a user-friendly software. However, in the case of running Fluent on a computer cluster, one needs to transfer some of the commands from GUI to some text file. This appendix aims to explain the general process that needs to be taken in order to run Fluent on the cluster.

For running any software or code on the cluster, one needs to download a software for remote computing. There are several free software amongst which MobaXterm is highly suggested as it has a sophisticated GUI. After installing MobaXterm (or whatever remote computing software that one prefers) one needs to get access to the computer cluster of their department. To do so, they need their net ID, their password, and remote hostname. Each department has its own remote host. The remote hostname for the TU Delft's Civil Engineering department is hpc08.tudelft.net. Four files are needed to run Fluent on the cluster as follows:

1- Fluent case file: After constructing the model on Fluent one can save their model as a case file: File; write; case
2- Data file: Once one has made their model in Fluent, they need to initialize that before hitting the calculate button. After initializing, the model data can be saved: File; write; case.
3- Journal file: Although all of the required information for the simulation is saved in the case file, some of the data (such as time step, number of iteration, output intervals, UDF files, etc.) are needed to be entered in the journal file. Here is one example of the journal file. (Note: each line that starts with a semicolon in the journal file is just for one's information and is considered as a comment)

```
; read your journal file by rcd command and then your case file name.

rcd Box1.cas y

; Define the place that you want fluent to start with; for instance, compute defaults from a velocity-inlet called "inlet"

/solve/initialize/compute-defaults/velocity-inlet inlet

/solve/initialize/open-channel-auto-init

; Initialize the solution

/solve/initialize/initialize-flow

; Set up auto-save intervals; for instance, 4000

/file/auto-save data-frequency 4000

/file/auto-save append-file-name-with time-step 6

; Time step size; for instance, 0.01 sec

/solve/set/time-step 0.01

; Iterations per time step 20 and 12000 time step

/solve/dual-time-iterate 12000 20

; Write data file

wcd test096_done.cas

exit

yes

exit
```

Before submitting their job on cluster, one can check if their journal file is running without a problem or not, by copying and pasting their journal file texts into the Fluent console.

4- SH file: In order to submit their job to the cluster, one needs to have a file with .sh extension:

```
; define number of required nodes and cores

#PBS -l nodes=1:ppn=20

; define approximate required time of your simulation

#PBS -l walltime=40:00:00

; Load your preferable ansys version; define if your model is 2d or 3d

module load ansys/18.1

export FLUENTLM_LICENSE_FILE=27021@flexserv-f2.tudelft.nl

cd $PBS_O_WORKDIR

NP=`wc -l < $PBS_NODEFILE`

fluent 2ddp -rsh -t $NP -g -cnf=$PBS_NODEFILE -i test177.jou >& output.$PBS_JOBID
```

Once the four above-mentioned files are prepared, one can submit their job in the cluster. Since the cluster is run on the Linux platform, one should know some basic commands on Linux. Here are some of the basic commands that are also very handy:

Submit one's job: *qsub* yourjob.sh

Move to a folder: *cd* foldername

Go back to the previous folder: *cd ..*

View active jobs and available cores on the cluster: *show q*

View active jobs for a specific netid: *qstat -u* yournetid

To find out where one is: *pwd*

To delete a submitted job: *qdel* jobid

Appendix 2

The incipient failure analysis of hollow box girder for proximity ratios of 1.5, 2, and 2.5 is presented in this section:
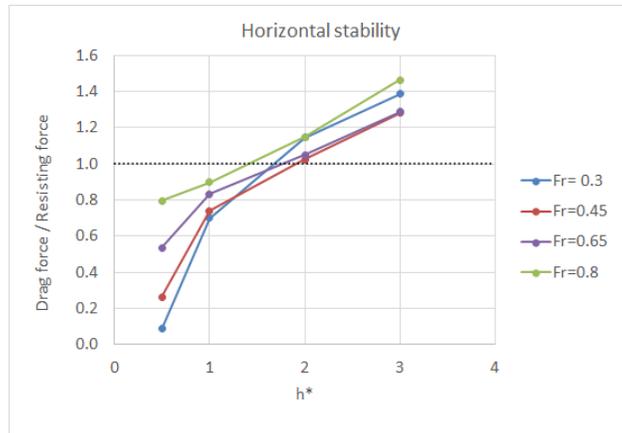
Figure A2- 1. Horizontal stability of hollow box girder with P_r= 2.5.
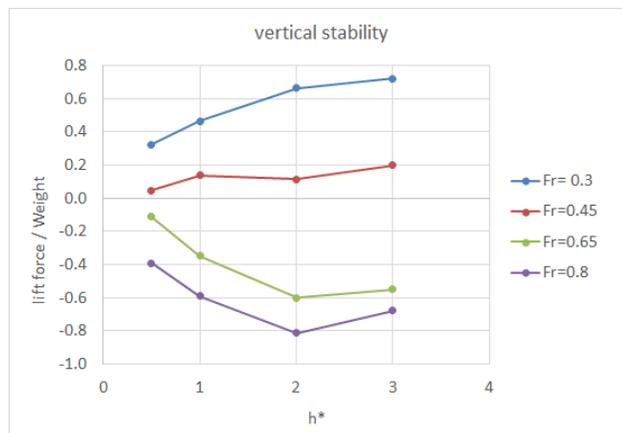
*Figure A2- 2. Vertical stability of hollow box girder with P_r= 2.5.*
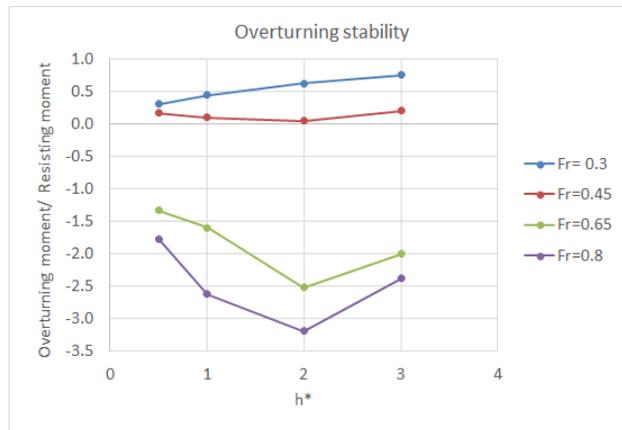
Figure A2- 3. Overturning stability of hollow box girder with P_r= 2.5.
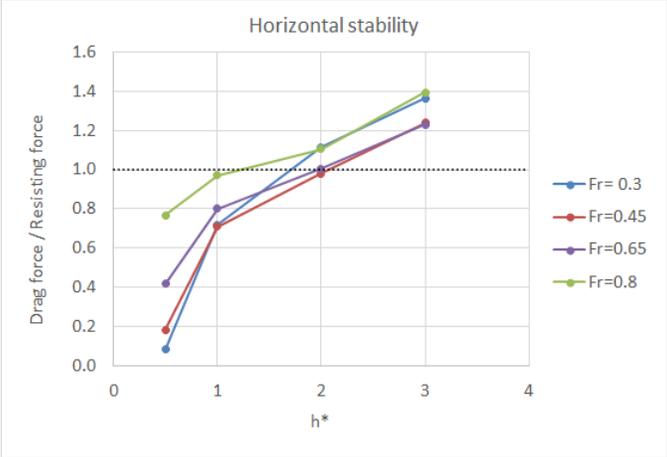
*Figure A2- 4. Horizontal stability of hollow box girder with P_r= 2.*
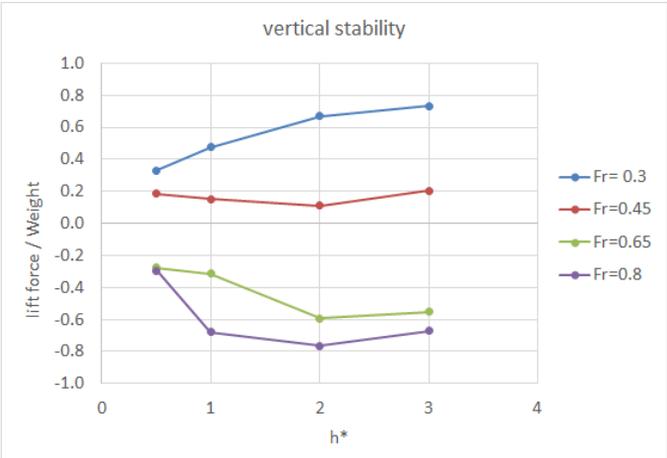
*Figure A2- 5. Vertical stability of hollow box girder with P_r= 2.*
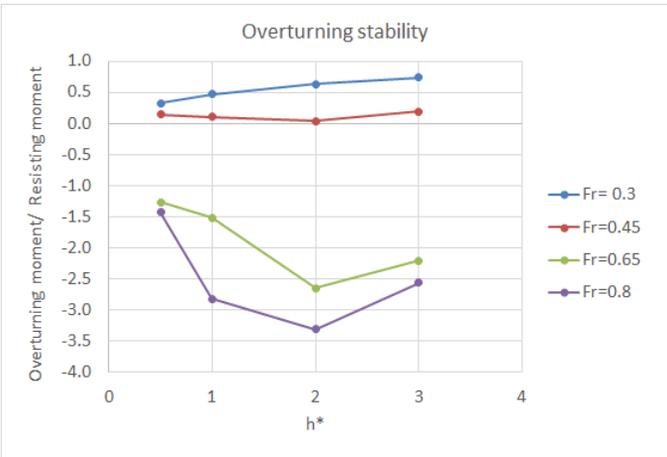
*Figure A2- 6. Overturning stability of hollow box girder with P_r= 2.*
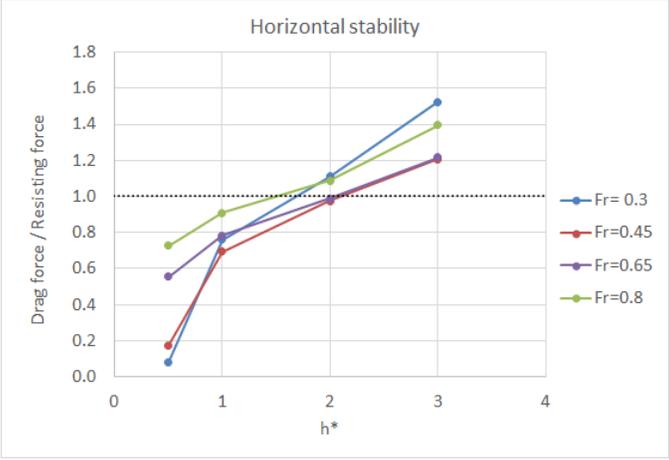
*Figure A2- 7. Horizontal stability of hollow box girder with P_r= 1.5.*
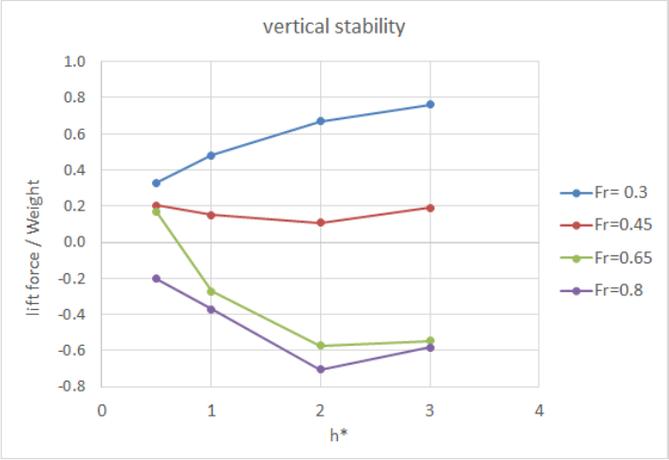
*Figure A2- 8. Vertical stability of hollow box girder with P_r= 1.5.*
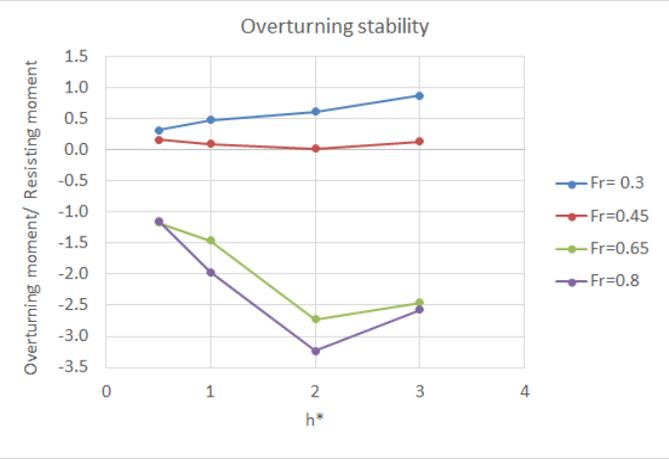
Figure A2- 9. Overturning stability of hollow box girder with P_r= 1.5.

Appendix 3

The incipient failure analysis of simple deck with wings attached to the deck (Scenario 5) for proximity ratios of 1.5, 2, 2.5, and 3 is presented in this section:
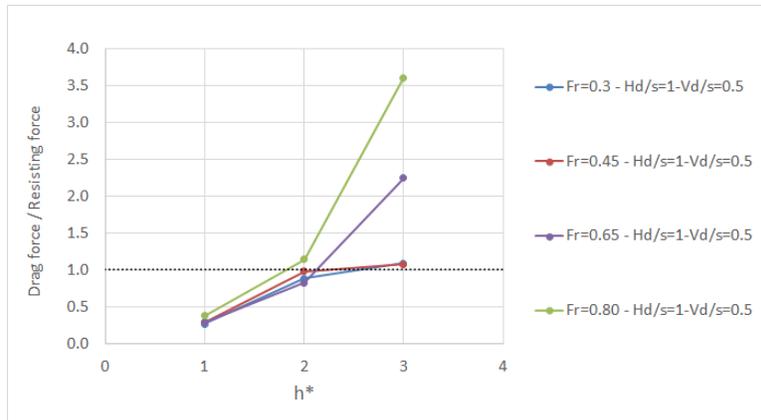

Figure A3- 1. Horizontal stability of simple deck with wings attached to the deck (Scenario 5), P_r= 1.5.
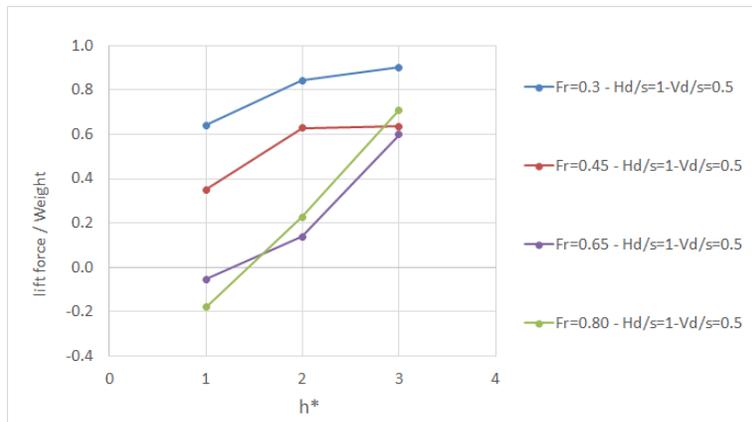

Figure A3- 2. Vertical stability of simple deck with wings attached to the deck (Scenario 5), P_r= 1.5.
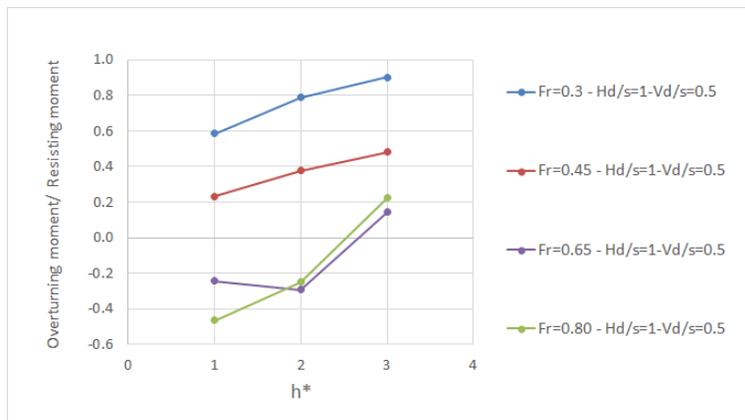
Figure A3- 3. Overturning stability of simple deck with wings attached to the deck (Scenario 5), P_r= 1.5.
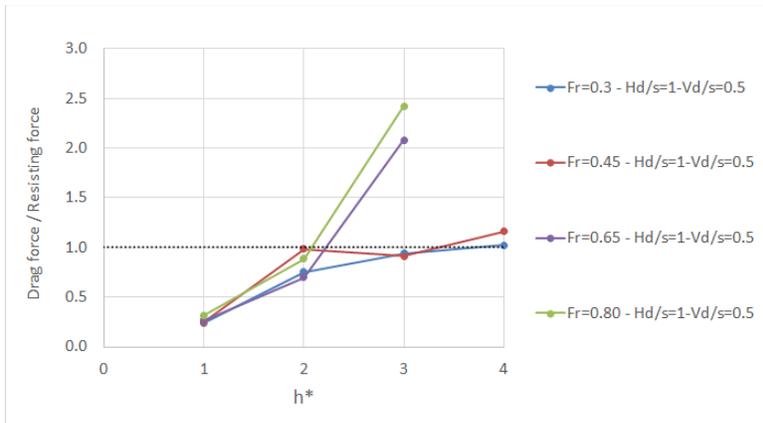
Figure A3- 4 Horizontal stability of simple deck with wings attached to the deck (Scenario 5), P_r= 2.
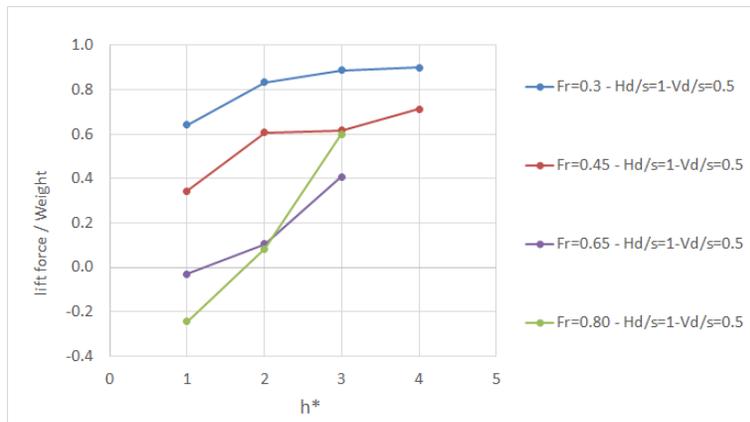
*Figure A3- 5 Vertical stability of simple deck with wings attached to the deck (Scenario 5), P_r= 2.*
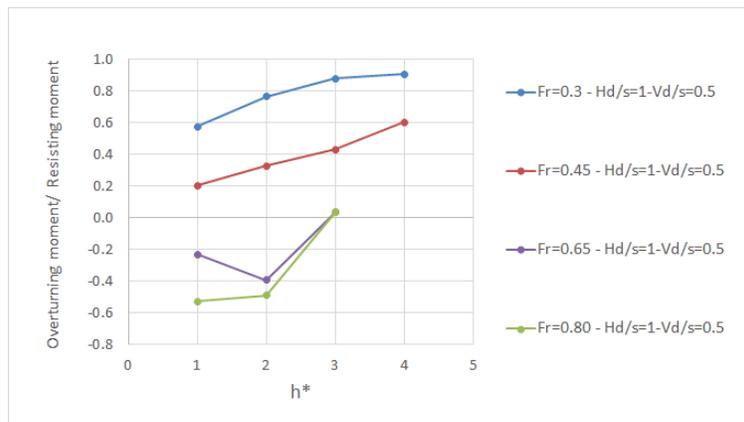
Figure A3- 6 Overturning stability of simple deck with wings attached to the deck (Scenario 5), P_r= 2.
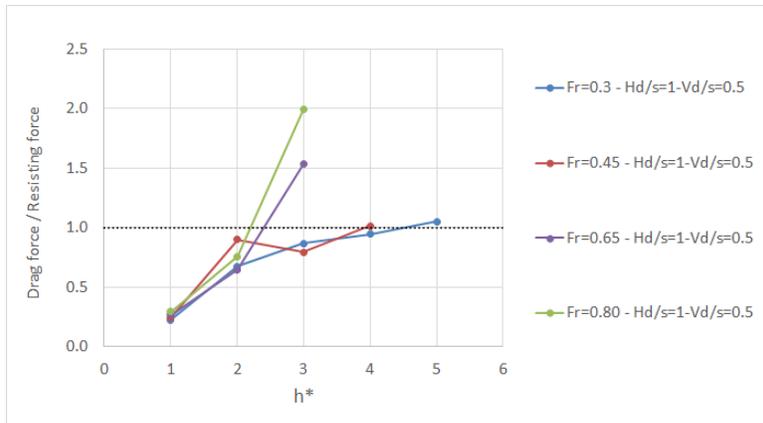
Figure A3- 7 Horizontal stability of simple deck with wings attached to the deck (Scenario 5), P_r= 2.5.
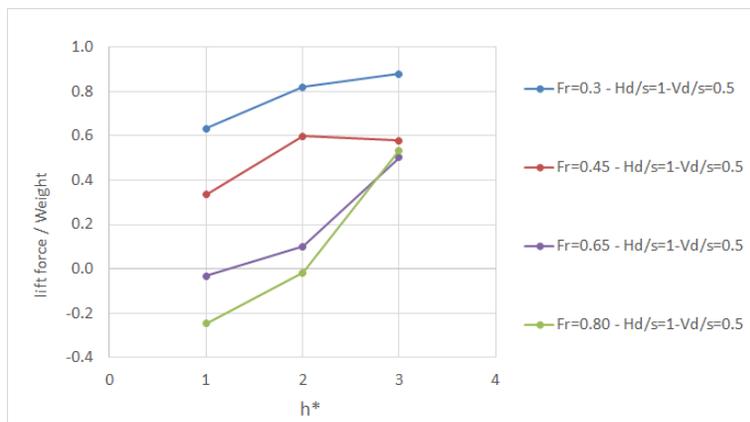

Figure A3- 8 Vertical stability of simple deck with wings attached to the deck (Scenario 5), P_r= 2.5.
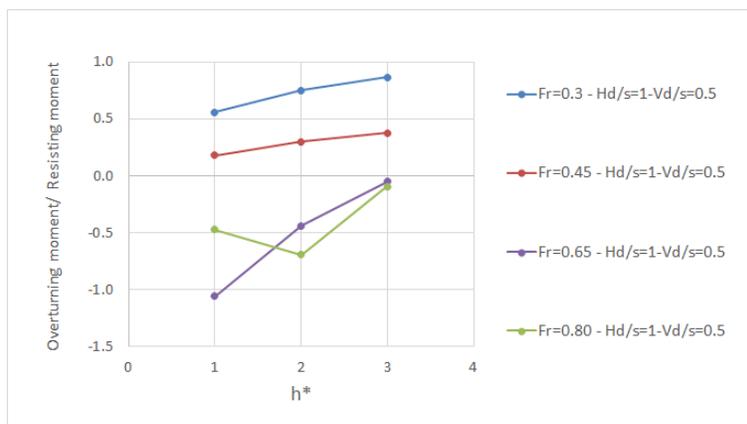
Figure A3- 9 Overturning stability of simple deck with wings attached to the deck (Scenario 5), P_r= 2.5.
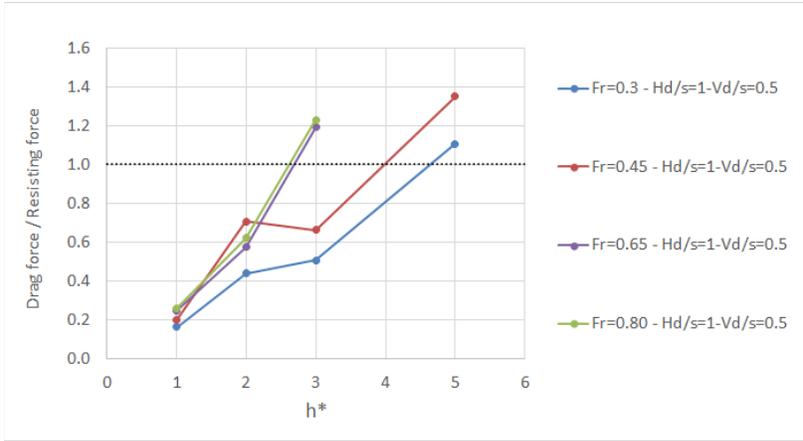
Figure A3. 10 Horizontal stability of simple deck with wings attached to the deck (Scenario 5), P_r= 3.
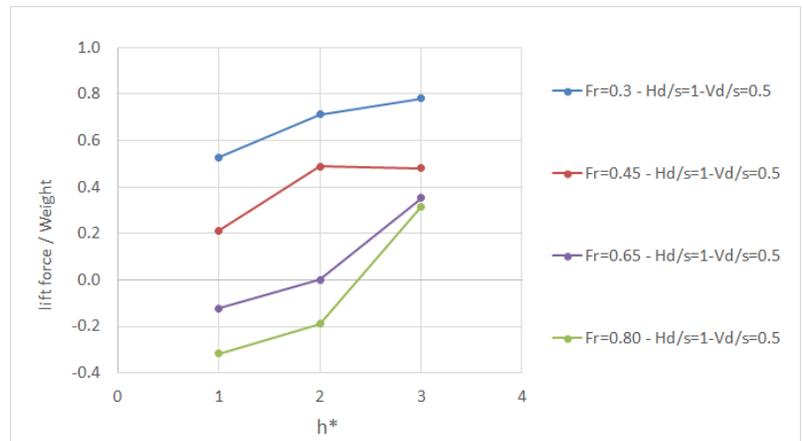
Figure A3- 11. Vertical stability of simple deck with wings attached to the deck (Scenario 5), P_r= 3.
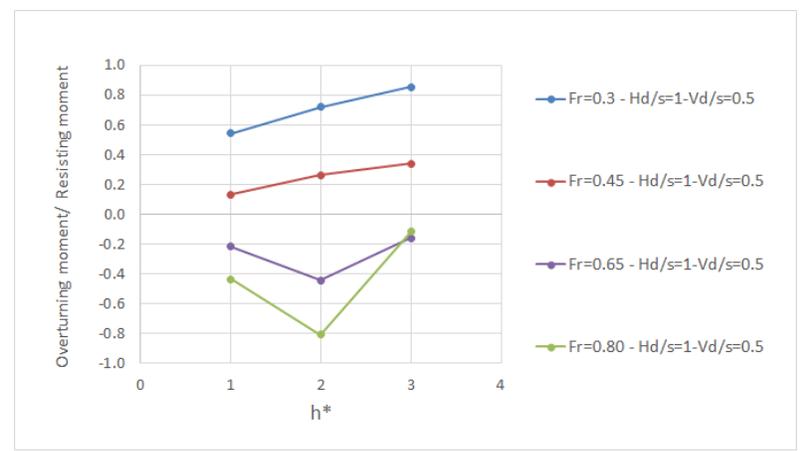

Figure A3- 12. Overturning stability of simple deck with wings attached to the deck (Scenario 5), P_r= 3.

Appendix 4

Incipient failure analysis was performed based on the unity check by considering resistance R and loads S, i.e.,

$$UC = \frac{S}{R}$$

(A-1)

Failure was defined when UC, the ratio of driving forces divided by resisting forces, becomes equal to or greater than 1. The stability ratios for horizontal, vertical, and overturning moments are defined by Equations A-1, A-2, and A-3, respectively.

$$UC_h = \frac{F_S}{F_R} = \frac{F_D}{F_{fri}} = \frac{F_D}{\mu \times (F_W - (F_L + F_B))}$$

(A-2)

$$UC_V = \frac{F_S}{F_R} = \frac{F_B + F_L}{F_W}$$

(A-3)

$$UC_M = \frac{M_S}{M_R} = \frac{-M_h}{F_W \times L_{cg}}$$

(A-4)

F_D: Drag force

F_L: Lift force

F_W: Gravitational force

F_B: Buoyancy force

M_h: Moment around the heel

L_{cg}: Horizontal distance from the centre of gravity to the lower downstream heel of the deck

μ: frictional coefficient of bearing
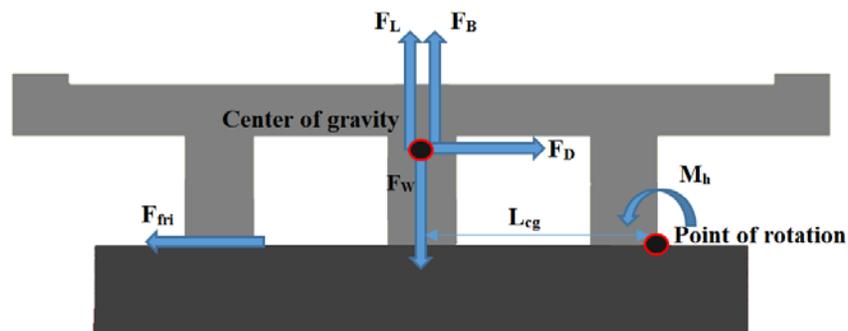
Figure A4- 1. Forces acting on the submerged deck.

References

[1] P. Junke Guo, "Computational Design Tool for Bridge Hydrodynamic Loading in Inundated Flows of Midwest Rivers," University of Nebraska-Lincoln , 2010.

[2] Madeleine M. Flint, Oliver Fringer; Sarah L. Billington, David Freyberg, and Noah S. Diffenbaugh, "Historical Analysis of Hydraulic Bridge Collapses in the Continental United States," *Journal of Infrastructure Systems,* vol. 23, no. 3, 2017.

[3] "Can you stop bridges collapsing in floods.," 23 11 2009. [Online]. Available: http://news.bbc.co.uk/2/hi/uk_news/magazine/8374616.stm. [Accessed 8 2 2018].

[4] Tze Liang Lau, Tatsuo Ohmachi, Shusaku Inoue and Panitan Lukkunaprasit., Experimental and Numerical Modeling of Tsunami Force on Bridge Decks, intech, 2011.

[5] Sibel Kara, Thorsten Stoesser, Terry W. Sturm & Saad Mulahasan, "Flow dynamics through a submerged bridge opening with overtopping," *Journal of hydraulic research,* vol. 53, no. 2, pp. 186-195, 2015.

[6] D. MAX SHEPPARD, JUSTIN MARIN, "Wave loading on bridge decks," Florida Department Of Transportation, Florida, 2009.

[7] A. J. G. a. B. E. McCallum, "Epic Flooding in Georgia, 2009," U.S. Geological Survey Fact Sheet, 2010.

[8] "Learning from Earthquakes: Bridge Performance in the Mw 9.0 Tohoku Japan, Earthquake of March 11, 2011.," EERI Special Earthquake Report.

[9] Denis Istrati, Ian G Buckle, Pedro Lomonaco, Solomon Yim, Ahmad Itani, "TSUNAMI INDUCED FORCES IN BRIDGES: LARGE-SCALE EXPERIMENTS AND THE ROLE OF AIR-ENTRAPMENT," *COASTAL ENGINEERING ,* vol. 35, 2016.

[10] M. K. a. P. M. S. PATIL, "Computational Fluid Dynamics Simulation of Open-Channel Flows Over Bridge-Decks Under Various Flooding Conditions," in *Proceedings of the 6th WSEAS International Conference on FLUID MECHANICS (FLUIDS'09)*, Athens, 2009.

[11] "Bridge Design & Assessment," David Childs B.Sc, C.Eng, MICE, [Online]. Available: http://www.bridgedesign.org.uk/parts/bearing.html. [Accessed 27 2 2018].

[12] M. A. Jempson, "FLOOD AND DEBRIS LOADS ON BRIDGES," University of Queensland, 2000.

[13] T. S. a. J. G. Kornel Kerenyi, "Hydrodynamic Forces on Inundated Bridge Decks," he Federal Highway Administration (FHWA) , 2009.

[14] T. E. /. A. C. J. /. P. A. C. Fenske, "Debris forces and impact on highway bridges," IABSE reports, 1995.

[15] M. Azadbakht, "Tsunami and hurricane wave loads on bridge superstructures," Oregon State University, 2014.

[16] K. Kawashima, H. Matsuzaki , "Damage of Road Bridges by 2011 Great East Japan (Tohoku) Earthquake," in *15 WCEE*, 2012.

[17] A. N. H. T. J. M. T. M. Jeremy D. Bricker, "Mechanisms of damage to coastal structures due to the 2011 Great East Japan Tsunami," *Handbook of Coastal Disaster Mitigation for Engineers and Planners,* pp. 403-410, 2015.

[18] M. Jeremy D. Bricker and a. A. Nakayama, "Contribution of Trapped Air, Deck Superelevation, and Nearby Structures to Bridge Deck Failure during a Tsunami," *Journal of Hydraulic Engineering,* vol. 140, no. 5, 2014.

[19] S. M. K. K. a. A. H. Hamed Salem, "Collapse analysis of Utatsu Ohashi bridge damaged by Tohoku Tsunami using Applied Element Method," *Journal of advanced concrete technology,* vol. 12, pp. 388-402, 2014.

[20] Y. K. Y. G.Shojia, "Evaluation of Tsunami Fluid Force Acting on a Bridge Deck Subjected to Breaker Bores," *Procedia Engineering,* vol. 14, pp. 1079 - 1088, 2011.

[21] K. MARUYAMA, Y. TANAKA, K. KOSA, A. HOSODA, T. ARIKAWA and N. MIZUTANI, "EVALUATION OF TSUNAMI FORCE ACTING ON BRIDGE GIRDERS," in *The Thirteenth East Asia-Pacific Conference on Structural Engineering and Construction (EASEC-13),*, Sapporo, 2013.

[22] W. Johnson, "Immense force of water ripped 2 bridges completely away; MoDOT on fast track to replace them," [Online]. Available: https://www.news-leader.com/story/news/local/missouri/2017/05/02/immense-force-water-ripped-2-bridges-completely-away-modot-fast-track-replace-them/101197394/. [Accessed 27 2 2017].

[23] A. Ozarks, "Hammonds and James Bridges after flooding in MO 2017," [Online]. Available: https://www.youtube.com/watch?v=33wdHQnHII0&t=1s. [Accessed 27 2 2018].

[24] C.-R. C. e. al., "Numerical simulation of hydrodynamic loading on submerged rectangular bridge decks," in *The Seventh International Colloquium on Bluff Body Aerodynamics and Applications (BBAA7)* , Shanghai, 2012.

[25] "Hydrodynamic Loading on River Bridges," *Journal of Hydraulic Engineering,* vol. 129, no. 11, pp. 854-861, 2003.

[26] G. E. C. I. H. D. L. R. a. S. A. Chen, " Analysis of the Interstate 10 twin bridge's collapse during Hurricane Katrina," Science and the storms, the USGS response to the hurricanes of 2005, 2005.

[27] W. H. a. H. Xiao, "Numerical Modeling of Dynamic Wave Force Acting on Escambia Bay Bridge Deck during Hurricane Ivan," *J. Waterway, Port, Coastal, Ocean Eng,* vol. 135, no. 4, pp. 164-175, 2009.

[28] Qin Chen; Lixia Wang; and Haihong Zhao, "Hydrodynamic Investigation of Coastal Bridge Collapse during Hurricane Katrina," *Journal of Hydraulic Engineering,* vol. 135, no. 3, 2009.

[29] "Australian Bridge Design Code," Standards Australia International Ltd , Sydney, 2004.

[30] W. Uijttewaal, "Turbulence in hydraulics CT5312 (Lecture Notes).," TU Delft, 2018.

[31] R. S. Raja, "Coupled fluid structure interaction analysis on a cylinder exposed to ocean wave loading," 2012.

[32] "ANSYS FLUENT 12.0 , User's Guide," 2009.

[33] T. Ducrocq, "Flow and drag force around a free surface piercing cylinder for environmental applications," *Environmental Fluid Mechanics,* vol. 17, no. 4, pp. 629-645, 2017.

[34] S. D. Mudiyanselage, "Effect of Nappe Non-aeration on Caisson Sliding Force during Tsunami Breakwater Overtopping," TU Delft, 2017.

[35] "Bridges," Spanbeton, [Online]. Available: https://www.spanbeton.nl/nl/media/kennisportaal-consolis-spanbeton/. [Accessed 4 6 2018].

[36] "Elastomeric Bearings," Cosmec Inc., [Online]. Available: http://www.cosmecinc.com/Elastomeric%20Bearings. [Accessed 4 6 2018].

[37] "Bearings," Trellebrog, [Online]. Available: http://www.trelleborg.com/en/engineered-products/products--and--solutions/bearings/?sortType=&startItem=0&numberOfItems=8&id=e80da030-1708-43ed-b182-728020be3a6a. [Accessed 4 6 2018].

[38] D. C. v. d. Veen, *Concrete Bridges - course CIE5127,* TU Delft, 2018.

[39] Saneie, M. Sheikh Kazemi, J. Azhdary Moghaddam, M., "Scale Effects on the Discharge Coefficient of Ogee Spillway with an Arc in Plan and Converging Training Walls," *Civil Engineering Infrastructures Journal,* vol. 49, no. 2, pp. 361-374, 2016.

[40] J. P. J. Warburton, "Surface tension in small hydraulic river models - The significance of the Weber number," *Journal of Hydrology,* vol. 35, no. 2, pp. 199-212, 1996.

[41] N. Isyumov, "Wind Engineering Terminology," *The University of Western Ontario,* 2015.